CONCEPTUAL THERMAL RESPONSE MODELING, TESTING, AND DESIGN OF FLEXIBLE HEATSHIELD INSULATION MATERIALS

A Dissertation
Presented to
The Academic Faculty

by

Grant Rossman

In Partial Fulfillment
of the Requirements for the Degree
Doctor of Philosophy in the
Daniel Guggenheim School of Aerospace Engineering

Georgia Institute of Technology
May 2018

CONCEPTUAL THERMAL RESPONSE MODELING, TESTING, AND DESIGN OF FLEXIBLE HEATSHIELD INSULATION MATERIALS

Approved by:

Dr. Robert D. Braun, Advisor
Committee Chair, Adjunct Professor
Daniel Guggenheim School of
Aerospace Engineering
Georgia Institute of Technology

Dr. Brian German
Associate Professor
Daniel Guggenheim School of
Aerospace Engineering
Georgia Institute of Technology

Dr. Marcus Holzinger
Assistant Professor
Daniel Guggenheim School of
Aerospace Engineering
Georgia Institute of Technology

Dr. John Dec
Program Manager
Terminal Velocity Aerospace

Dr. Mairead Stackpoole
Materials Science Branch
NASA Ames Research Center

Date Approved: December 14th, 2017

But we're not born to chase the fading light

We're not born to fall and lose the fight

Never letting go, oh no

I'm asking you to lift me, lift me higher than I've ever been

Hold your breath and say you're gonna come with me

We were born to follow

The light that never fails

- *Andra Day*

To my parents, Stanley and Diane Rossman.

To my brother, Brooks Rossman.

Thank you for giving me sunshine throughout my entire life. You are my light that never

fails. You made it possible for me to spread my message and hit my notes.

If you can fly spread feathers like a message

Sunshine, sunshine, it's fine

I feel it in my skin, warming up my mind

As long as I can hit my notes

Imma travel down that gravel road

- *Atmosphere*

ACKNOWLEDGEMENTS

    Mom and Dad, thank you for your unwavering love and support. You made all the difference in getting me here. Thanks for always having my back. I am grateful to my brother, **Brooks**, for keeping me focused through the tough times. I would also like to thank my girlfriend, **Joanna**, for supporting me through the long days and long nights completing this dissertation. You always pushed me to do my best and not worry about the rest. Thank you.

TABLE OF CONTENTS

LIST OF TABLES

LIST OF FIGURES

xiv

LIST OF SYMBOLS AND ABBREVIATIONS

Acronyms

AKK	Aluminized Kapton laminated to Kevlar
ASTM	American Society for Testing and Materials
BF20	Ceramic Outer Fabric
CCAM	Contamination and Collision Avoidance Maneuver
CFD	Computational Fluid Dynamics
CG	Center of Gravity
CHIEFS	Convective Heating Improvement for Emergency Fire Shelters
CMA	Charring Material Thermal Response and Ablation Program
COTS	Commercial-Off-The-Shelf
C1	Candidate Insulator 1
C2	Candidate Insulator 2
DAEM	Distributed Activation Energy Model
DFT	Discrete Fourier Transformation
DoE	Design of Experiments
DoF	Degrees of Freedom
DSC	Differential Scanning Calorimetry
EDL	Entry, Descent, and Landing
EFF	Exploration Feed Forward
FIAT	Fully Implicit Ablation and Thermal Response Program
FTPS	Flexible Thermal Protection System
GB	Gas Barrier
GRAM	Global Reference Atmosphere Model
HARA	High-temperature Aerothermodynamic Radiation
HEART	High-Energy Atmospheric Reentry Test

HIAD	Hypersonic Inflatable Aerodynamic Decelerator
HULA	HIAD on ULA
IHTP	Inverse Heat Transfer Problem
INS	Insulator
IRVE	Inflatable Re-Entry Vehicle Experiment
ISS	International Space Station
KFA5	Carbon Felt Insulator
LAURA	Langley Aerothermodynamic Upwind Relaxation Algorithm
LCAT	Large-Core Arc Tunnel
LEO	Low-Earth Orbit
LI900	General Purpose Aerospace Insulation Backing
LM	Levenberg-Marquardt
L1	Layer 1
L2	Layer 2
L3	Layer 3
MAS	Mission Applications Study
MES	Main Engine Start
MLI	Multi-Layer Insulation
MSL	Mars Science Laboratory
NASA	National Aeronautics and Space Administration
PICA	Phenolic Impregnated Carbon Ablator
POST2	Program to Optimize Simulated Trajectories II
P2250	Pyrogel 2250 Aerogel Felt Insulator
P3350	Pyrogel 3350 Aerogel Felt Insulator
RSME	Root Mean Square Error
RSS	Root-Sum-Square
RV	Reentry Vehicle

SiC   Silicon-Carbide Outer Fabric

SLA   Super Lightweight Ablator

SSE   Sum of Squared Errors

TC   Thermocouple

TGA   Thermogravimetric Analysis

TPRL   Thermophysical Properties Research Laboratory

TPS   Thermal Protection System

ULA   United Launch Alliance

1D   One-Dimensional

2D   Two-Dimensional

3DOF   Three Degrees of Freedom

Subscripts

i = correlation calculation input number

j = correlation calculation Monte Carlo sample number

n = correlation calculation total number of Monte Carlo samples

k   = Error-minimization iteration number

Symbols

β_D = Ballistic coefficient

A_D = Entry vehicle drag area

C_D = Drag coefficient

m_D = Entry vehicle mass

T_b = baseline TPS thickness for RSS approach

T_1 = first TPS thickness calculation for RSS approach

T_2 = second TPS thickness calculation for RSS approach

T_3 = third TPS thickness calculation for RSS approach

C_P = Specific heat

k = Thermal conductivity

ρ = Density

ρ_i = correlation coefficient

x_{ij} = correlation calculation input variable

$x_{i,avg}$ = correlation calculation mean value of input variable

y_j = correlation calculation output variable

y_{avg} = correlation calculation mean value of output variable

N = central difference calculation number of input parameters

X_{ij} = central difference calculation sensitivity coefficients

P_j = central difference calculation vector of input parameters

T_i = central difference calculation vector of prediction outputs

$\boldsymbol{\varepsilon}$ = central difference calculation scale factor perturbation fraction

$f_{k_{INS}}$ = Scale factor for insulator thermal conductivity

$f_{C_{P_{INS}}}$ = Scale factor for insulator specific heat

$f_{perm_{INS}}$ = Scale factor for insulator permeability

$f_{por_{INS}}$ = Scale factor for insulator porosity

$f_{k_{GB}}$ = Scale factor for gas barrier thermal conductivity

$f_{C_{P_{GB}}}$ = Scale factor for gas barrier specific heat

$\mathbf{P}$ = Scale factor thermal input parameter vector

$\mathbf{T}$ = Temperature profile prediction vector from COMSOL

$\mathbf{Y}$ = Thermocouple measured experimental temperature vector

$\mathbf{J}$ = Sensitivity matrix

μ   = Damping parameter

Ω   = Diagonal matrix

S = Error-minimization objective function

ε_0 = Central difference method tolerance

ε_1 = Stopping criteria 1 tolerance

ε_3 = Stopping criteria 3 tolerance

k_R = rate constant

A = arrhenius pre-exponential factor

E_a = arrhenius activation energy

R = gas constant

T = temperature

α = degree of conversion

W_0 = initial TGA sample weight

W_t = TGA sample weight at time "t"f

$\frac{d\alpha}{dt}$ = rate of conversion

$k(T)$ = rate constant at temperature "T"

$f(\alpha)$ = kinetic expression

N = number of experiments performed for each TGA method

n = reaction order for nth order kinetics

β = constant heating rate of TGA test

m = slope of Arrhenius plot

E_{it} = iterative activation energy estimate

a = table lookup value from ASTM E1641-16

b = table lookup value from ASTM E1641-16

A_{MP} = temperature half-amplitude for modulated TGA testing

$\dfrac{d\alpha_p}{dt}$ = maximum value of $\dfrac{d\alpha}{dt}$ curve at conversion $\propto$

$\dfrac{d\alpha_v}{dt}$ = minimum value of $\dfrac{d\alpha}{dt}$ curve at conversion $\propto$

L = difference between max and min $\dfrac{d\alpha}{dt}$ curve at conversion $\propto$

$\bar{x}$ = sample mean of activation energy calculations for each TGA method

x_i = sample calculation of activation energy

s^2 = sample variance of activation energy calculations for each TGA method

s = sample standard deviation of activation energy calculations for each TGA method

dT = temperature difference

Isp = spacecraft engine specific impulse

SUMMARY

Flexible Thermal Protection Systems (FTPS) have been investigated to support many applications, including thermal protection of inflatable atmospheric entry vehicles. This flexible blanket is composed of a stack of material sheets, including heat rate resistant outer fabrics, heat load resistant insulation, and an air-tight gas barrier to prevent pressure leaks. This dissertation advances the state-of-the-art of thermal modeling, material property testing, and design of FTPS.

In this investigation, a one-dimensional (1D) thermal response model is used to predict in-depth temperatures of FTPS layups during arc-jet ground testing. An extended inverse multi-parameter estimation methodology is developed to improve thermal model prediction accuracy. This method utilizes concepts from inverse heat transfer analysis, parameter estimation, and probabilistic analysis. Thermal response model input parameters are adjusted to minimize the error between temperature predictions and in-depth temperature measurements from arc-jet ground testing.

Some FTPS insulators experience decomposition under extreme heating conditions, while others do not. In this investigation, a thermogravimetric analysis (TGA) experimental campaign was designed and executed to further characterize fibrous insulators that undergo decomposition. This material testing methodology was developed to obtain the approximate distribution of activation energy. Associated activation energies were inserted into corresponding thermal response models to improve temperature prediction accuracy.

In this investigation, a simulation-based FTPS insulator design methodology is developed to obtain a final FTPS insulator configuration. This design process uses inputs such as candidate insulators, insulator material properties, and a nominal mission profile. Candidate insulators are designed efficiently using an improved thermal response model, providing FTPS insulator stackup configurations that satisfy mission requirements.

CHAPTER I

LITERATURE REVIEW AND MOTIVATION

1.1 Background of FTPS for HIAD Applications

Atmospheric entry vehicles traveling to Mars have used vehicle geometry designs derived from heritage Viking missions. Each follow-on mission has incrementally improved landing mass capability [1]. Additionally, rigid ablators like the Super Lightweight Ablator (SLA-561V) and Phenolic Impregnated Carbon Ablator (PICA) were used on every Mars mission to date. Landing additional mass beyond the MSL capability has been shown to be difficult with present technology, motivating the advancement of technologies to enable future missions. One such technology is a Hypersonic Inflatable Aerodynamic Decelerator (HIAD) [2], [3], [4], [5], [6], [7].

A HIAD is an inflatable aeroshell that reduces the entry ballistic coefficient when compared with atmospheric entry vehicles fitted with traditional rigid aeroshells. Ballistic coefficient (β_D) is a function of the vehicle mass (m_D), drag coefficient (C_D), and drag reference area (A_D) shown in Equation 1. HIADs reduce the vehicle's ballistic coefficient by substantially increasing the vehicle's drag area while adding minimal mass.

$$\beta_D = \frac{m_D}{C_D A_D} \tag{1}$$

A lower ballistic coefficient allows the vehicle to decelerate higher in the atmosphere and decreases the peak heat rate. Unlike rigid Thermal Protection Systems (TPS), HIAD TPS must remain flexible to enable inflation before entry. The HIAD must also allow for compact packaging within the confines of a launch vehicle shroud for extended periods before inflation and eventual aerothermal loading during entry. With the advancement of

fabrics, insulation, and thin-film materials, HIADs may result in a means to increase mission capabilities. Additionally, by making improvements in FTPS material characterization and thermal response modeling, designers can obtain more accurate and more reliable FTPS mass and thickness estimates for future Earth and Mars entry missions.

1.1.1 Introduction to HIAD Applications

The primary FTPS application assumed in this dissertation is the HIAD. Figure 1 shows an image of a HIAD designed for Earth entry called the Inflatable Re-Entry Vehicle Experiment (IRVE) on the left and an artist's rendition of a HIAD for Mars entry on the right.

Figure 1: IRVE [6] (Left) and HIAD for Mars Entry [2] (Right)

Additional FTPS applications include emergency fire shelters and Multi-Layer Insulation (MLI) for spacecraft. For example, the Convective Heating Improvement for Emergency Fire Shelters (CHIEFS) project is currently underway at NASA Langley Research Center to find FTPS alternatives to improve fire shelters for wildland firefighters [8].
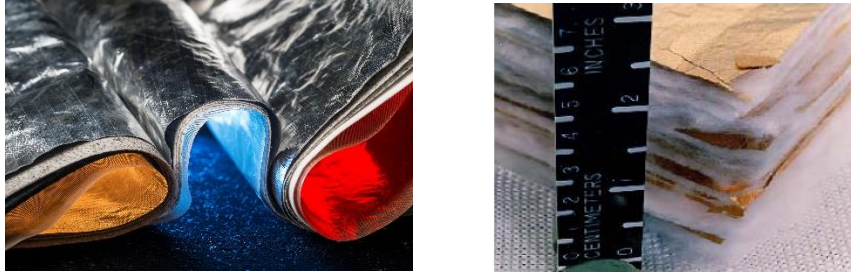
Figure 2: CHIEFS Fire Shelter FTPS [8] (Left) and MLI [9] (Right)

MLI controls spacecraft temperature in the environment of space. Daryabeigi has performed significant research advancing the state-of-the-art of thermal conductivity testing and design of MLI [9], [10], [11]. Figure 2 shows an image of CHIEFS fire shelters on the left and an image of MLI on the right.

1.1.2 Introduction to FTPS for HIAD

In this dissertation, the primary purpose of the FTPS is to protect an inflatable drag device from the harsh aerothermodynamic environment of atmospheric entry [2], [12], [13], [14], [15], [16]. FTPS consists of multiple layers, each with a unique function. The first set of layers, referred to as the outer fabric, is a porous fabric meant to protect the underlying layers from the incident heat flux. The second set of layers, referred to as the insulator, is a series of fibrous insulation layers used to protect the inflatable aeroshell from cumulative heat load with low thermal conductivity properties. The last layer, called the gas barrier, prevents hot gas flow from making contact with the aeroshell. The gas barrier lies between the FTPS and the vehicle's inflatable structure, which is the "bondline" for FTPS heatshield.
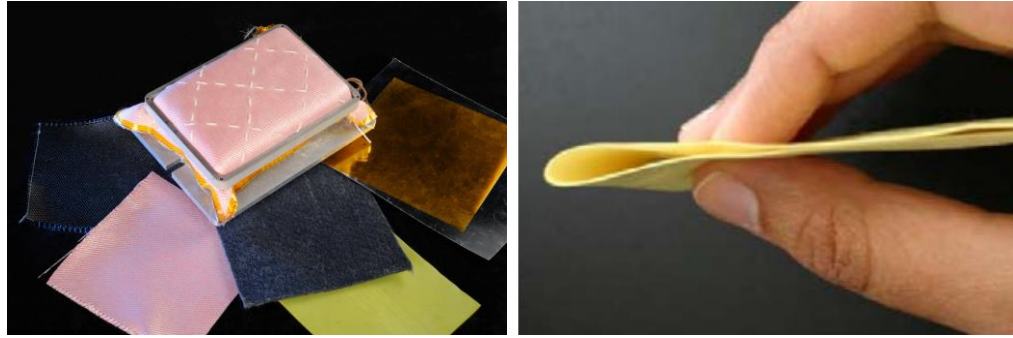
Figure 3: Sample FTPS Layups [3] (Left) and Polyimide Aerogel Insulation [3] (Right)
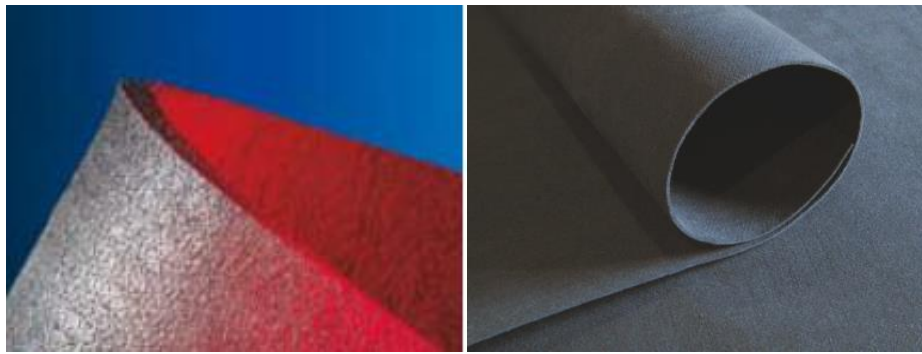
Figure 4: Sigratherm KFA5 Fibrous Insulation [17] (Left) and Aspen Aerogels Pyrogel 2250 Fibrous Insulation [18] (Right)
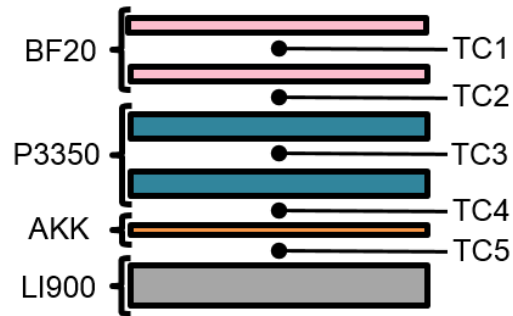
Figure 5: FTPS Layup Instrumented for Arc-Jet Testing

There are multiple material options for an FTPS configuration, including two outer fabric materials (Nextel BF-20 and Silicon Carbide), four insulator materials (KFA5, Saffil, Pyrogel 2250, Pyrogel 3350), and two gas barrier materials (Kapton and Aluminized Kapton laminated to Kevlar). Figure 3 and Figure 4 show images of example FTPS materials and insulation. The most alternatives exist for insulators because there are more

Commercial-Off-The-Shelf (COTS) options available in this domain. Figure 5 shows an example FTPS layup composed of Nextel BF-20 outer fabric, Pyrogel 3350 insulator layers, and an Aluminized Kapton laminated to Kevlar (AKK) gas barrier. Although LI-900 backing insulation is used to seal the sample in the holder, it is not considered part of the FTPS layup.

1.1.3 FTPS Challenges with Thermal Response Modeling and Design

The current FTPS design process is largely based on design intuition and selects the outer fabric based on the expected peak heat flux of a range of possible entry trajectories. Next, analysts rely on arc-jet ground test data to make screening and design decisions for the FTPS insulation layup configurations. After the final FTPS layup is selected, a Root-Sum-Square (RSS) approach is used compound sizing uncertainties together to produce a conservative heatshield thickness margin [19].

The first major set of challenges lies with the current FTPS insulator design process. Arc-jet testing is costly and time-consuming. Scarce experimental resources limit the number of runs that can be performed before selecting a final layup, forcing the analyst to make ad-hoc decisions based on an incomplete search of the insulator configuration decision space [20]. Furthermore, there are characteristics unique to FTPS that rigid-ablative design methods do not address. One such characteristic requires FTPS to be flexible. Because the primary application requires the FTPS to protect an inflatable aeroshell during entry, the FTPS itself must have the flexibility to be stowed during launch and the durability to survive rapid inflation. Another unique characteristic is its multi-layered, multi-material layup structure. As a result, urgent extensions are needed beyond traditional rigid, ablative TPS design and sizing methods. These extensions have been developed in this investigation to address the unique characteristics of FTPS and enable adequate design.

The next major set of challenges concerns thermal-material properties embedded in each FTPS thermal response model. These thermal-material properties are notoriously difficult to obtain with acceptable accuracy [21], [22]. To successfully measure material properties, one must execute rigorous experimental campaigns with specialized instruments. Limited access to material testing facilities results in an incomplete set of material properties used in thermal response models [21]. Even accurately measured thermal-material properties often neglect proper determination of associated uncertainties. In this investigation, a methodology developed to obtain experimental-based uncertainties of thermal-material properties with scarce resources, which could lead to better estimation of thermal-material property uncertainties. This effort enables probabilistic characterization of thermal-material properties, paving the way for probabilistic analysis to be performed on the each FTPS thermal response model.

Finally, current FTPS design methods do not rigorously calculate the probability of success of the final FTPS layup [19], [23]. Many uncertainties in flight-testing, ground-testing, material testing, and thermal response modeling can render the baseline thickness inadequate. Therefore, a more rigorous probabilistic approach is desired to guarantee that a chosen FTPS layup will keep the bondline under its maximum temperature constraint for a specified percentage of possible atmospheric entry trajectories.

1.2 Traditional TPS Thermal Response Modeling

Thermal response models simulate the process of heat transfer through a medium. Targeted ground-testing in flight-relevant conditions is heavily used to choose TPS material type and thickness for atmospheric entry missions. The advancement of computational capability in the previous two decades has enabled complex modeling of heat-transfer phenomena occurring within TPS exposed to flight-relevant heating. To accurately simulate a thermal event, one needs to define the physical phenomena governing

equations, thermal process boundary conditions, and the thermal-material properties of the medium [24].

1.2.1 Current State of the Art for TPS Thermal Response Modeling

Lachaud provides a comprehensive review of thermal response modeling tools used to simulate heat transfer through rigid, ablative TPS [24]. Many of today's thermal response models are based on theory from heritage codes such as the Charring Material Thermal Response and Ablation Progam (CMA) [24]. CMA was the culmination of ablation modeling efforts by leading researchers in the 1950's - 1960's and was used to calculate heatshield recession on high-velocity atmospheric vehicles [25], [26].

Initial thermal response models developed in the 1950's included basic heat transfer phenomena and thermal-material heatshield properties but did not account for mass decomposition or pyrolysis gas flow. Ablation was modeled using engineering correlations. In the early 1960's, Munson and Spindler were the first to include mass decomposition and pyrolysis gas flow in thermal response modeling using the Arrhenius relation [27]. A few additional researchers of the same era refined the treatment of organic resin decomposition. These advancements were put together to form CMA which then served as the primary thermal response model analysis tool for NASA missions for the next three decades [28].

In 1999, Milos and Chen developed the Fully Implicit Ablation and Thermal Response Program (FIAT) based on theory from CMA [29] [30]. This advancement features better convergence stability and has become the new state-of-the-art thermal response modeling tool for NASA atmospheric entry missions with rigid, ablative heatshields. Thermal response model performance is commonly validated by ground-testing of heatshield materials [29], [31], [32].

1.2.2 Traditional TPS Material Property Uncertainty Characterization

For traditional TPS thermal response models, Wright characterizes material property uncertainties into three separate categories, including stochastic variability, structural uncertainty, and parametric uncertainty [33]. By definition, stochastic variability represents all variations in the physical environment during the simulation. In the case of TPS, one example may be the variability in atmospheric density during hypersonic entry. Structural uncertainty describes how accurately the physical model represents the actual physical phenomena in reality. Two examples of structural uncertainty include using significant approximations in the physical model and generating results outside of the physical model's region of validity. Finally, parametric uncertainty describes the uncertainty of each input parameter in the physical model. Parametric uncertainty is rooted in the measurement, calculation, or estimation method used to characterize each input parameter uncertainty.

When experimental methods are not available to estimate parametric uncertainties of model input parameters, Wright provided six estimation methods from most rigorous to least [34]. These six methods include averaging the material property's mean and standard deviation from multiple sources, conducting an independent review of a property's uncertainty from single source, estimating the property's uncertainty from compiled databases, quoting the property's uncertainty from the original data source, applying the uncertainty from a similar property, and conducting an expert opinion poll. Many of the probabilistic uncertainty characterization methods specified by Wright can be applied to the FTPS thermal response modeling process to improve prediction accuracy. The following section discusses the current approach to FTPS thermal response modeling.

1.3 FTPS Thermal Response Modeling

An FTPS layup experiences many heat transfer modes under extreme heating conditions as shown in Figure 6 [21]. Convective heating, solid conduction, gas conduction, and radiative transport are all fundamental heat generation modes included in many types of thermal response models [9]. More complex phenoma unique to FTPS include mass decomposition, pyrolysis gas flow, pyrolysis gas convective heat transfer, and radiative heating to surroundings. Mass decomposition and pyrolysis gas flow are of particular interest because they can potentially lower FTPS layup bondline temperatures [2].
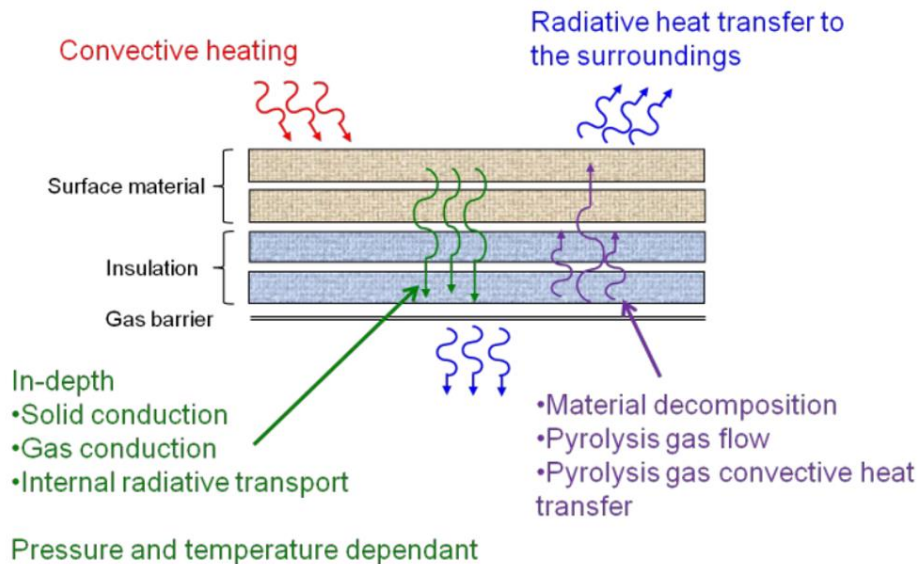
Figure 6: Modes of Heat Transfer in FTPS During Arc-Jet Testing [21]

The Boeing Large-Core Arc Tunnel (LCAT) arc-jet facility generates wind-tunnel conditions that replicate flight-relevant surface heat fluxes and flow velocities experienced by FTPS during Earth and Mars atmospheric entry missions. Each candidate FTPS layup can be instrumented with thermocouple (TC) sensors between each material layer to obtain temperature measurements as a function of time at various depths. The analyst is most concerned with measuring the FTPS layup's bondline temperature during an arc-jet

experiment because this value will prevent catastrophic failure from overheating. All arc-jet tests in this investigation apply constant heat flux profiles to FTPS layups.

1.3.1 Motivation for FTPS Thermal Response Modeling

Analysts can simulate the thermal response of FTPS only after performing a great deal of flight relevant arc-jet experiments on various layup combinations and recording temperatures between material layers. Development of an accurate thermal response model reaffirms understanding of the most significant thermal phenomena occurring within layups during extreme heating conditions. This confirmation gives analysts confidence that they can reliably predict in-depth temperatures as a function of time given flight-relevant boundary conditions such as peak heat flux and peak surface pressure.

There are no ground-based facilities that can simultaneously match all of the flight conditions in terms of heat flux, surface pressure, and enthalpy [35], [36]. However, a validated thermal model allows analysts to predict performance of candidate FTPS configurations under boundary conditions that cannot be reproduced with ground-based experimentation.

1.3.2 Material Property Testing for FTPS Thermal Response Modeling

The validity of a thermal response model is heavily driven by the accuracy of thermophysical properties used to represent heat-transfer through each material. Obtaining more precise thermal-material properties will yield better thermal response model predictions. Therefore, investment in the methods and tools used to characterize TPS thermal-material properties is a key approach to reduce uncertainties and enable thermal response model validation.

Thermal conductivity is most commonly calculated by measuring thermal diffusivity directly with the Laser Flash Method [37]. Insulation materials provide a unique challenge because they are fibrous and designed to have low thermal conductivity. One method used

by Purdue's Thermophysical Properties Research Laboratory (TPRL) to measure insulator thermal conductivity is called a Step Heat Apparatus [38]. This apparatus exposes one face of the sample to a constant heat flux and measures the resulting temperature on the sample's back side. Applying a known heat flux boundary condition over time allows the analyst to solve for bulk thermal conductivity. Daryabeigi used an alternative approach to measure thermal conductivity. As described in [39], [40], [11], [41], [9], he built a custom apparatus used to measure thermal conductivity specifically for fibrous insulation following American Society for Testing and Materials (ASTM) C201 [42].

Specific heat is traditionally measured using a Differential Scanning Calorimetry (DSC) experimental apparatus [43]. A traditional DSC encloses two small crucibles in a controlled furnace environment by surrounding samples with a selected inert gas and exposing them to a programmed temperature profile. One crucible contains sample material while the other crucible remains empty. During the experiment, one can determine the heat flow difference between the sample crucible and the empty reference crucible, which is used to calculate the sample material's specific heat.

Thermogravimetric Analysis (TGA) is used to characterize a decomposition weight-loss event as a function of temperature or time. Material samples are exposed to a controlled environmental composition, pressure, and temperature profile while measuring the sample mass loss. In order for a decomposition weight-loss event to occur, there must be a certain amount of thermal energy present before the process can begin or "activate". One fundamental quantity obtained from TGA experimentation is this required activation energy for a specific decomposition event. In this investigation, activation energy is experimentally determined with TGA to improve the FTPS thermal response model.

1.3.3 Thermogravimetric Analysis for FTPS Thermal Response Modeling

The method of TGA most generally used to characterize TPS material decomposition is the Ozawa-Flynn-Wall method, which is referred to as the Standard TGA method herein.

11

To obtain one determination of activation energy, this method requires 4 experiments each performed at a unique heating rate between 1 ˚C/min and 10 ˚C/min. After performing these four TGA tests, one can determine the sample material's activation energy by following a calculation method sanctioned by ASTM. A relatively new technique, referred to as the Modulated TGA method, allows the analyst to obtain the activation energy of a sample material after only one experiment. Modulated TGA exposes the sample to a temperature profile that oscillates about a constant heating rate between 1 ˚C/min and 2 ˚C/min. This investigation makes this comparison for FTPS insulation materials and shows the viability of using Modulated TGA to characterize the decomposition of all TPS materials with less experimental effort. In this investigation, insulator decomposition is modeled using the Arrhenius equation.

1.3.4 FTPS Insulator Decomposition Modeling

Both Standard and Modulated TGA methods assume that the Arrhenius relation is valid for the tested material sample. The Arrhenius equation, which is shown in Equation 2 [44], has been chosen to model FTPS insulator decomposition behavior in this investigation.

$$k_R = A \, e^{\left(-\frac{E_a}{RT}\right)} \tag{2}$$

The fundamental form of the Arrhenius equation defines the approximate relationship between the rate constant (k_R) and the activation energy (E_a) for a material. This expression is a function of the pre-exponential factor (A), the universal gas constant (R), and the temperature (T) of the sample material. Performing TGA results in an experimental determination of the activation energy (E_a) and the analyst can calculate a corresponding pre-exponential factor (A) if desired.

Although previous FTPS thermal response model decomposition modules assume Arrhenius behavior for insulator decomposition, limited experimental resources have caused analysts to estimate fundamental quantities in Equation 2 without formal

experimentation. One of the main goals of this investigation is to increase knowledge of thermal response model physical properties, to increase temperature prediction accuracy.

1.3.5 FTPS Material Property Uncertainty Characterization

Many input parameter uncertainties for each FTPS thermal response model rely on expert opinion due to limited experimental resources. This can present precision challenges for probabilistic heatshield sizing, which motivates the need for rigorous, targeted experimental methods to reduce as many parameter uncertainties as possible. Finding the probability density function of material properties within a thermal response model enables the use of probabilistic methods to perform uncertainty analysis, sensitivity analysis, and heatshield sizing. Better uncertainty characterization enables analysts to rigorously determine the probability of success of proposed heatshield designs, which can reduce the chance of over-margining heatshield thickness and increase mission capabilities.

1.4 Inverse Parameter Estimation for Thermal Response Modeling

Thermal response models are commonly used to solve the direct analysis problem. For the TPS community, solving the direct problem means the analyst seeks to describe the thermal response of a TPS material using known boundary conditions, known material properties, and known thermal model input parameters. The traditional TPS design process precisely measures thermal response of candidate TPS materials (through testing) without complete knowledge of boundary conditions or material properties. When the analyst has measured thermal response data and known boundary conditions, an inverse problem may be solved to obtain estimates of heatshield material properties [45].

1.4.1 Parameter Estimation for the Inverse Heat Transfer Problem

Inverse methods have been used frequently to solve problems associated with heat transfer, especially with regards to TPS [45], [46], [47], [48], [49], [50], [51], [52]. This

field of research is generally referred to as the Inverse Heat Transfer Problem (IHTP). Recent studies have used parameter estimation within the IHTP framework to reconstruct boundary conditions imposed on atmospheric entry vehicles during an atmospheric entry [53], [54], [55], [56], [57], [58]. Inverse methods provide the analytical tools needed to estimate heat transfer boundary conditions or material properties from experimental data measurements collected during a test. In this investigation, focus will be placed on estimating TPS material properties from experimental thermocouple temperature measurements.

1.4.2 Inverse Parameter Estimation Techniques for TPS Thermal Response Modeling

Recently, an inverse estimation methodology was created by Mahzari to allow for the multi-parameter estimation of TPS material properties within a thermal response model using temperature profile data obtained from ground-testing or flight-testing [56]. Mahzari's methodology consists of four consecutive steps referred to as nominal analysis, uncertainty analysis, sensitivity analysis, and inverse analysis [59]. Nominal analysis guides the analyst in preparing measured temperature data for estimation. Uncertainty analysis uses Monte Carlo techniques to identify which material property input parameters have the largest uncertainty contribution to temperature predictions. Sensitivity analysis investigates the correlation between material property input parameters to determine which parameters can be independently estimated during inverse analysis. Finally, inverse analysis estimates targeted material input parameters by minimizing a least-squares objective function difference between measured and predicted thermocouple temperatures. Mazhari applied his methodology to a FIAT thermal response model to estimate either a surface heating function or estimate material property parameters using the TC driver approach for rigid TPS applications [54].

The inverse estimation methodology created by Mahzari was a significant advancement in the state-of-the-art for characterization of thermal response models for rigid, ablating

14

TPS. However, Mahzari's methodology relied on the governing physical equations built into previously validated thermal response tools. For this reason, Mahzari was limited to applying this inverse estimation methodology to only FIAT thermal input parameters and not to parameters that governed more complex physical processes in heritage source code. Extensions beyond Mahzari's methodology are required to properly characterize and improve FTPS thermal response models.

1.5 Flexible Thermal Protection System Design and Sizing Analysis

Relative to a rigid ablator, a FTPS possesses significant physical differences – multiple materials used, multiple layers used, and decomposition that depends on the insulation material selected. Advanced design techniques for traditional TPS must be significantly altered to accommodate FTPS.

One of the major benefits of creating a validated FTPS thermal response model is using it as a design tool. This benefit has not been realized yet to improve the heatshield design and sizing process. For complete validation, it is necessary to verify that equations describing the physical processes within the model are correct and confirm that predicted behavior matches observations recorded during ground-testing. Once the analyst has completed validation, such tools may be used to predict FTPS performance for nominal atmospheric entry mission trajectories.

1.5.1 HIAD Earth Entry Nominal Mission Profile

A nominal HIAD atmospheric entry trajectory was assumed in this investigation to provide a realistic demonstration of the methodologies developed. This mission was developed as a joint effort between the HIAD team at NASA Langley Research Center and the United Launch Alliance (ULA), and as such, was named HIAD on ULA (HULA). The nominal mission aims to return the second stage of a launch vehicle to Earth from Low Earth Orbit (LEO) for re-use. Figure 7 shows a preliminary concept of operations for the

nominal mission along with a zoomed-in image of a fully-inflated HIAD separating from the second stage.
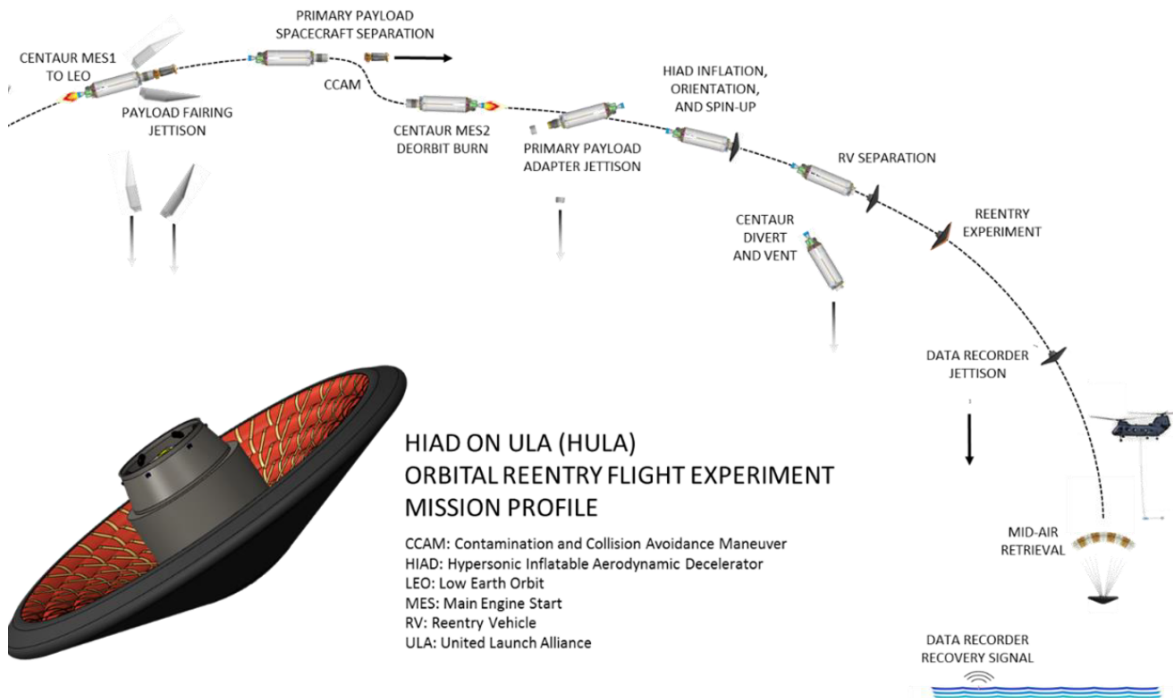
Figure 7: Nominal HIAD Second-Stage Return Mission Concept of Operations [60]

The concept of operations starts on the far left after the launch vehicle first stage falls away. A Main Engine Start (MES) thrusts the vehicle forward to allow the payload fairing to be jettisoned and the primary payload spacecraft to be exposed. Once the primary payload is injected into LEO, the vehicle performs a Contamination and Collision Avoidance Maneuver (CCAM) to ensure the vehicle does not collide with the jettisoned primary payload. Another MES, followed by HIAD inflation and vehicle spin-up, prepares the Reentry Vehicle (RV) for atmospheric reentry. The HIAD's first objective is to protect the launch vehicle second stage from peak heating. Afterwards, the HIAD separates from the second stage along a spin-stabilized ballistic trajectory to complete its second objective, which is a flight-test demonstration. Relevant flight data will be recorded on a device, jettisoned to safety, and the HIAD will be recovered.

16

This investigation uses the nominal trajectory provided to demonstrate a streamlined and efficient process that can be used to design a FTPS for atmospheric Entry, Descent, and Landing (EDL). Focus will be placed on potential HIAD atmospheric entry for Earth missions as a proof of concept, but the interested designer can apply this methodology for EDL to other atmospheric bodies. The nominal trajectory was calculated using NASA's Program to Optimize Simulated Trajectories II (POST2) while leveraging mass models, aerodynamic databases, and aeroheating tables from previous studies described in the following section.

1.5.2 Nominal HIAD Earth Entry Mission Trajectory Analysis

A recent publication, the HIAD Mission Applications Study (MAS), by Bose et al established HIAD mission reference vehicles for Earth and Mars Entry [61] . The tools developed in the MAS enabled analysts to obtain realistic aeroheating boundary conditions for a broad range of HIAD atmospheric entry missions, including the nominal mission analyzed in this dissertation [60] [62]. This dissertation will focus on the Earth entry reference vehicle displayed in Figure 8, featuring a half-cone angle of 60 degrees, a nose radius of 6.0 meters, and an approximate diameter of 5.0 meters.

Figure 8: HIAD MAS Earth Entry Reference Vehicle [61]

A parametric mass model was used to estimate total vehicle mass [63]. Aerodynamic databases were also developed in previous studies for the High-Energy Atmospheric Reentry Test (HEART) and the Inflatable Reentry Vehicle Experiment (IRVE) [2] [7]. The three main parts of the aerodynamic database include the IRVE aerodynamic database used up to Mach 3, a set of HEART continuum solutions used between Mach 3 and Mach 25, and free-molecular HEART solutions at LEO altitudes [61] [64].

The aeroheating database was developed as a part of the HIAD MAS study using cutting-edge coupling of the Langley Aerothermodynamic Upwind Relaxation Algorithm (LAURA) and the High-temperature Aerothermodynamic Radiation (HARA) code [61]. The result yields an aeroheating database that estimates combined convective and radiative heating.

The databases described for mass, aerodynamics, and aeroheating were leveraged in the POST2 code to obtain realistic heat flux profiles and surface pressure profiles for each nominal trajectory. These heat flux and pressure profiles were imported as boundary conditions for the FTPS thermal response model as a function of time to generate temperature predictions between FTPS layers for an Earth entry mission.

1.5.3 Probabilistic Sizing Methods for Traditional TPS

Rigid-ablative TPS design has a rich history with regards to atmospheric entry and has been the overwhelming heatshield configuration of choice for both manned and robotic missions [65]. Some notable rigid ablative entry missions include Apollo with the use of an Avcoat heatshield, Viking with the use of an SLA 561-V heatshield, and Mars Science Laboratory (MSL) with the use of a PICA heatshield [65], [66], [67], [68], [69]. Due to its frequency of use, rigid-ablative TPS has been the focus of TPS design methods for decades.

Traditional design methods for rigid-ablative TPS are approximate, relying on over-conservative heatshield thickness margins [70], [71], [72]. TPS material selection depends

on expected heating conditions from a worst-case entry trajectory. Peak heat flux and stagnation pressure usually drive TPS material selection while the integrated heat load drives the required TPS thickness calculation [73], [74].

Current rigid-ablative TPS design is performed using a Root Sum Square (RSS) approach. In the RSS method, a baseline TPS thickness (T_b) is obtained from the resulting thicknesses from three separate cases, each of which applies a different combination of mission relevant uncertainties. The first thickness (T_1) is calculated using only the uncertainty from trajectory dispersion. Aerothermal uncertainty combined with trajectory dispersion uncertainty is used to calculate the second thickness (T_2). Finally, a third thickness, (T_3), is calculated using the trajectory dispersion uncertainty combined with the bondline temperature uncertainty [73]. The difference in these three cases is root-sum-squared to obtain a baseline TPS thickness (T_b) as shown in Equation 3 below. Generally, the RSS approach is conservative, leading to over-margined heatshield thicknesses [73], [75].

$$T_b = T_1 + \sqrt{(T_2 - T_1)^2 + (T_3 - T_1)^2} \tag{3}$$

Probabilistic design methods for rigid-ablative TPS were first proposed by Dec and Mitcheltree in 2002 and advanced by others [75], [76], [77], [78], [79], [33]. Cozmuta and Wright have added to this probabilistic heatshield sizing methodology in an effort to reduce unnecessary margin due to large uncertainties [73]. Wright demonstrates that increased knowledge of thermal response model input uncertainties allows the analyst to reduce overly-conservative heatshield margining.
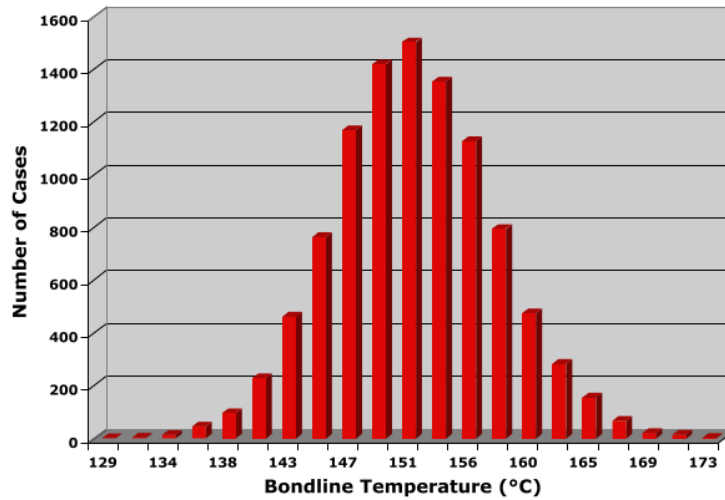
Figure 9: Wright's Bondline Temperature Distribution Obtained with Probabilistic Methods [56]

Wright and Tobin use Monte Carlo simulations to create a distribution of resulting bondline temperatures to estimate the probability of success of TPS configurations, respectively, exposed to entry-like boundary conditions. Wright's example of a bondline temperature distribution is shown in Figure 9.

1.5.4 FTPS Probabilistic Sizing Using a TRM

Probabilistic sizing methods have a rich history when designing traditional, rigid, ablating TPS systems. Unique constraints imposed by FTPS such as its multi-material design and multi-layer structure have resulted in difficulty applying probabilistic sizing methods to FTPS designs. This investigation estimated probability distributions of key thermal-material properties and adjusted top thermal response driving parameters according to an extended inverse multi-parameter estimation methodology to improve the accuracy of TRM temperature predictions.

A follow-up investigation was performed by Tobin and Dec in 2015 to size FTPS insulation using a probabilistic Monte Carlo approach [19]. This work featured more refined probability distribution estimates for key thermal-material properties and a similar

Monte Carlo analysis to determine which thermal-material properties contributed most to thermal response model prediction uncertainty. Tobin correlated an FTPS thermal response model by manually adjusting top-contributing thermal-material properties. A discrete FTPS sizing was performed by applying nominal mission trajectory dispersed heating profiles to the thermal response model as a boundary condition. Several discrete insulator thicknesses were considered for only one insulator material type. The thinnest FTPS insulation stack that did not exceed the maximum bondline temperature constraint was chosen as the final thickness.

A related study by Brune, Hosder, Edquist, and Tobin in 2016 used related probabilistic methods to characterize the HIAD heating environment upon atmospheric entry [80] [81]. Brune assumed a nominal trajectory from the Exploration Feed Forward (EFF) study [63] and performed Computational Fluid Dynamics (CFD) to obtain the transient heating environment at three points on the HIAD throughout the entire atmospheric entry trajectory. Brune assumed an FTPS layup design and performed a global nonlinear sensitivity analysis on a thermal response model considering parameters from aerodynamic heating along with FTPS thermal-material properties. After finding the top-contributing parameters, Brune created a surrogate model of the FTPS thermal response model and ran many Monte Carlo samples to obtain uncertainty bounds on the resulting bondline temperature prediction.

Note that both studies performed in 2015 and 2016 relied on manual correlation of FTPS thermal response models and did not consider using probabilistic methods to select or design the insulation materials. Tobin painstakingly correlated the FTPS thermal response model manually, selected the insulation material type a priori and focused on determining the appropriate thickness for his application. Brune selected the FTPS layup material types and thicknesses a priori, built an approximate surrogate model based on a manually correlated FTPS thermal response model, and estimated the transient bondline temperature uncertainty bounds based on his approximated model. Brune did not apply any

probabilistic methods to FTPS sizing or design. This dissertation expands on probabilistic FTPS correlation methods while developing novel FTPS insulator sizing and design methods.

1.5.5 Design Space Exploration Technique

A full-factorial design space search evaluates every possible combination of designs. Design of Experiments (DoE) are used to explore the extremes of a design space efficiently requiring far less experimental effort than a full-factorial design space. In this investigation, a specific DoE is used to enable a full exploration of FTPS insulator configuration design space under the constraint of limited experimental resources. This is because one does not have to run a full-factorial of experiments to gain understanding of how each FTPS layering combination will perform. Doing so will greatly reduce the number of FTPS thermal response models that need to be evaluated to arrive at a final FTPS insulator configuration design.

1.6 Study Overview and Contributions

Analysts designing a FTPS heatshield presently use methods developed for rigid-ablative TPS. Applying these traditional TPS design techniques to a FTPS heatshield is inadequate because these methods do not address the unique constraints of a FTPS. Heavy reliance on ground-testing for FTPS screening and design limit design space exploration for final FTPS layup configuration. The methodologies presented in this dissertation aim to address the unique challenges of FTPS design by extending traditional TPS techniques in the areas of thermal modeling, thermal-material property testing, and FTPS screening and design.

In this investigation, an existing inverse estimation methodology has been extended to a thermal response model to help improve temperature profile predictions. Next, material property testing is performed for decomposing insulators to obtain the associated activation

energies. A method is developed to obtain the probability distributions for these activation energies. Finally, a new insulator design methodology, tailored specifically to a nominal FTPS mission, is proposed to efficiently obtain a final insulator design configuration. These advancements in the state-of-the-art of FTPS analysis and design are represented in the following three contributions of this dissertation.

(1) Development of an Extended Inverse Parameter Estimation Methodology for Verification of a Modern Finite Element Solver's In-Depth FTPS Insulator Temperature Profile Predictions

This body of work extends an existing inverse estimation methodology to verify and minimize error in a physics-based thermal model developed within the COMSOL finite-element framework. Previous development of an inverse estimation methodology for rigid TPS parameter estimation used a validated NASA thermal modeling tool, which is not generally applicable during development of novel TPS materials. This work extends this existing inverse estimation methodology. For the first time, the physical underpinnings of FTPS insulator decomposition are modeled probabilistically by treating insulator activation energy, from the Arrhenius relation, as a thermal parameter with an associated probability distribution. Gradient-based algorithms are used with inverse parameter estimation to match thermal response model temperature predictions to arc-jet thermocouple temperature measurements. The extended inverse parameter estimation methodology proposed in this work uses a Monte Carlo technique to investigate the sensitivity of thermal-material properties within their estimated uncertainty bounds. These extensions will be used to improve FTPS thermal response model temperature predictions.

(2) Characterization of FTPS Insulator Mass Decomposition by Finding Activation Energy Using Thermogravimetric Analysis (TGA)

The Arrhenius relation is commonly used in TPS thermal response modeling to simulate mass decomposition processes when a material is exposed to extreme heating. Limited Standard TGA tests are usually performed at a few different heating rates to roughly

23

estimate the activation energy, which is then fed into a thermal response tool. For the first time, a Modulated TGA test method will be used to obtain the activation energy of an FTPS material. Results from the Standard and Modulated TGA experimental methods will be compared for the same FTPS insulation materials, and conclusions will be drawn about the benefits of using Modulated TGA testing for future FTPS missions. A methodology is presented to perform detailed characterization of FTPS insulator decomposition through use of TGA experimental data. A rigorous TGA test campaign is proposed to obtain the activation energies and associated probability distribution for two FTPS insulators. Not only does this lend more confidence to simulating the decomposition process, it allows the analyst to examine how much the variation in the activation energy effects the thermal response model temperature predictions.

(3) Development of a Design Methodology for FTPS Insulator Configuration Analysis

A novel design process has been proposed in an effort to arrive at a final FTPS insulator design configuration efficiently. In traditional TPS design, an exhaustive ground-test series is performed to simultaneously screen out and design heatshield materials. Such an approach uses a great deal of resources. The new methodology, proposed herein, combines thermal response modeling and concepts from simulation-based design with a few crucial ground-tests to design an FTPS insulation stack tailored for an expected nominal mission heating profile. FTPS thermal response models are validated by arc-jet measured thermocouple data using the extended inverse estimation methodology also proposed in this work. The design process performs a Monte Carlo analysis on thermal response models, representing candidate insulators, to eliminate designs with the lowest probability of success for the proposed mission. Further, a Design of Experiments (DOE) technique is applied to thermal response model containing layers from multiple attractive insulators to find FTPS insulation stackup alternatives that meet nominal mission requirements. The proposed design process can be readily extended beyond the application of an FTPS heatshield. Applications ranging from emergency fire shelters to spacecraft insulation can

make use of this simulation-based insulator design methodology to efficiently explore an insulator stack configuration design space.

1.7 Dissertation Outline

Chapter 2 will use concepts from probabilistic uncertainty analysis to characterize the contribution of thermal-material properties to thermal response model temperature prediction. Methods from inverse parameter estimation are extended to estimate key thermal parameters that result in more accurate temperature profile predictions. This iterative process will be used to help verify and minimize error between temperature predictions and measurements for FTPS thermal response models.

Chapter 3 presents a rigorous TGA experimental campaign to obtain the activation energy for two types of decomposing FTPS fibrous insulation. This improved decomposition module results from use of a new material testing methodology, developed to obtain a statistically significant sample set of TGA runs. As a final result, this contribution will calculate the activation energy of fibrous insulators and provide its uncertainty using statistical methods.

Chapter 4 presents a novel, simulation-based FTPS design methodology to efficiently reach a final FTPS insulator configuration. The complete design process uses inputs such as two candidate insulators, insulator thermal-material properties, and a nominal mission profile to screen insulators and explore the design space of a dual-insulator stackup to find best-performing insulator combinations.

Chapter 5 summarizes the dissertation and outlines suggested future work in this domain.

CHAPTER II

EXTENDED INVERSE MULTI-PARAMETER ESTIMATION METHODOLOGY

2.1 Introduction

In this chapter, an extended inverse multi-parameter estimation methodology is developed to adjust response-driving FTPS thermal-material properties within their uncertainty ranges, thereby improving thermal response model prediction accuracy. In 2013, Mahzari was the first to develop an inverse multi-parameter estimation methodology to improve thermal response modeling prediction accuracy for rigid, ablating, single-material TPS [56]. While this method remains the current state-of-the-art for rigid-ablative TPS inverse multi-parameter estimation, it is inadequate for improving FTPS thermal response models. Because FTPS is composed of multiple materials and its thermal response model has not been previously validated, Mahzari's baseline methodology cannot to be used for the FTPS application without modification. These improvements are addressed in this work as extensions to Mahzari's methodology, providing additional capability to analyze a multi-material FTPS thermal response model and assisting in the validation effort of a thermal response model that is currently under development.

2.1.1 Overview of Flexible Thermal Protection System Thermal Response Modeling

A ground-based arc-jet experiment must be developed and performed accurately on potential FTPS layups. Thermocouples must be properly placed between FTPS layers to accurately measure in-depth temperatures used as experimental boundary conditions for the thermal response model. Next, physical phenomena must be analytically described in

the thermal response model to represent the most significant thermophysical behaviors driving temperature response. A few examples of significant heat transfer behavior include conduction, convection, radiation, advection, and insulator decomposition.

Thermal-material properties must be experimentally determined and input into the thermal response model. It is notoriously difficult to accurately measure thermal-material properties for the temperature range experienced during FTPS ground-testing. Experimental measurement procedures used to measure thermal conductivity, specific heat, and activation energy usually have upper temperature limits lower than maximum measured arc-jet temperatures. Some extrapolation of thermal-material property measurements is necessary to obtain thermal response model predictions for higher temperature ranges, which serves as a source for error. As a result, some thermal-material properties need to be estimated using a multi-parameter estimation methodology to improve accuracy of thermal response model temperature predictions.

2.1.2 Multi-Parameter Estimation Methodology Extensions Developed for FTPS

When designing a FTPS heatshield and attempting to build its associated thermal response model with relatively uncharacterized candidate insulation materials, the analyst does not have the luxury of using previously validated thermal modeling tools. A physics-based thermal response model was previously built in COMSOL to simulate the thermal response of FTPS during arc jet testing [21]. This model was utilized in the present investigation.

Some candidate FTPS insulators experience mass decomposition during arc-jet testing, while others do not. The higher-fidelity thermal models used in this dissertation simulate mass decomposition for multiple FTPS insulators. In this work, Mahzari's inverse estimation methodology is extended and generalized in the following ways to accommodate the unique constraints of FTPS and its associated non-heritage thermal response model.

27

1. The mass decomposition process is included within the thermal response model by treating activation energy as an input parameter in the inverse estimation methodology.

2. Understanding the activation energy's probability distribution and associated uncertainty allows greater flexibility to analyze thermal response models. Activation energy is determined experimentally to obtain its probability distribution. Additional detail is provided in Chapter 3 on the TGA experimental procedure and probabilistic analysis.

3. Thermal input parameters from multiple materials are considered simultaneously in the inverse estimation methodology. Unlike the homogenous TPS that Mahzari considered, a FTPS layup contains at least 3 different types of materials. The methodology is extended to accommodate these different types of materials.

4. The analysis time-domain within the thermal model is segmented to focus the inverse estimation methodology only on the period of heat exposure. This provides the analyst with the ability to only apply analysis methods to a segment of interest.

5. Multiple in-depth temperature predictions from the thermal response model are improved simultaneously in the proposed extended inverse multi-parameter estimation methodology.

These extensions provide the analyst with tools to accommodate the unique characteristics of FTPS. The following section describes each step of the extended inverse multi-parameter estimation methodology.

2.2 Extended Multi-Parameter Estimation Framework for FTPS

At its most basic level, an FTPS thermal response model can be categorized under the general heat transfer problem concept. In traditional heat transfer problems, *Direct* analysis predicts temperatures at depth assuming perfect knowledge of boundary conditions and thermophysical properties. Conversely, *Inverse* analysis estimates either thermal-material properties or boundary conditions assuming temperature data at depth is known [45].

Experiments designed to test a TPS normally expose a heatshield sample to atmospheric entry-like conditions while measuring in-depth temperatures as a function of time. Boundary conditions can be estimated by analysts with defined accuracy according to the experimental setup. In this work, the Inverse Heat Transfer Problem (IHTP) is solved with focus placed on the in-depth material response problem. As a result, thermophysical properties are estimated assuming in-depth temperature measurements and boundary conditions are known.

The inverse estimation methodology created by Mahzari was a significant advancement in the state-of-the-art for characterization of thermal response models for rigid, ablating TPS. However, Mahzari's methodology relied on the governing physical equations built into previously validated thermal response tools. For this reason, Mahzari was limited to applying his inverse estimation methodology to only FIAT thermal input parameters and not to parameters that governed more complex physical processes buried in heritage source code. Extensions beyond Mahzari's methodology are required to properly characterize FTPS thermal response.
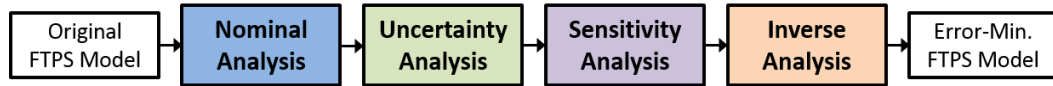
Figure 10: Extended Inverse Multi-Parameter Estimation Flowchart

The extended inverse multi-parameter estimation methodology presented in this work consists of nominal, uncertainty, sensitivity, and inverse analyses. Figure 10 shows the sequence of analysis flow applied to each FTPS thermal response model to obtain error-minimized temperature predictions. In this investigation, arc-jet experimental temperature measurements from the thermocouple between the outer fabric and insulation stack are applied to each thermal response model as a boundary condition, referred to as the Thermocouple (TC) Driver approach. In the following sections, each step of the extended inverse multi-parameter estimation methodology will be discussed.

29

2.2.1 Nominal Analysis

The main purpose of nominal analysis is to evaluate the quality of experimental temperature data and bound the problem for further analysis. When applying this methodology to thermal response models of heatshield materials, the experimental temperature data is recorded during heatshield sample exposure arc-jet heated flow. Additionally, bounding the problem refers to selecting the appropriate time-segment of data to analyze. For example, one might select specific time-domains to avoid a region of poor-quality data or one may want to focus on a time segment between key experimental events.

Ultimately, this presented methodology will select thermal-material property scale factors for inverse analysis. By evaluating the quality of experimental temperature measurements and selecting a specific time-domain of interest, nominal analysis sets up the problem for success. Overall, the test cases used to demonstrate the methodology in this dissertation have very good experimental temperature data quality and focus on the time-domain between model injection and model extraction from the arc-jet test.

2.2.2 Uncertainty Analysis

The purpose of uncertainty analysis is to determine which thermal-material property scale factors contribute most to thermal response model temperature prediction uncertainty. To do this, the uncertainty analysis presented in this dissertation uses a Monte Carlo simulation to compute a time-dependent linear regression shown in Equation 4.

$$\rho_i = \frac{\sum_{j=1}^{n}(x_{ij}-x_{i,avg})(y_j-y_{avg})}{\sqrt{\sum_{j=1}^{n}(x_{ij}-x_{i,avg})^2 \sum_{j=1}^{n}(y_j-y_{avg})^2}} \tag{4}$$

This expression includes input number (i), Monte Carlo sample number (j), total number of Monte Carlo samples (n), correlation coefficient (ρ_i), input variable (x_{ij}), mean

value of the input variable ($x_{i,avg}$), output variable (y_j), and mean value of the output variable (y_{avg}). Here, the square of the correlation coefficient is equivalent to the individual contribution of each input variable to the uncertainty of each output variable.

In this dissertation, thermal-material scale factors are assumed to be normally distributed with a mean value of 1 and a standard deviation estimated by FTPS experts. For Test Case 1 and Test Case 2, two-thousand Monte Carlo simulations are performed by randomly selecting sets of scale factor input values according to their specified distributions. Two-thousand resulting temperature profiles are then generated for each thermocouple of interest. Equation 4 is used to calculate each scale factor's contribution to temperature prediction uncertainty and determine which thermal-material property scale factors have the largest contributions to temperature prediction uncertainty.

2.2.3 Sensitivity Analysis

Sensitivity analysis serves as an additional filter to identify which of the key thermal-material property scale factors (identified via uncertainty analysis) will produce desirable convergence behavior in inverse analysis. If two parameters are linearly-dependent, or strongly correlated, they will have similar or opposing effects on the temperature predictions of the thermal response model. Due to this dependency, inverse analysis cannot distinguish the individual effects of each correlated, linearly-dependent parameter during the error-minimization process, leading to challenges with solution uniqueness. In this dissertation, sensitivity analyses were performed for thermocouples of interest within each FTPS layup to identify the correlation between scale factors, as shown by Equation 5.

$$X_{ij} \cong \frac{\partial T_i}{\partial P_j} = \frac{T_i(P_1,P_2,...,P_j+\varepsilon P_j,...,P_N) - T_i(P_1,P_2,...,P_j-\varepsilon P_j,...,P_N)}{2\varepsilon_0 P_j} \qquad (5)$$

This expression includes the number of input parameters (N), central difference sensitivity coefficients (X_{ij}), vector of input parameters (P_j), vector of temperature

31

prediction outputs (T_i), and scale factor perturbation fraction (ε). Understanding relative scale factor correlations provides valuable information about which thermophysical parameters can be estimated simultaneously to obtain a unique solution. By calculating the partial derivatives of temperature outputs with respect to scaling parameter inputs (perturbing each scale factor approximately $\varepsilon = \pm 1\%$ off nominal), one can obtain relative correlations between parameters. After determining relative correlations between scale factors, the analyst can select a smaller set of scale factors that show the least amount of linear-dependency to use for inverse analysis.

2.2.4 Inverse Analysis

The Levenberg-Marquardt (LM) method is used in this investigation to perform the inverse analysis portion of the extended inverse multi-parameter estimation methodology. It uses scaled thermal input parameters in a transient iterative process to solve a least squares minimization between arc-jet temperature measurements and thermal response model predictions [45]. The LM technique behaves like a steepest descent algorithm near the starting point, and as the solution approaches a minimum, it exhibits similar behavior to Gauss' method [45], [82], [83]. The following discussion highlights the algorithm calculation steps.

The design variables used in error-minimization are not the thermal parameters themselves. Rather, they are corresponding multiplicative scale factors (in Equation 6) for thermal parameters at time step (k) of the Insulator (INS) thermal conductivity ($f_{k_{INS}}$), INS specific heat ($f_{C_{p_{INS}}}$), INS permeability ($f_{perm_{INS}}$), INS porosity ($f_{por_{INS}}$), Gas Barrier (GB) thermal conductivity ($f_{k_{GB}}$), and GB specific heat ($f_{C_{p_{GB}}}$).

$$P^k = \left[\, f_{k_{INS}} \, , f_{C_{p_{INS}}} \, , f_{perm_{INS}} \, , f_{por_{INS}}, f_{k_{GB}}, f_{C_{p_{GB}}} \right] \tag{6}$$

Step 1: Solve the direct heating problem with P^k to obtain $T(P^k)$ (temperatures).

Step 2: Compute the objective function $S(P^k)$ shown in Equation 7 and Equation 8.

$$S(P^k) = [Y - T(P^k)]^T[Y - T(P^k)] \tag{7}$$

$$S(P^k) = \sum_{i=1}^{I}(Y_i - T_i(P^k))^2 \tag{8}$$

Step 3: Compute the sensitivity matrix J^k shown in Equation 9 and central difference approximations shown in Equation 10. Using an initial scale factor vector, P^k, the LM method uses a sensitivity matrix J^k to determine the proper ΔP^k to apply at each iteration (k) in order to approach the minimized scale factor combination, P^{k+1}.

$$J(P) = \left[\frac{\partial T^T(P)}{\partial P}\right]^T = \begin{bmatrix} \frac{\partial T_1}{\partial P_1} & \frac{\partial T_1}{\partial P_2} & \frac{\partial T_1}{\partial P_3} & \cdots & \frac{\partial T_1}{\partial P_N} \\ \frac{\partial T_2}{\partial P_I} & \frac{\partial T_2}{\partial P_2} & \frac{\partial T_2}{\partial P_3} & \cdots & \frac{\partial T_2}{\partial P_N} \\ \vdots & \vdots & \vdots & & \vdots \\ \frac{\partial T_I}{\partial P_I} & \frac{\partial T_I}{\partial P_2} & \frac{\partial T_I}{\partial P_3} & \cdots & \frac{\partial T_I}{\partial P_N} \end{bmatrix} \tag{9}$$

$$J_{ij} \cong \frac{\partial T_i}{\partial P_j} = \frac{T_i(P_1,P_2,\dots,P_j+\varepsilon P_j,\dots,P_N)-T_i(P_1,P_2,\dots,P_j-\varepsilon P_j,\dots,P_N)}{2\varepsilon_0 P_j} \tag{10}$$

Step 4: Solve Equation 11, Equation 12, and Equation 13 to find ΔP^k.

$$\Omega^k = \text{diag}\left[(J^k)^T J^k\right] \tag{11}$$

$$\left[(J^k)^T J^k + \mu^k \Omega^k\right]\Delta P^k = (J^k)^T\left[Y - T(P^k)\right] \tag{12}$$

$$\Delta P^k = \left[(J^k)^T J^k + \mu^k \Omega^k\right]^{-1}(J^k)^T\left[Y - T(P^k)\right] \tag{13}$$

Step 5: Compute the new estimate P^{k+1} using Equation 14.

$$P^{k+1} = P^k + \Delta P^k \tag{14}$$

Step 6: Solve the direct problem with the new estimate of parameters P^{k+1} to obtain the predicted temperatures $T(P^{k+1})$. Compute the new objective function $S(P^{k+1})$.

Step 7: If $S(P^{k+1}) \geq S(P^k)$, replace μ^k by $10\mu^k$ and return to step 4.

Step 8: If $S(P^{k+1}) < S(P^k)$, accept the new estimate P^{k+1} and replace μ^k by $0.1\mu^k$.

Step 9: If the stopping criterion shown in Equation 15 and Equation 16 are satisfied, stop the iterative procedure. Otherwise replace k by $k+1$ and return to step 3.

$$|S(P^{k+1}) - S(P^k)| < \varepsilon_1 \tag{15}$$

$$\left\|P^{k+1} - P^k\right\| < \varepsilon_3 \tag{16}$$

The first set of analyses uses heat flux as a boundary condition, while the second set of analyses enforces a TC driver approach by using temperature measurements between the last layer of outer fabric and the first layer of insulation.

2.2.5 TC Driver Approach

In order to remove model error associated with arc-jet flow conditions on the surface of each FTPS sample, a boundary condition was enforced in FTPS thermal response modeling. Because this investigation focuses on improving thermal response predictions within the FTPS insulation region, the boundary condition thermocouple location was selected to be at TC2, which is between the last layer of outer fabric and the first layer of insulation. Arc-jet temperature measurements are enforced at TC2 on each thermal response model to generate deeper TC temperature predictions. Applying this type of boundary condition is referred to as the TC Driver approach. A flowchart of this process applied to FTPS thermal response models in this study is depicted in Figure 11.
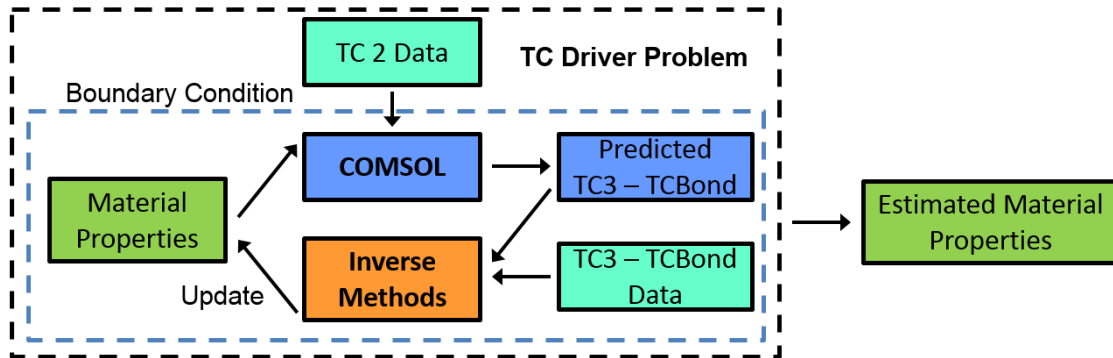
Figure 11: TC Driver Approach Flowchart

Using the TC Driver approach within the extended inverse multi-parameter estimation methodology is an iterative approach. An arc-jet measured temperature profile at the TC2 location is first applied to the thermal response model. Next, a set of nominal predictions are produced by the thermal response model between TC3 and the bondline thermocouple location (TCBond). These temperature predictions are then compared with arc-jet temperature measurements at the same locations. This process is repeated in an iterative fashion until the inverse analysis stopping criteria are met. The final result is an estimated set of thermal-material properties.

Three test cases will be used to demonstrate the effectiveness of this methodology. Each test case will contain multiple layers of a single insulation type. One thermal response model was created for each FTPS insulation type.

2.3 Introduction to Extended Multi-Parameter Estimation Framework Test Cases for FTPS with Arc-Jet Data

Arc-jet testing was conducted on FTPS material layups to characterize thermal-material performance. Thermocouples were placed between each FTPS layer during testing to obtain temperature vs. time profile measurements at various depths (TC1, TC2, TC3, TC4, or TC5). FTPS thermal response models were used to generate corresponding temperature predictions at thermocouple depths. The goal of the modeling effort is to produce thermocouple predictions within an acceptable closeness to thermocouple measurements. The thermal model initially solves the direct heat transfer problem by accepting an arc-jet measured thermocouple temperature profile as the driving boundary condition on the top surface of each FTPS layup and solving for temperature predictions at the appropriate depths. Discrepancies produced by the model itself and by uncertain knowledge of the boundary condition are expected to cause initial predictions to deviate from measurements. Parameter estimation is commonly used to reduce prediction errors by accurately

estimating thermophysical parameters within the model, hence the development of the extended inverse multi-parameter estimation methodology presented herin.

2.3.1 Arc-Jet Experiment Description

The Boeing LCAT facility makes uses of a Huels arc-heater to raise the temperature of supersonic flow through the pressurized test cabin. An external photograph of the test cabin is provided in Figure 12. Flow coming out of the exit nozzle shown in Figure 13 impinges on the FTPS sample held by the proper shear or stagnation test fixtures. For shear tests, a custom-developed wedge model was loaded with the FTPS sample and adjusted to the correct angle to achieve the target shear force, surface pressure, and heat. The shear test fixture used for Run 2259 is a semi-elliptic exit nozzle to properly displace the flow over the sample. The water-cooled, copper model holder used to perform stagnation testing on Run 2627 and Run 2822 is shown in Figure 13 [36].
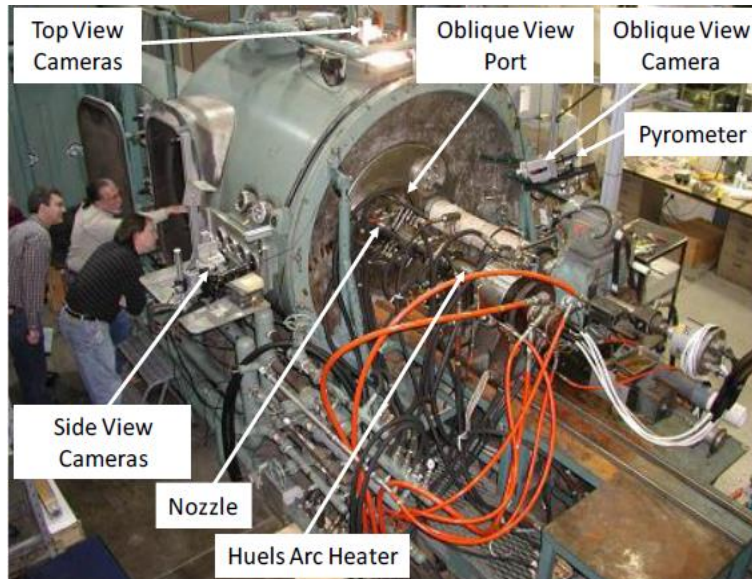
Figure 12: Boeing LCAT Arc-Jet Facility [36]
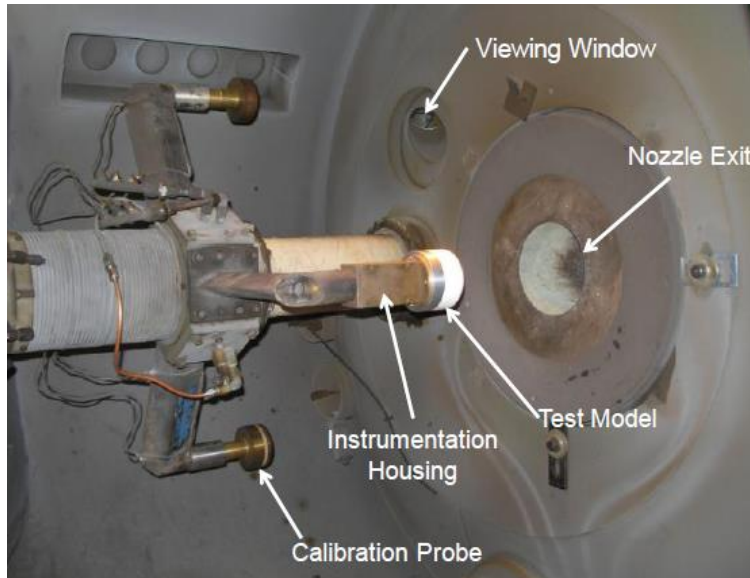
Figure 13: FTPS Stagnation Test Sting Arm [36]

Table 1 below shows the Boeing LCAT testing conditions for Layup 0's Run 2259 (shear test), Layup 1's Run 2627 (stagnation test), and Layup 2's Run 2822 (stagnation test). It is important to note that there were a small number of arc-jet data points to choose from for these specific layups.

Table 1: Boeing LCAT Testing Conditions for Test Case 0, Test Case 1, and Test Case 2 [36]

LCAT Run Number/Type	Layup Configuration	Probe Heat Flux (W/cm^2)	Surface Pressure (kPa)
2259 (Shear)	Layup 0	26.7	8.01
2627 (Stag.)	Layup 1	51.4	3.94
2822 (Stag.)	Layup 2	76.8	4.08

Thermocouples placed between FTPS layers at various depths measure temperature vs. time during experimental testing. These thermocouples have a measurement uncertainty specified by the manufacturer, Omega Engineering. Type K thermocouples are used for low-range temperature measurements with an uncertainty of approximately 0.75% of the maximum measured temperature at that location. For higher temperature ranges, Type R thermocouples are used with a defined measurement uncertainty of approximately 0.25%

37

of the maximum measured temperature at that location. The following test cases will focus on improving thermal response model temperature predictions for thermocouples in the insulation region. Thermocouples improved with the extended inverse multi-parameter estimation methodology will show calculated measurement uncertainty error bars, calculated with Omega's specifications, overlaid on its corresponding arc-jet experimental temperature measurement.

2.3.2 FTPS Material Description

In general, FTPS consists of multiple layers, each with a unique function. The first set of layers, referred to as the outer fabric, is a porous fabric meant to protect the underlying layers from the incident heat flux. The second set of layers, referred to as the insulator, is a porous insulation sheet that further prevents through-thickness heat conduction, keeping the interface to the inflatable structure. The last layer, referred to as the gas barrier, is a laminated sheet that prevents flow from traveling through the entire layup. The gas barrier also behaves as the interface between the FTPS and the vehicle's inflatable structure. The top surface of the gas barrier, or the bottom surface of the last layer of insulation, is equivalent to the "bondline" for an ablative heat shield system. This reference will hold true throughout the analyses in this chapter.
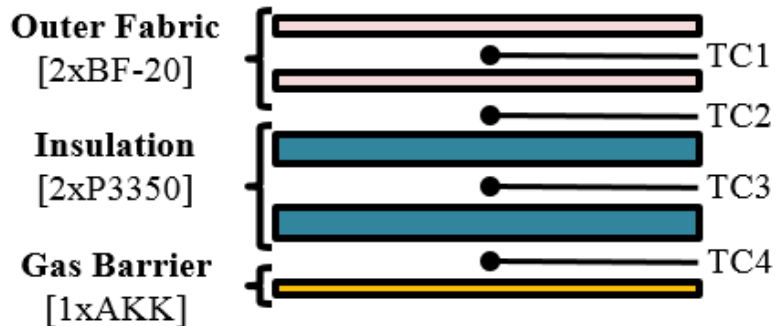
Figure 14: Layup 0 for Run 2259 with P3350 Insulation
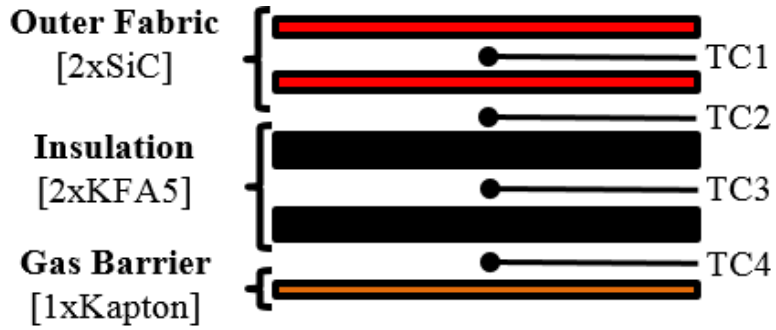
Figure 15: Layup 1 for Run 2627 with KFA5 Insulation
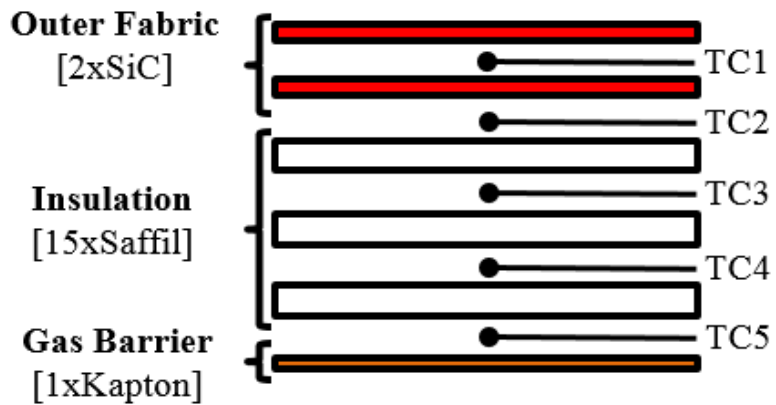
Figure 16: Layup 2 for Run 2822 with Saffil Insulation

Layup 0, Layup 1, and Layup 2 correspond to Test Case 0, Test Case 1, and Test Case 2 and are shown in Figure 14, Figure 15, and Figure 16, respectively. Layup 0 has two outer fabric layers made of Nextel BF-20 ceramic fabric, two insulation layers made of Pyrogel 3350 aerogel felt, and one gas barrier layer made of Aluminized Kapton Laminated to Kevlar (AKK). Layup 1 has two outer fabric layers made of Nicalon Silicon-Carbide (SiC) fabric, two insulation layers made of KFA5 carbon-felt, and one gas barrier layer made of Kapton. Layup 2 has identical outer fabric and gas barrier regions, but the insulation is composed of fifteen layers (three groups of five layers) of Saffil paper. Thermocouple (TC) locations are shown between FTPS layers with focus placed on the insulation region (TC2 – TC bondline). One FTPS thermal response model was created for

39

each of these three layups to predict in-depth temperatures and confirm understanding of the physical processes occurring during arc-jet experiments.

2.3.3 FTPS Thermal Response Model Description

Using the COMSOL Mutli-Physics software framework, the many physical processes experienced during arc-jet testing have been combined within one cohesive thermal model, which includes the governing equations for conservation of mass, momentum, and energy. Thermal-material property databases for FTPS layers are input into the model in tabular form as a function of temperature and pressure. These thermal-material properties were measured in a non-compressed state for FTPS outer fabric, insulation, and gas barrier materials.

The thermal response model includes convection, surface radiation, and solid/gas conduction through FTPS layers. While contact resistance is not modeled between FTPS layers, gas conduction has a much larger effect because FTPS outer fabric and insulation materials have significant porosity and permeability. The current model includes the capability to incorporate insulator pyrolysis gas flow and mass decomposition. Additionally, the pyrolysis gas species generated from decomposition are added to compute total pressure throughout the FTPS layup. Mass decomposition and pyrolysis gas flow are energy absorbing mechanisms that potentially lower temperature through a FTPS layup. Pyrogel aerogel felt and KFA5 carbon-felt exhibit similar decomposition and pyrolysis behavior, which must be accounted for in the thermal response model before accurate temperature predictions can be made. Thermal conductivity for insulator materials is made up of the sum of three components: solid conduction, gas conduction, and internal radiation. Specific heat, permeability, and porosity of insulation and gas barrier materials are determined experimentally and included in the thermal response model.

One thermal response model was created for each of the three layups considered in this chapter (Layup 0, Layup 1, and Layup 2). As mentioned, the primary motivation to perform

parameter estimation is to reduce thermal response model temperature prediction discrepancies by more accurately estimating these FTPS thermophysical properties during extreme regions of arc-jet testing. At these extremes, materials experience temperatures and pressures outside their known and tested limits, or in regions where the uncertainty in the measured properties is large. The following three sections demonstrate the application of the extended inverse multi-parameter estimation methodology to each thermal response model to improve in-depth temperature predictions within the FTPS insulation stack by updating key thermal-material property estimates.

2.4 Test Case 0: Proof-of-Concept Study of Extended Multi-Parameter Estimation Framework

As a proof-of-concept, a simplified version of the extended inverse multi-parameter estimation methodology was applied to Layup 0 shown in Figure 14. This study will be referred to as Test Case 0. First, a nominal analysis was performed to investigate the state of the arc-jet test data and specify which portion of Run 2259 would be considered in the LM objective function. Next, a transient uncertainty analysis was performed for the bondline thermocouple (TC 4) to investigate the contribution of each scale factor to the thermal response model's temperature prediction uncertainty. A sensitivity analysis was then performed to examine the linear correlations between scale factors. These analyses are used to minimize error in the TC4 prediction by selecting the appropriate thermophysical properties to estimate within the thermal model.

2.4.1 Nominal Analysis

The purpose of nominal analysis is to examine the integrity of the experimental data and define the time region that will be considered for inverse analysis. Figure 17 shows the test data for Run 2259 as solid lines for TC1, TC2, TC3, and TC4. This figure also shows the nominal thermal response model prediction for TC4 as a dashed line.
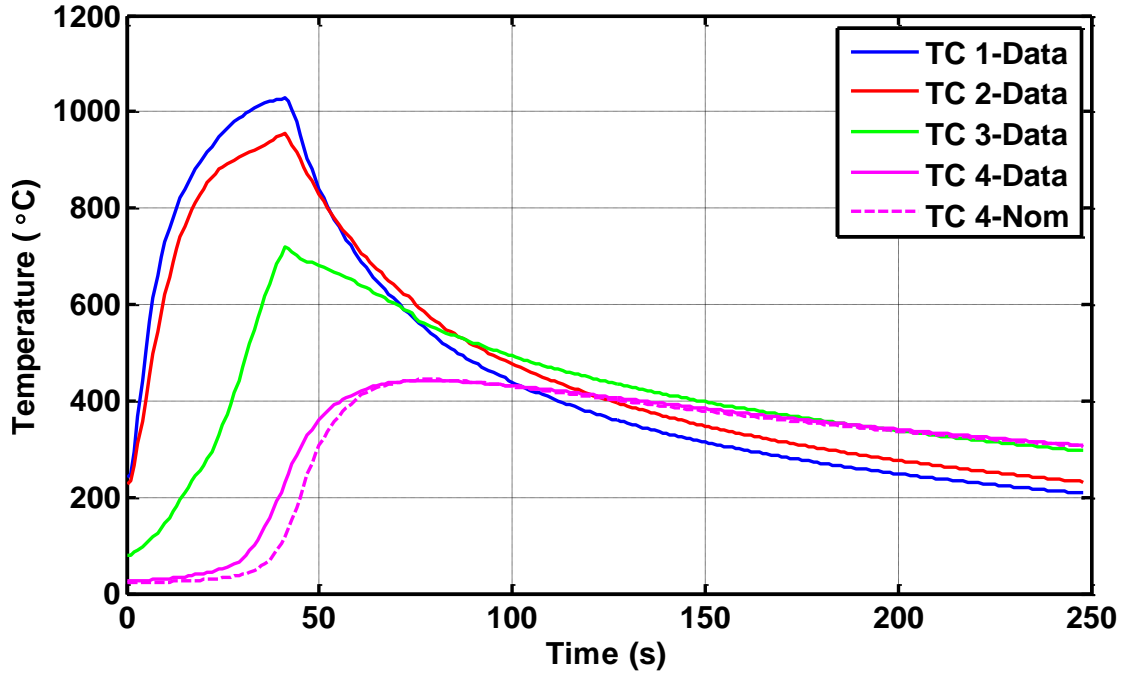
Figure 17: Run 2259 Nominal TC4 Temperature Prediction

The first thing to note is that this investigation uses the TC Driver Approach by applying the measured temperature profile of TC3 as a boundary condition for the prediction of TC4. A TC3 driver approach eliminates a great deal of model uncertainty by only calculating heat conduction between one layer of Pyrogel 3350 between TC3 and TC4.

Overall, the quality of the data is superb. Recorded data for TC1, TC2, TC3, and TC4 is smooth and continuous without breaks or noise. Normally, the selected time-domain for analysis starts when Layup 0 is injected into the flow at t = 0 seconds and ends when the model is retracted from the flow at approximately t = 45 seconds. As a proof-of-concept, this specific case will investigate a larger time domain, between model injection and the peak bondline (TC4) temperature at approximately t = 78 seconds. The additional computational cost to do this in Test Case 0 is small because only TC4 is analyzed.
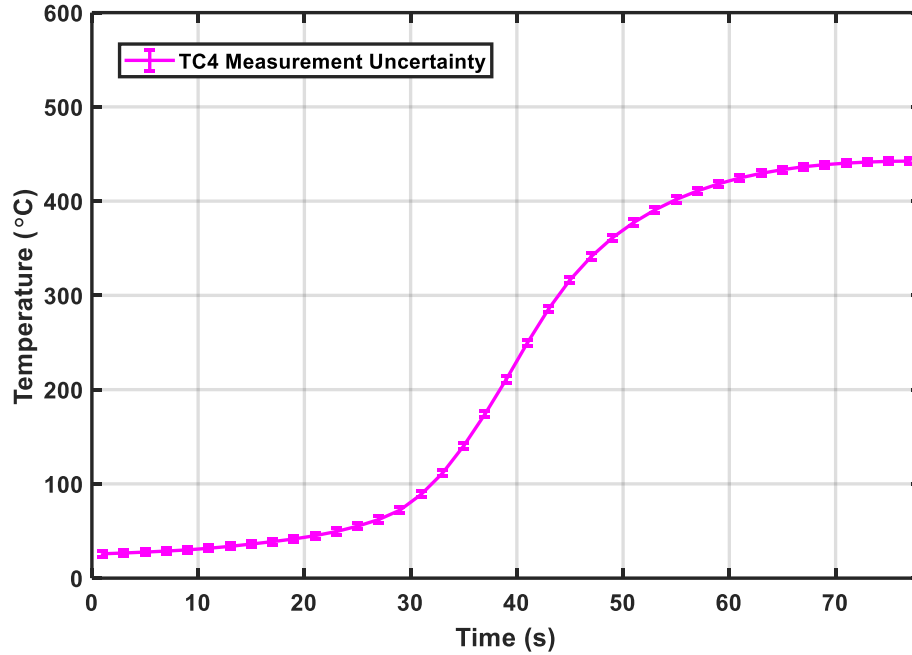
Figure 18: Run 2259 Measurement Uncertainty for TC4

Measurement uncertainty for the thermocouple of interest (TC4) is shown in Figure 18. Because TC4 is a Type K thermocouple, its measurement uncertainty is specified as 0.75% of the maximum measured value, resulting in an uncertainty of approximately ± 3.32 ºC. Representative error bars are shown for TC4 in Figure 18 for the specified time region between t = 0 seconds and t = 78 seconds illustrating that the temperature measurement uncertainty is extremely small.

2.4.2 Uncertainty Analysis

An uncertainty analysis was performed using a Monte Carlo technique for TC4 in Test Case 0. The purpose of this study was to evaluate how much each thermal-material property in a selected set effect the uncertainty of the TC4 thermal response model prediction. This method plots the relative uncertainty contribution for each thermal-material parameter as a function of time allowing the analyst to decide which parameters are significant drivers of the temperature prediction response. Large contributors are then considered for sensitivity analysis and uncertainty analysis afterwards.

43

In this simplified proof-of-concept study, only four thermal-material parameters were considered. These include insulator thermal conductivity, insulator specific heat, insulator density, and gas barrier specific heat. The resulting uncertainty analysis chart, shown in Figure 19, was produced after performing 750 Monte Carlo runs.
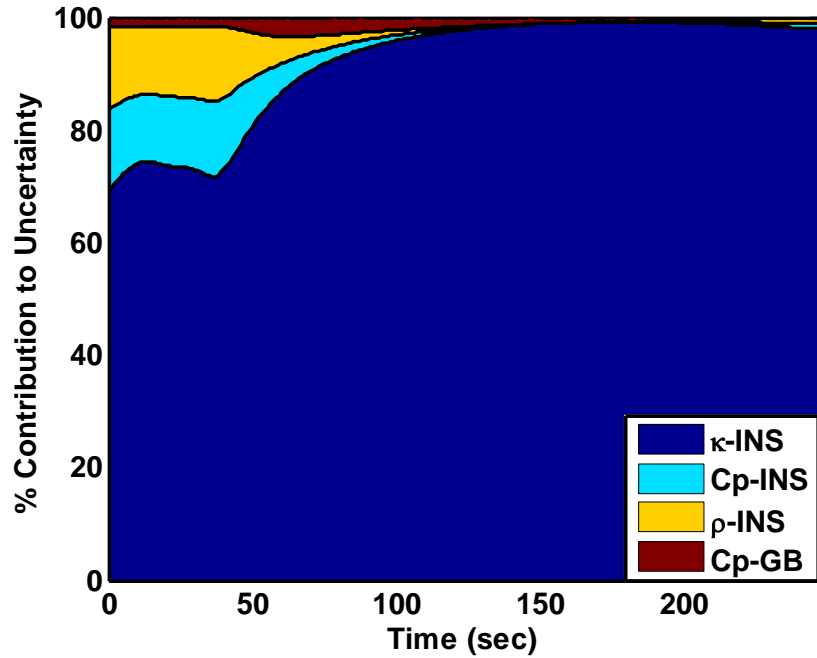
Figure 19: Run 2259 TC4 Uncertainty Analysis

The following method determines if the number of Monte Carlo runs performed is adequate by showing approximate convergence for TC4's peak temperature distribution. To do so, one must compile a cumulative histogram of peak TC4 temperatures after each Monte Carlo run. The standard deviation of each histogram can be calculated and plotted as a function of the number of Monte Carlo simulation runs. As this plot converges to a stable value standard deviation, one gains confidence that the TC4 peak temperature distribution is no longer changing significantly with each additional Monte Carlo run, and therefore, the number of runs is adequate. Figure 20 shows convergence of the TC4 peak temperature distribution standard deviation after 750 runs, which gives confidence that the TC4 distribution ceases to change and has been adequately captured. This lends confidence

in the uncertainty analysis shown in Figure 19 and ensures that an appropriate number of Monte Carlo runs was performed.
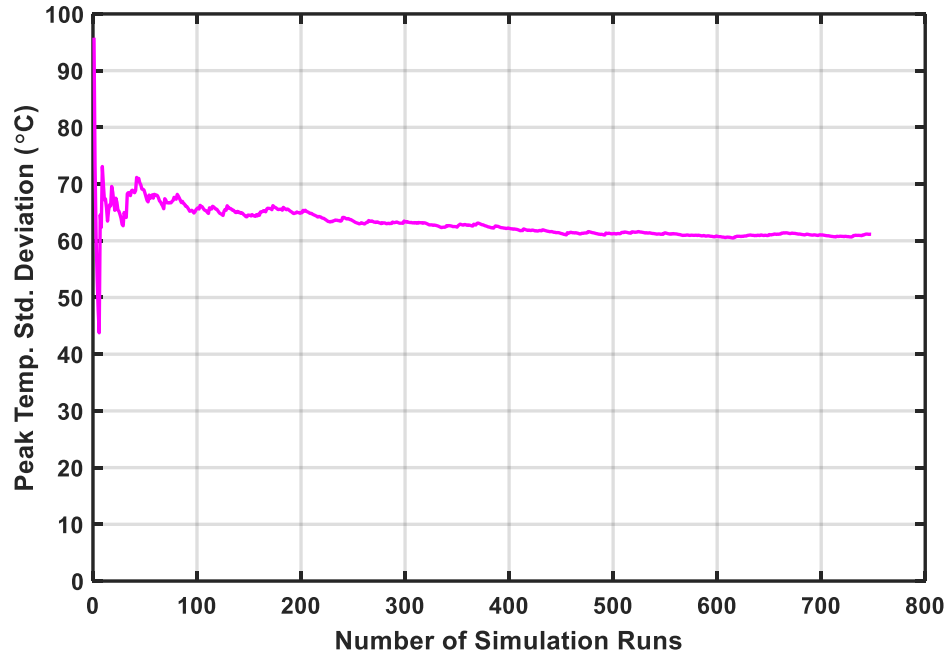
Figure 20: Run 2259 Peak Temperature Distribution Standard Deviation Convergence for TC4

This uncertainty analysis illustrates the time domain between $t = 0$ seconds to $t = 250$ seconds to show some important behavioral trends. It is important to first note that insulator thermal conductivity is by far the largest contributor, followed by insulator specific heat, insulator density, and gas barrier specific heat. It's also interesting to note that the insulator thermal conductivity becomes a larger contributor to thermal response model TC4 prediction uncertainty with time as the TC4 temperature peaks and begins to cool down. Additionally, the uncertainty analysis displayed in Figure 19 suggests that the gas barrier specific heat scale factor contributes the least to prediction uncertainty and can be neglected for sensitivity analysis and inverse analysis.

2.4.3 Sensitivity Analysis

A sensitivity analysis was performed on TC4 in Figure 21 using the remaining parameters from uncertainty analysis. This figure displays relative sensitivities of scale factors produced by an off-nominal perturbation to scale factor parameters as a function of time for each thermocouple. Scale factor parameters that exhibit strong correlation should not be estimated simultaneously due to linear independency.
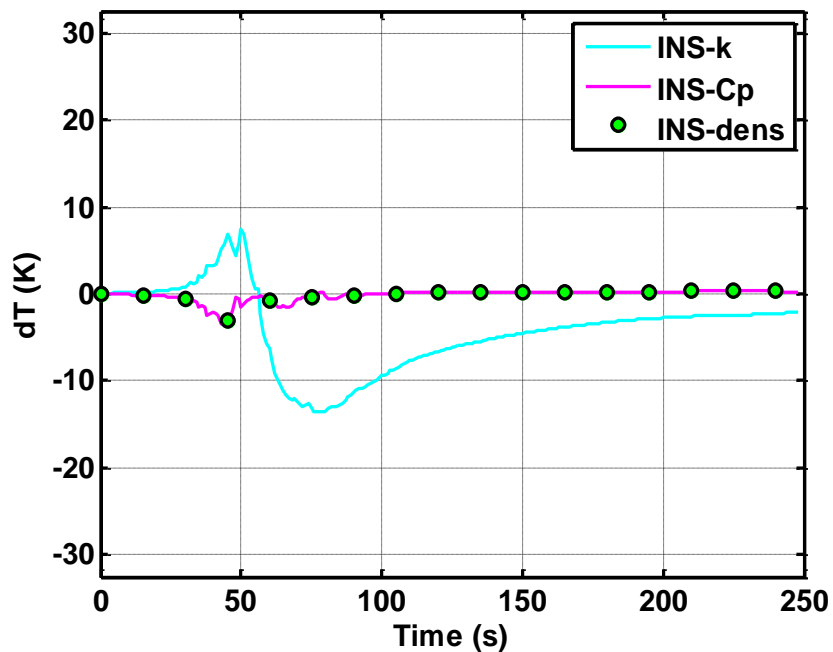
Figure 21: Run 2259 TC4 Sensitivity Analysis

From this analysis, one can clearly identify a 100% correlation between the insulator specific heat scale factor and the insulation density scale factor. The insulator thermal conductivity scale factor has a somewhat negative correlation with the insulator specific heat scale factor, but this correlation is much less significant. Because insulator specific heat and insulator density scale factors have such a strong correlation, one must be eliminated before moving on to inverse analysis. The insulator specific heat scale factor had a slightly larger contribution to uncertainty than the insulator density scale factor,

making it more attractive to carry on to the next step. For this reason, the insulator density scale factor is neglected, and the insulator thermal conductivity and specific heat scale factors are carried into inverse analysis.

2.4.4 Inverse Analysis

This discussion focuses on the results from performing inverse analysis using insulator thermal conductivity and specific heat scale factors. The previous nominal analysis helped define the analysis time-domain between model injection at t=0 seconds and TC4 peak temperature at t = 78 seconds. The objective function for the inverse analysis is the sum of squared errors (SSE) between the TC4 measurement and thermal response model estimation. Figure 22 shows the inverse analysis iteration history while Figure 23 shows the TC4 error-minimized temperature prediction obtained from inverse analysis.
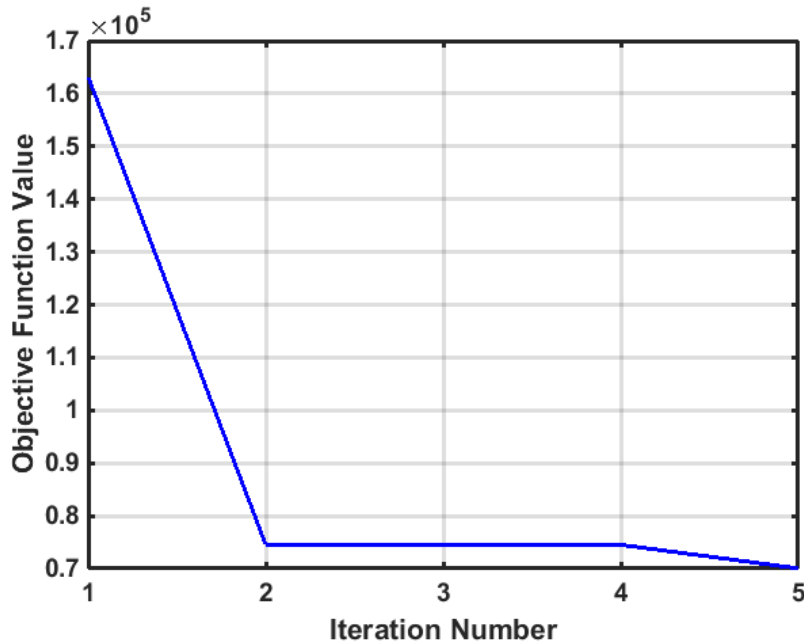
Figure 22: Run 2259 Inverse Analysis Objective Function Value
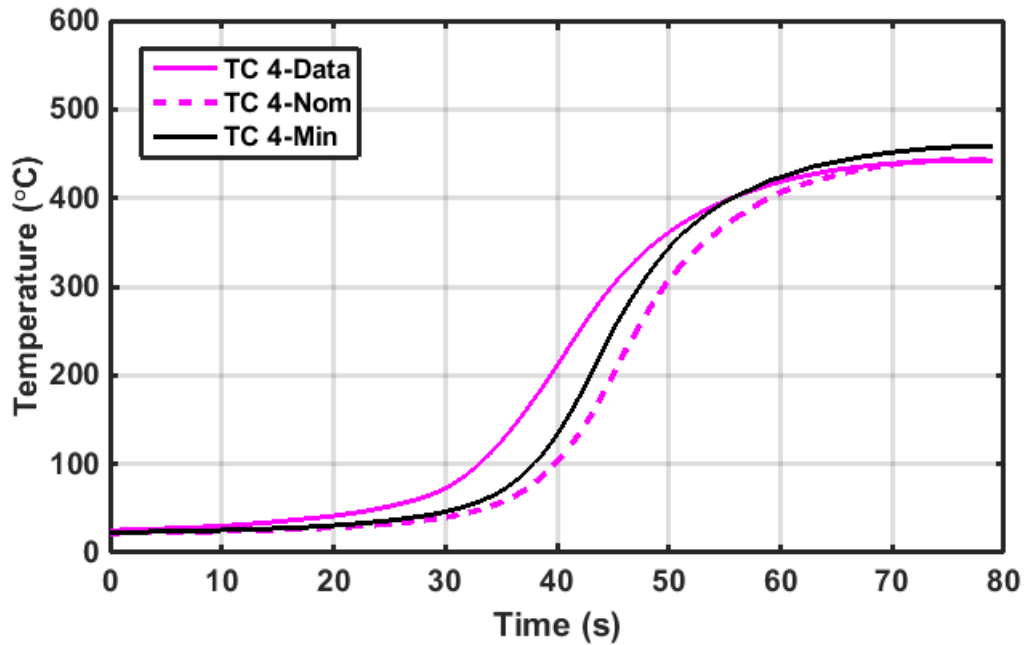
Figure 23: Run 2259 Inverse Analysis for Error-Minimized TC4 Prediction

As shown in Figure 22, the objective function was reduced by approximately 50% after the first iteration and slightly reduced further after additional iterations. The resulting "TC4-Min" temperature prediction for TC4 is shown in Figure 23. This error-minimized prediction shows reasonably better closeness to the "TC4-Data" temperature measurement curve, especially between 30 seconds and 60 seconds.

Successful error-minimization is a promising result that sets the stage for extending this method to higher fidelity physics models, multiple thermocouples, and various FTPS insulators.

2.5 Test Case 1: Extended MPE Framework Applied to KFA5 FTPS Insulation Thermal Response Model

While Test Case 0 is an encouraging result, it is also necessary to acknowledge that most FTPS insulation stacks have more than one thermocouple temperature prediction that needs to be improved. The full version of the extended inverse multi-parameter estimation methodology considers multiple thermocouple and improves all temperature predictions

simultaneously. The following sections detail the results and discussion from applying the methodology to Layup 1 in Test Case 1. The insulation stack in this layup is composed of two layers of KFA5 carbon felt as shown in Figure 15.

2.5.1 Nominal Analysis

The nominal analysis for Test Case 1 begins by investigating the quality of the arc-jet thermocouple data shown in Figure 24. Here, the solid lines represent experimental data and the dashed lines represent initial thermal response model predictions. The TC Driver approach has been applied to Test Case 1 at the TC2 thermocouple location, which sits between the last layer of outer fabric and the first layer of insulation shown in Figure 15. The next two thermocouples, TC3 and TC4, are predicted based on the application of TC2 as the temperature boundary condition. Initially, one can see that initial thermal response model predictions appear low and could be improved.
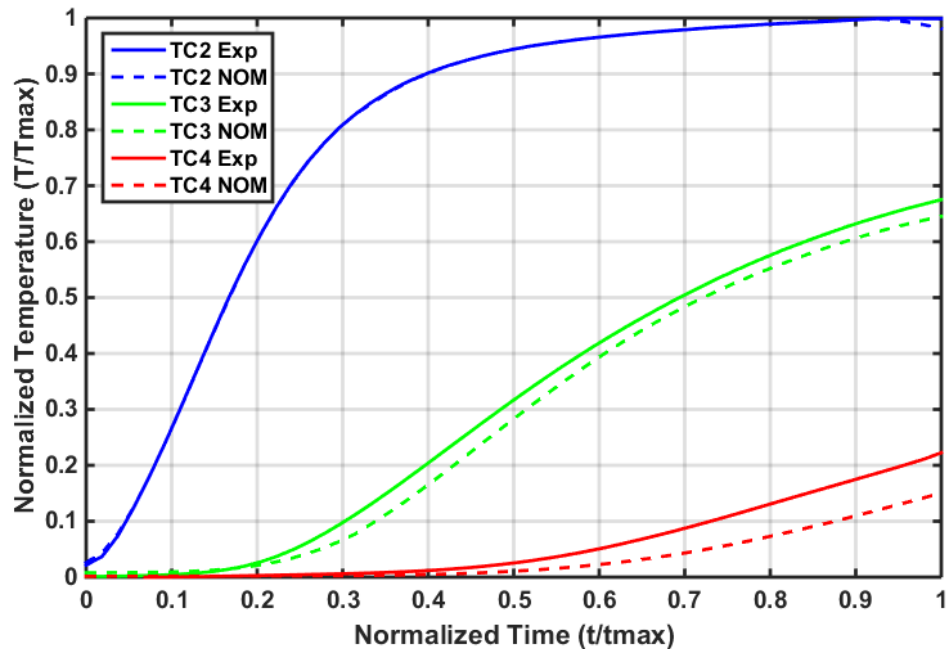
Figure 24: Run 2627 Nominal TC3 and TC4 Temperature Predictions

After examining Figure 24, the reader will notice that the time and temperature are normalized to protect the integrity of the data. For context, one can assume that the maximum temperature and maximum time are similar to the nominal analysis for Test Case 0 shown in Figure 17. The quality of the temperature data for nominal analysis of Test Case 1, shown in Figure 24, is very good. Much like the previous test case, the thermocouple data in Test Case 1 is smooth and continuous without any breaks or bumps. This will make it more straightforward to perform uncertainty, sensitivity, and inverse analysis. Here, t = 0 occurs when the model is injected into the flow and t = 1 occurs when the model is retracted.
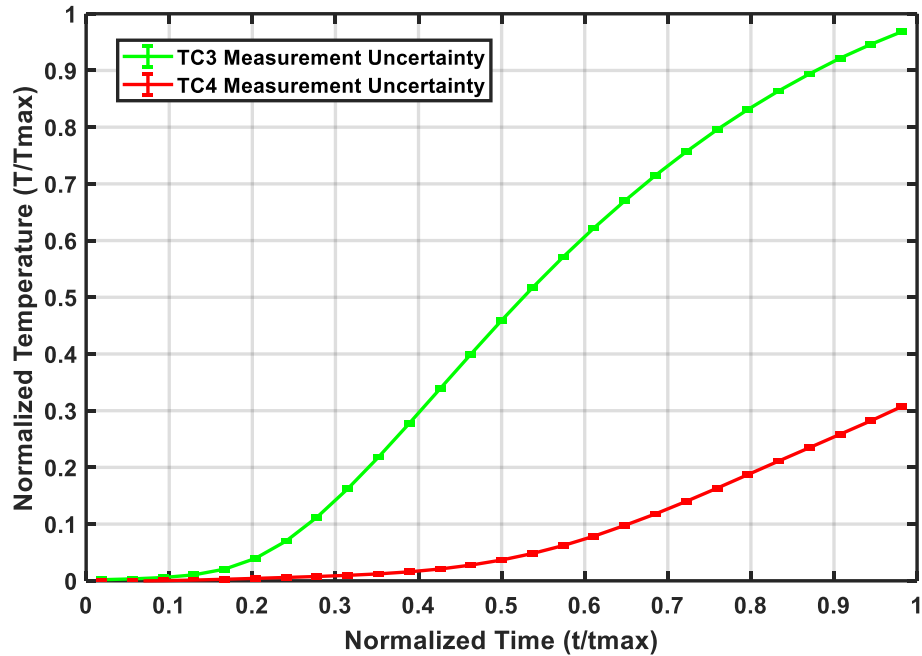
Figure 25: Run 2627 Measurement Uncertainty for TC3 and TC4

Measurement uncertainty for the thermocouples of interest (TC3 and TC4) are shown in Figure 25. Because TC3 is a Type R thermocouple, its measurement uncertainty is specified as 0.25% of the maximum measured value, resulting in an uncertainty of approximately ± 2.45 ℃. TC4 is a Type K thermocouple with a measurement uncertainty of approximately ± 2.42 ℃. Representative error bars are shown for TC3 and TC4 in Figure

50

25 for the specified normalized time region between t = 0 and t = 1 illustrating that the temperature measurement uncertainty is extremely small for both thermocouples.

2.5.2 Uncertainty Analysis

Scale factors with the highest relative contribution to uncertainty drive the majority of the thermal model's temperature prediction response. As such, these key scale factors are ideal for inverse analysis because the temperature predictions can be improved the most by obtaining better estimates for driving thermal-material property scale factors.

Because this dissertation is focused on solving the material response problem of the insulation stack, the thermal-material properties included in this set are associated with either the insulator or the gas barrier. The thermal-material property scale factors included in Test Case 1 correspond to KFA5 insulation thermal conductivity, KFA5 insulation specific heat, KFA5 insulation permeability, KFA5 insulation porosity, Kapton gas barrier thermal conductivity, and Kapton gas barrier specific heat. Additionally, the KFA5 insulation activation energy is considered here in the scale factor set for uncertainty analysis to show its contribution to thermal response model prediction uncertainty relative to other well-known thermal material properties. Table 2 provides a summary of the thermal-material scale factor set evaluated for Test Case 1.

Table 2: Run 2627 Uncertainty Analysis Scale Factor Distribution Statistics

Distribution Statistics	KFA5 k (SF)	KFA5 Cp (SF)	KFA5 Perm (SF)	KFA5 Por (SF)	GB k (SF)	GB Cp (SF)	KFA5 Ea (SF)
(μ) Mean	1	1	1	1	1	1	1
(σ) Std. Dev.	0.100	0.050	0.050	0.010	0.050	0.025	0.044
($+3\sigma$) Value	1.300	1.150	1.150	1.030	1.150	1.075	1.132
(-3σ) Value	0.700	0.850	0.850	0.970	0.850	0.925	0.868

Each parameter in Table 2 is a multiplicative scale factor that adjusts the corresponding thermal-material property. The following uncertainty analysis is performed using the Monte Carlo method, which randomly selects combinations of scale factors according to a prescribed probability distribution. Here, the first six scale factors in Table 2 are defined by normal distributions with a mean of 1. The corresponding standard deviations for each scale factor were obtained using expert opinion from members of the HIAD FTPS analysis team at NASA LaRC. The activation energy scale factor is assumed to be distributed with a t-distribution with a mean of 1 and a standard deviation of 0.044.

A scale factor representing KFA5 specific heat was chosen for the following analysis over a KFA5 density scale factor because density constantly changes within the KFA5 thermal response model to represent mass loss due to decomposition. This would make parameter estimation with a density scale factor extremely difficult, and as a result, a KFA5 specific heat scale factor was used instead. If the outer fabric region was considered in this analysis, one may choose to estimate a scale factor for outer fabric emissivity. Considering emissivity is similar to porosity because the value of each cannot exceed 1. As a result, the analyst would need to ensure that the maximum scaled value for emissivity was no greater than 1 by choosing feasible uncertainty bounds for the outer fabric emissivity scale factor normal distribution.

Uncertainty analysis was completed using 2000 Monte Carlo simulations. Each simulation randomly selected each scale factor according to their defined distributions. Relative contributions to uncertainty were calculated for each scale factor using the relationship defined in Equation 4. Figure 26 and Figure 27 show the resulting uncertainty analysis as a function of time for TC3 and TC4, respectively.
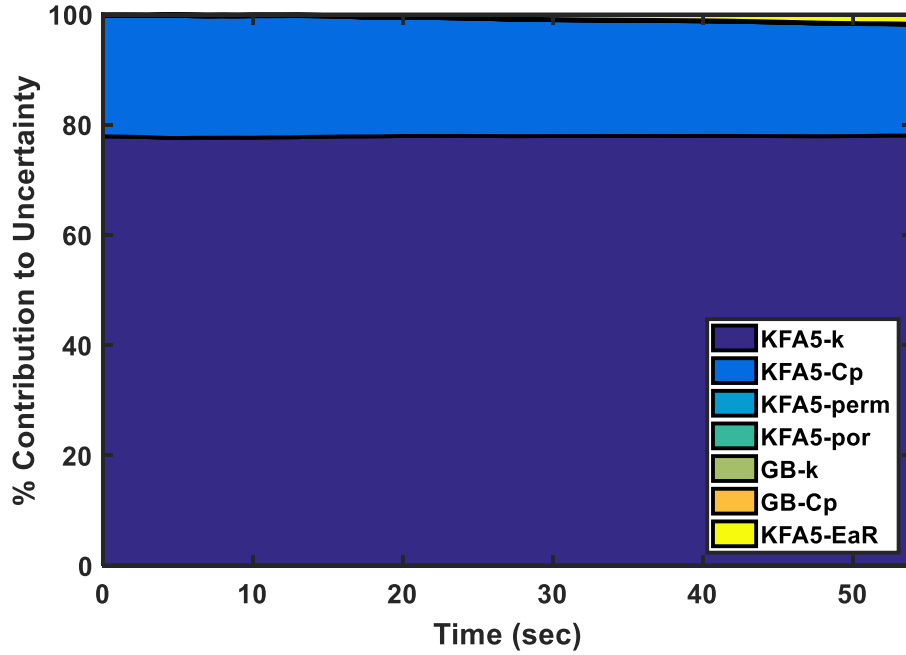
Figure 26: Run 2627 TC3 Uncertainty Analysis
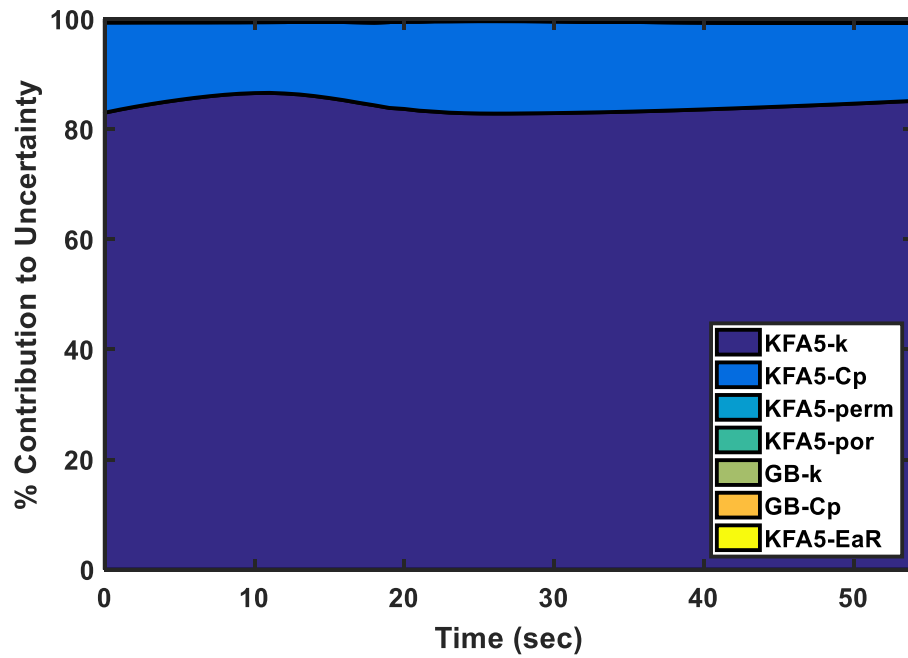
Figure 27: Run 2627 TC4 Uncertainty Analysis

The same method from Test Case 0 is used to determine if the number of Monte Carlo runs performed is adequate. Like before, the objective of the method is to show

approximate convergence for peak temperature distributions for thermocouples analyzed in the uncertainty analysis. Figure 28 shows convergence of the TC3 and TC4 peak temperature distribution standard deviations after 2000 Monte Carlo runs, which gives confidence that both distributions cease to change and have been adequately captured. This lends confidence in the uncertainty analyses shown in Figure 26 and Figure 27 while ensuring that an appropriate number of Monte Carlo runs was performed.
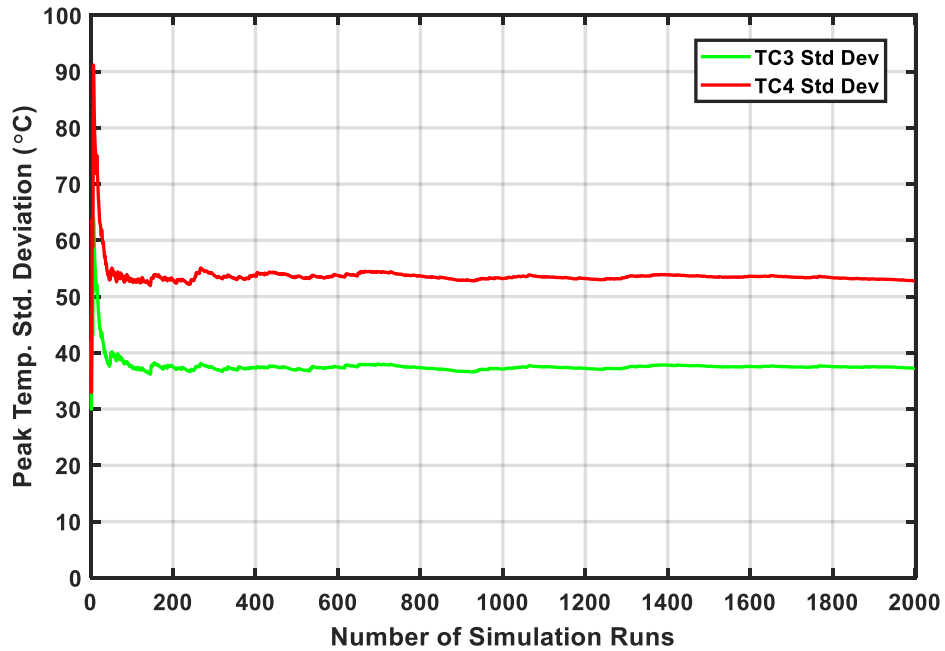
Figure 28: Run 2627 Peak Temperature Distribution Standard Deviation Convergence for TC3 and TC4

Figure 26 shows that there are three clear scale factors that drive TC3 and TC4 prediction response, including KFA5 thermal conductivity, specific heat, and activation energy scale factors. For TC3, thermal conductivity accounts for approximately 78% of prediction uncertainty, followed by approximately 20% from specific heat and approximately 2% from activation energy. For TC4, thermal conductivity accounts for approximately 80% of prediction uncertainty and specific heat accounts for the remaining 20%.

It is expected that both thermal conductivity and specific heat drive the response because these two parameters define heat conduction, which is the main mode of heat transfer through insulator layers. Because KFA5 is a carbon felt insulator that decomposes when exposed to high temperatures, it is also expected that its activation energy is a significant driver to overall temperature prediction response. During high-temperature decomposition from oxidation, carbon atoms from the KFA5 combine with oxygen atoms, creating a hot carbon-oxygen gas that carries thermal energy through the top face of the sample and out of the layup. It is believed that this advection process is the main reason why KFA5 performs well at higher temperatures – it encourages physical heat removal through a gaseous medium. The higher the temperature, the more decomposition gas products are created, and the more heat is removed from the layup due to advection.

This behavior is shown in Figure 26 as activation energy starts small and becomes a larger contributor as the TC3 temperature increases. The peak temperature for TC3 is significantly higher than TC4 because TC3 is closer to the heat source. As a result, activation energy does not contribute nearly as much to uncertainty here. For TC4, heat conduction dominates advection as the primary mode of heat transfer. The temperature in TC4 is not high enough to induce the formation of significant decomposition gases that could potentially remove heat from the system.

The purpose of including the KFA5 activation energy scale factor as a parameter in uncertainty analysis was to show its relative performance to other scale factors and define associated decomposition behaviors. Because activation energy is experimentally determined in Chapter 3, it is a known quantity in this investigation that will not be estimated with inverse analysis. Therefore, it is not considered in the following uncertainty and sensitivity analyses.

2.5.3 Sensitivity Analysis

A sensitivity analysis was performed for the first six scale factors listed in Table 2. Scale factors were perturbed ±1% and temperature predictions were obtained for both perturbations. The central difference was taken between perturbed temperature predictions using Equation 5. The resulting temperature differences (dT) are shown for all six scale factors at TC3 and TC4 locations in Figure 29 and Figure 30.
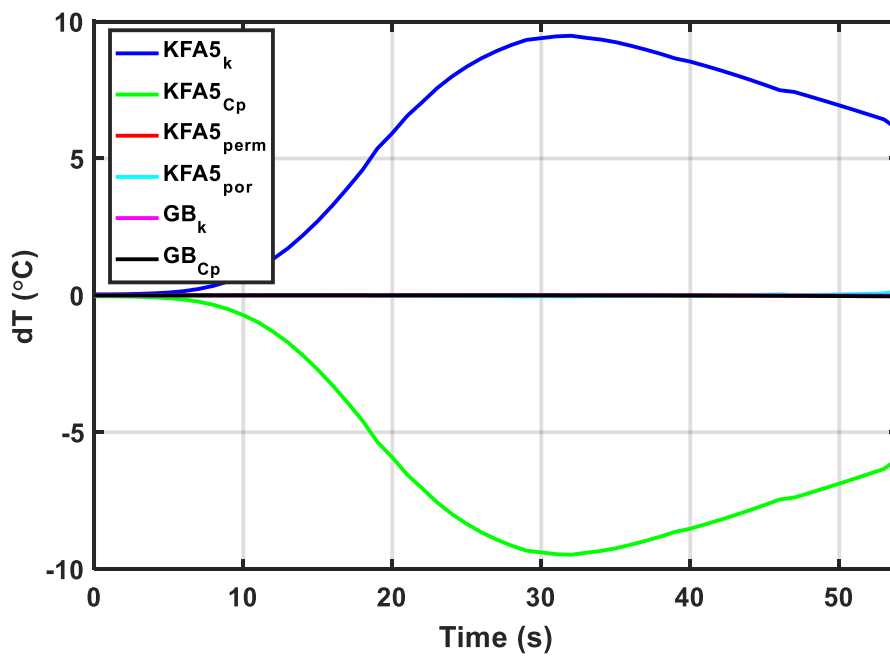
Figure 29: Run 2627 TC3 Sensitivity Analysis
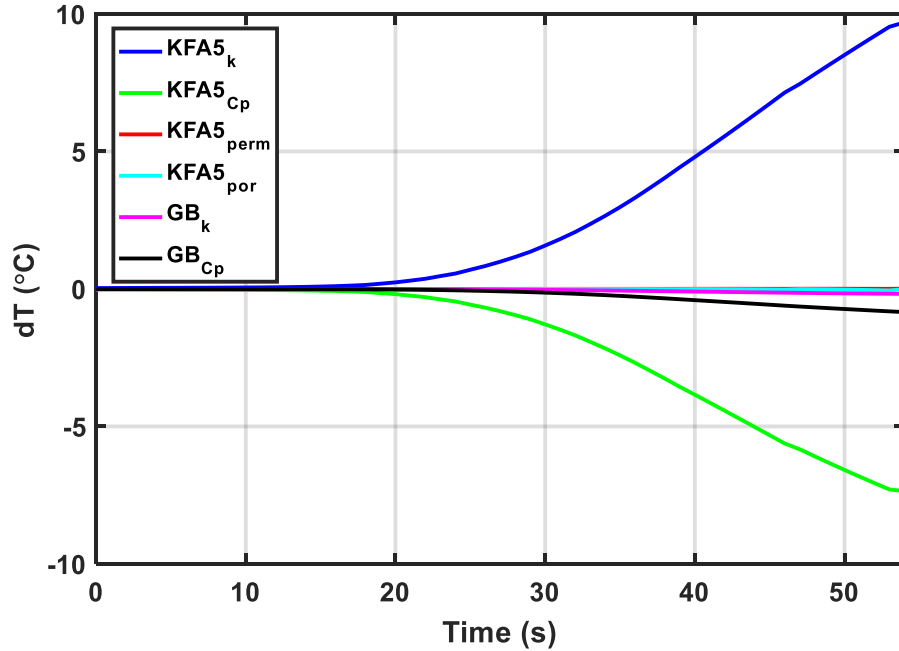
Figure 30: Run 2627 TC4 Sensitivity Analysis

These figures illustrate the temperature difference from perturbed temperature predictions for each scale factor as a function of time. After examining the figures, one can see that KFA5 thermal conductivity and specific heat scale factors have a negative correlation close to 100%. At the TC3 location, the next largest contributor is the KFA5 porosity scale factor while remaining contributors are small. At the TC4 location, the next largest contributor is the Gas Barrier (GB) specific heat scale factor, followed by the GB thermal conductivity scale factor and the KFA5 porosity scale factor. Table 3 shows the relative linear dependencies between scale factors in the form of a correlation table. This table has averaged correlation tables from TC3 and TC4 together.

Table 3: Run 2627 Sensitivity Analysis Averaged Correlation Coefficients for TC3 and TC4

TC3-4 Avg	KFA5 k	KFA5 Cp	KFA5 Perm	KFA5 Por	GB k	GB Cp
KFA5-k	1					
KFA5-Cp	-0.9998	1				
KFA5-Perm	0.5556	-0.5545	1			
KFA5-Por	-0.5098	0.5099	0.0985	1		
GB-k	-0.6554	0.6526	-0.8456	0.0130	1	
GB-Cp	-0.6463	0.6429	-0.8457	0.0131	0.9992	1

Using the information presented, the designer must make an intelligent decision to find which scale factors will be used for inverse analysis. It is advantageous to use scale factors that were large contributors in the uncertainty analysis. One must also make sure the selected scale factors are not linearly dependent as this will lead to issues with convergence stability and solution uniqueness. Although KFA5 thermal conductivity and KFA5 specific heat scale factors were the largest contributors to uncertainty, they are nearly 100% correlated. As a result, one of these parameters must be neglected and replaced. Because the KFA5 thermal conductivity scale factor contributed approximately 80% to uncertainty for both TC3 and TC4, it will move forward to inverse analysis. Using the KFA5 specific heat scale factor would not be advantageous because it contributed only 20% to uncertainty for both TC3 and TC4, which gives the scale factor much less leverage to improve temperature predictions. The KFA5 specific heat scale factor will be neglected and replaced by a less correlated scale factor.

According to Table 3, the parameter that is least correlated with the KFA5 thermal conductivity scale factor for both TC3 and TC4 is the KFA5 porosity scale factor. As a result, both KFA5 thermal conductivity and KFA5 porosity scale factors will be considered to demonstrate the inverse analysis component of the extended multi-parameter estimation methodology applied to Test Case 1.

2.5.4 Inverse Analysis

For Test Case 1, the analyst used information from uncertainty and sensitivity analyses to select two scale factors to include in inverse analysis. The thermal-material properties these scale factors represent are KFA5 thermal conductivity and KFA5 porosity. The thermal conductivity scale factor was selected using uncertainty analysis results that showed it contributes approximately 80% to thermal response model prediction uncertainty for both TC3 and TC4. The porosity scale factor was selected using sensitivity analysis results that showed it was the least correlated parameter to thermal conductivity. Using these two scale factors together for inverse analysis ensure that the methodology will have a large effect on thermal response model predictions and will not experience convergence instability or issues with solution uniqueness.
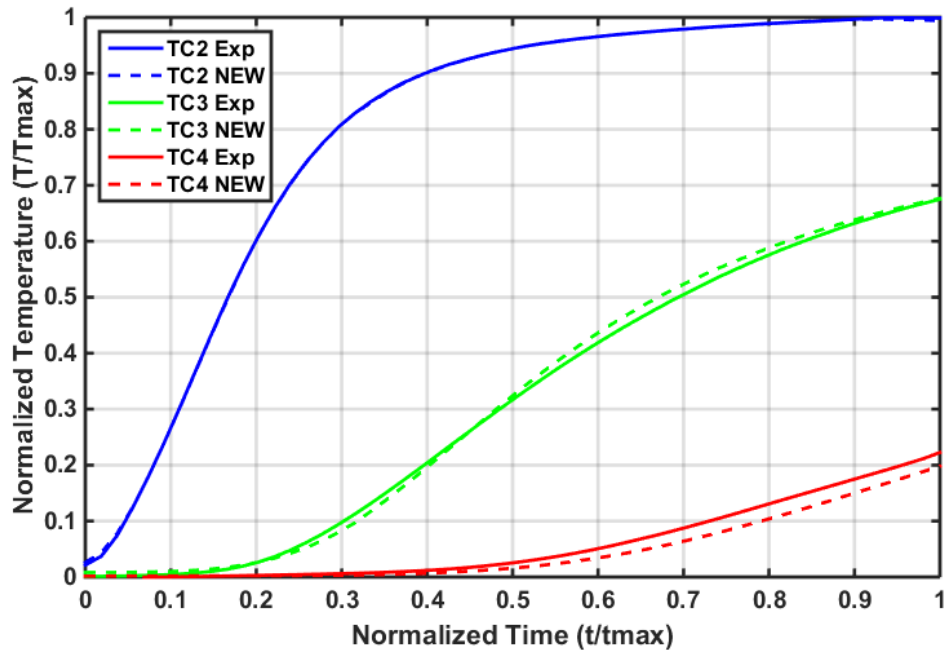
Figure 31: Run 2627 Inverse Analysis for Error-Minimized TC3 and TC4 Predictions

Inverse multi-parameter estimation was performed on the Layup 1 thermal response model for Test Case 1 using Equations 6 – 14 described earlier. The objective of this

procedure was to minimize error between arc-jet thermocouple temperature measurements and thermal response model temperature predictions. Iterations were performed until the stopping criteria was met specified in Equations 15 – 16. After the procedure was completed, the final scale factor values for KFA5 thermal conductivity and porosity were 1.138 and 0.97, respectively. Using these scale factors, the improved thermal response model temperature predictions are shown in Figure 31.

Table 4: Run 2627 Comparison of Root Mean Square Error (RMSE) of TC3 and TC4 Predictions

Prediction	TC3 (°C)	TC4 (°C)	Avg. (°C)	Avg. (%) Improved
Nominal	36.44	52.83	45.38	NA
Error-Minimized	15.73	23.28	19.87	56.22%

Comparing the improved temperature predictions in Figure 31 with nominal predictions in Figure 24 shows significant reduction in prediction error. Table 4 summarizes inverse analysis results by comparing the RMSE of TC3 and TC4. The extended inverse multi-parameter estimation methodology suggested slightly increasing the thermal conductivity scale factor from a value of 1 to a value of approximately 1.138 to reduce prediction error. This makes intuitive sense because nominal temperature predictions for TC3 and TC4 were significantly lower than arc-jet thermocouple measurements due to possible inaccuracies in thermal conductivity measurements.

Obtaining a higher estimate for thermal conductivity and a slightly lower estimate for porosity increased temperature predictions as a function of time to be approximately 56.22% closer to arc-jet thermocouple temperature measurements. This value was obtained by taking the RMSE at each time step for TC3 and TC4 nominal predictions (45.38 °C) and error-minimized predictions (19.87 °C) and calculating the relative percent reduction after improvement. This proves that using the extended inverse multi-parameter estimation

methodology can feasibly improve multiple temperature predictions simultaneously in complex FTPS thermal response models.

2.6 Test Case 2: Extended MPE Framework Applied to Saffil Paper FTPS Insulation Thermal Response Model

Test Case 1 was an encouraging demonstration of the extended inverse-parameter estimation methodology. In this section, the extended inverse multi-parameter estimation methodology is applied to a thermal response model for Layup 2 containing multiple layers of Saffil insulation. This study is referred to as Test Case 2.

2.6.1 Nominal Analysis

Like before, the nominal analysis for Test Case 2 begins by investigating the quality of the arc-jet thermocouple data shown in Figure 32. Here, the solid lines represent experimental data and the dashed lines represent initial thermal response model predictions. The TC Driver approach has been applied to Test Case 2 at the TC2 thermocouple location, which sits between the last layer of outer fabric and the first layer of insulation shown in Figure 16. The next three thermocouples (TC3, TC4, and TC5) are predicted based on the application of TC2 as the temperature boundary condition. Initially, one can see that initial thermal response model predictions are slightly higher than arc-jet thermocouple measurements.
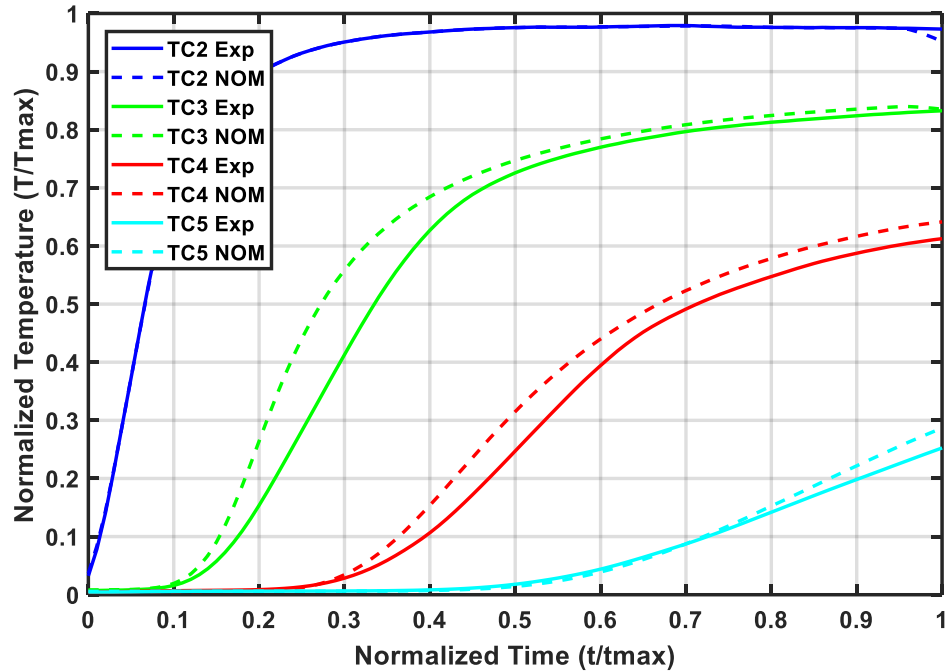
Figure 32: Run 2822 Nominal TC3, TC4, and TC5 Temperature Predictions

After examining Figure 32, the reader will notice that the time and temperature are normalized. Like previous test cases, one can assume that the maximum temperature and maximum time are similar to the nominal analysis for Test Case 0 shown in Figure 17. The quality of the temperature data for nominal analysis of Test Case 2 is very good. Much like the previous test cases, the thermocouple data in Test Case 2 is smooth and continuous without any breaks or bumps. This will make it more straightforward to perform upcoming uncertainty, sensitivity, and inverse analyses. The time domain investigated here begins at FTPS model injection (t = 0) and ends at model retraction (t = 1).
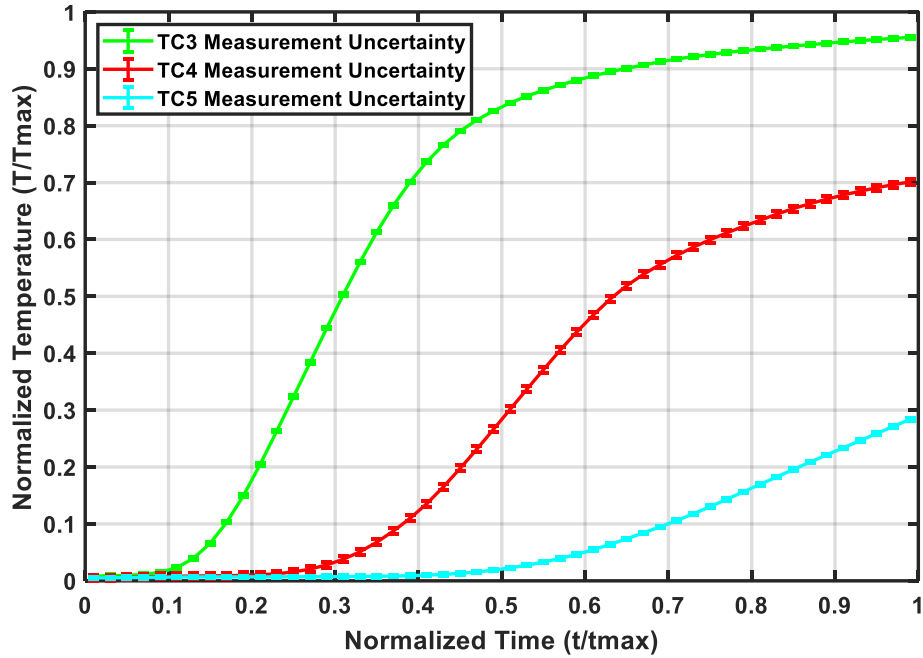
Figure 33: Run 2822 Measurement Uncertainty for TC3, TC4, and TC5

Measurement uncertainty for the thermocouples of interest (TC3, TC4, and TC5) are shown in Figure 33. TC3 is a Type R with a measurement uncertainty of approximately ± 3.23 ℃. TC4 and TC5 are both Type K thermocouples with measurement uncertainties of approximately ± 7.12 ℃ and ± 2.94 ℃, respectively. Representative error bars are shown for TC3, TC4, and TC5 in Figure 33 for the specified normalized time region between t = 0 and t = 1 illustrating that the temperature measurement uncertainty is extremely small for all three thermocouples.

2.6.2 Uncertainty Analysis

The thermal-material property scale factors included in Test Case 2 include to Saffil insulation thermal conductivity, Saffil insulation specific heat, Saffil insulation permeability, Saffil insulation porosity, Kapton gas barrier thermal conductivity, and Kapton gas barrier specific heat. Table 5 provides a summary of the thermal-material scale factor set evaluated for Test Case 2.

Table 5: Run 2822 Uncertainty Analysis Scale Factor Distribution Statistics

Distribution Statistics	SAF k (SF)	SAF Cp (SF)	SAF Perm (SF)	SAF Por (SF)	GB k (SF)	GB Cp (SF)
(μ) Mean	1	1	1	1	1	1
(σ) Std. Dev.	0.100	0.050	0.050	0.010	0.050	0.025
(+3σ) Value	1.300	1.150	1.150	1.030	1.150	1.075
(-3σ) Value	0.700	0.850	0.850	0.970	0.850	0.925

Each parameter in Table 5 is a multiplicative scale factor that adjusts the corresponding thermal-material property. This uncertainty analysis is performed using the Monte Carlo method assuming that the six scale factors in Table 5 are defined by normal distributions with a mean of 1. The corresponding standard deviations for each scale factor were obtained using expert opinion from members of the HIAD FTPS analysis team at NASA LaRC. Again, the corresponding ±3σ values are listed for the reader's convenience.

The following uncertainty analysis was completed using 2000 Monte Carlo simulations. Each simulation randomly selected each scale factor according to their defined distributions. Relative contributions to uncertainty were calculated for each scale factor using the relationship defined in Equation 4. Figure 34, Figure 35, and Figure 36 show the resulting uncertainty analysis as a function of time for TC3, TC4, and TC5, respectively.
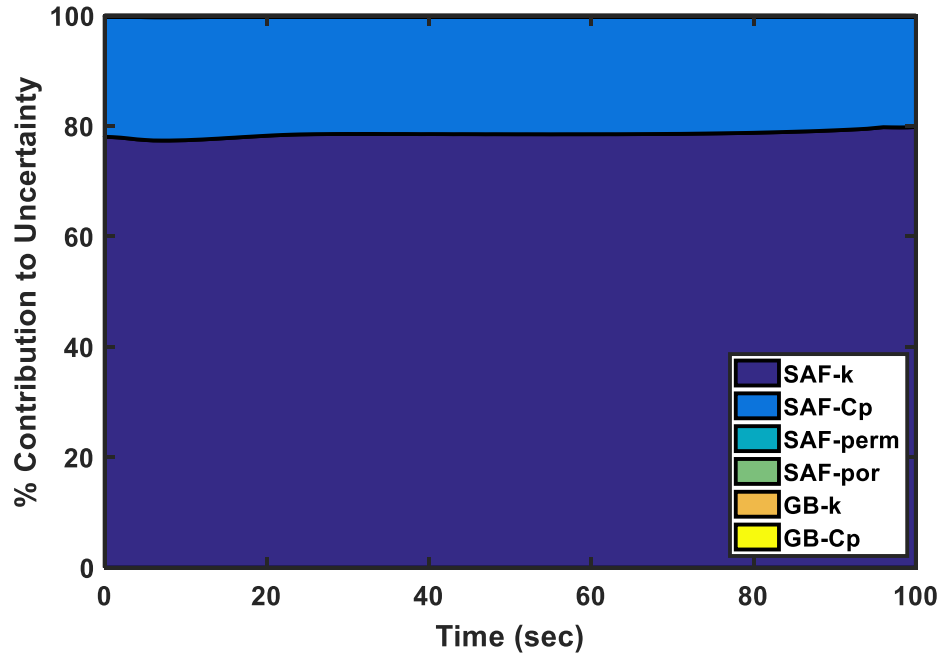
Figure 34: Run 2822 TC3 Uncertainty Analysis
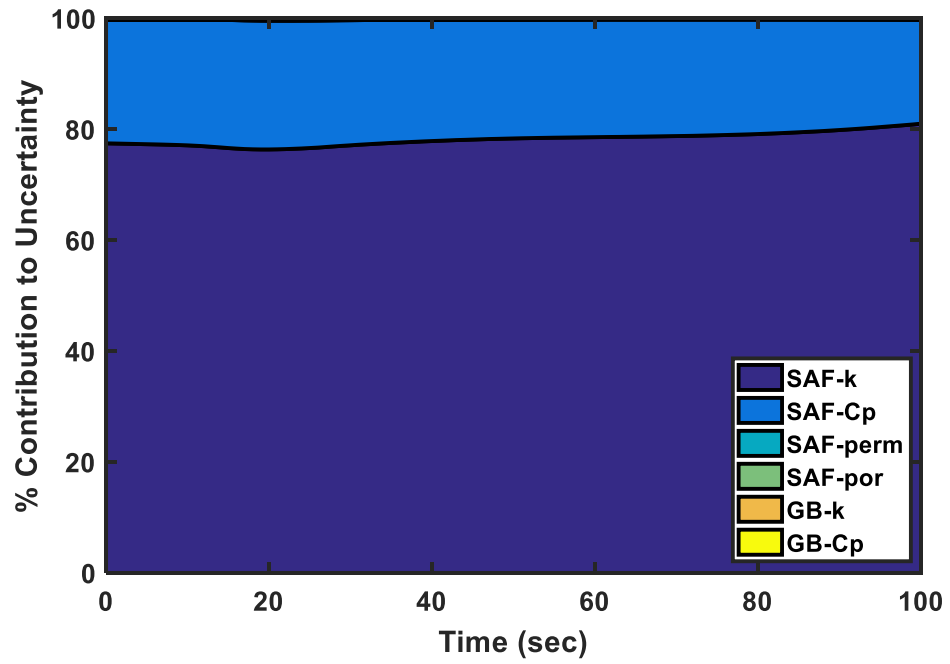
Figure 35: Run 2822 TC4 Uncertainty Analysis
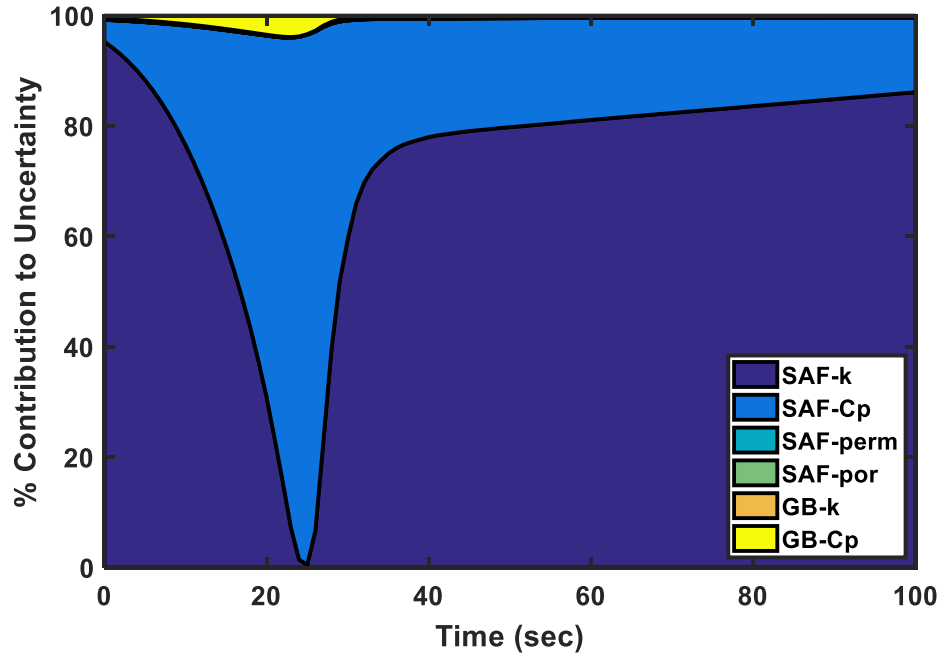
Figure 36: Run 2822 TC5 Uncertainty Analysis

The same method from Test Case 0 and Test Case 1 is used to determine if the number of Monte Carlo runs performed here is adequate. Like before, the objective of the method is to show approximate convergence for peak temperature distributions for thermocouples analyzed in the uncertainty analysis. Figure 37 shows convergence of the TC3, TC4, TC5 peak temperature distribution standard deviations after 2000 Monte Carlo runs, which gives confidence that all three distributions cease to change and have been adequately captured. This lends confidence in the uncertainty analyses shown in Figure 34, Figure 35, and Figure 36 while ensuring that an appropriate number of Monte Carlo runs was performed.
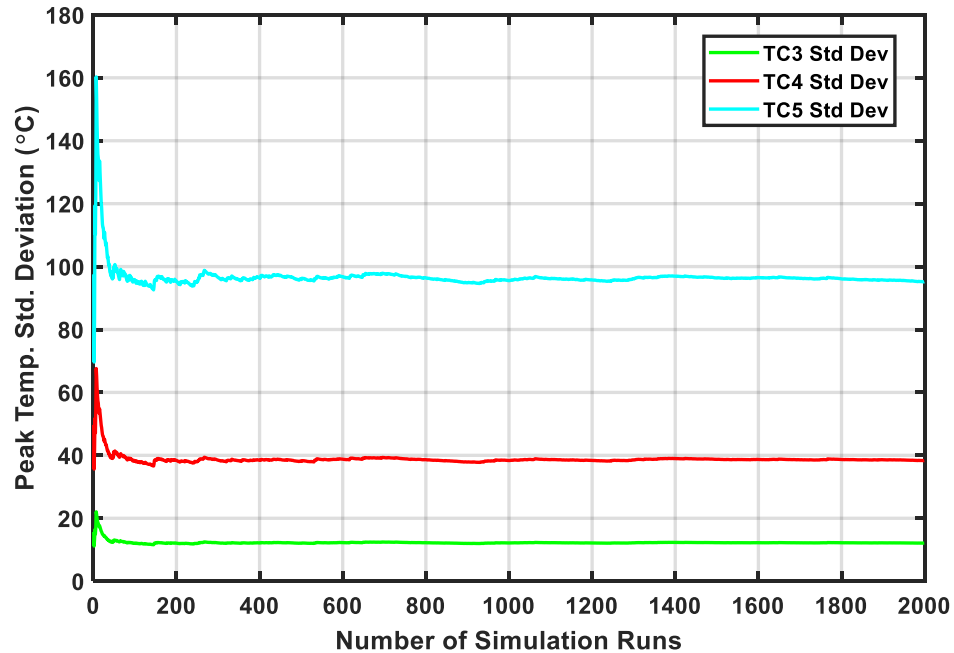
Figure 37: Run 2822 Peak Temperature Distribution Standard Deviation Convergence for TC3, TC4, and TC5

Figure 34 and Figure 35 both show only two scale factors that drive TC3 and TC4 prediction response corresponding to Saffil thermal conductivity and Saffil specific heat. For both TC3 and TC4, thermal conductivity accounts for approximately 78% of prediction uncertainty, followed by approximately 20% from specific heat. Here, it is expected that both thermal conductivity and specific heat drive the response because these two parameters define heat conduction, which is the main mode of heat transfer through insulator layers.

Figure 36 shows three scale factors that drive TC5 prediction response, including Saffil thermal conductivity, Saffil specific heat, and Kapton specific heat. For TC5, thermal conductivity accounts for approximately 80% of prediction uncertainty and specific heat accounts for the remaining 20% for the majority of the time domain. The only exception occurs at approximately 25 seconds when the Saffil thermal conductivity contribution drops sharply to be replaced by approximately 95% Saffil specific heat uncertainty and 5% Kapton specific heat uncertainty. The main reason there is a different behavior in TC5 is

67

because the top-side of the thermocouple is touching the last layer of Saffil while the bottom-side of the thermocouple is touching the gas barrier layer. At approximately 25 seconds, the TC5 bondline temperature prediction begins to rise from zero, causing a momentary dip in thermal conductivity contribution to uncertainty, which stems from thermal response model conduction. The next section investigates the linear dependency of the remaining six scale factors using sensitivity analysis.

2.6.3 Sensitivity Analysis

A sensitivity analysis was performed for the six scale factors listed in Table 5. Scale factors were perturbed ±1% and temperature predictions were obtained for both perturbations. The central difference was taken between perturbed temperature predictions using Equation 5. The resulting temperature differences (dT) are shown for all six scale factors at TC3, TC4, and TC5 locations in Figure 38, Figure 39, and Figure 40.
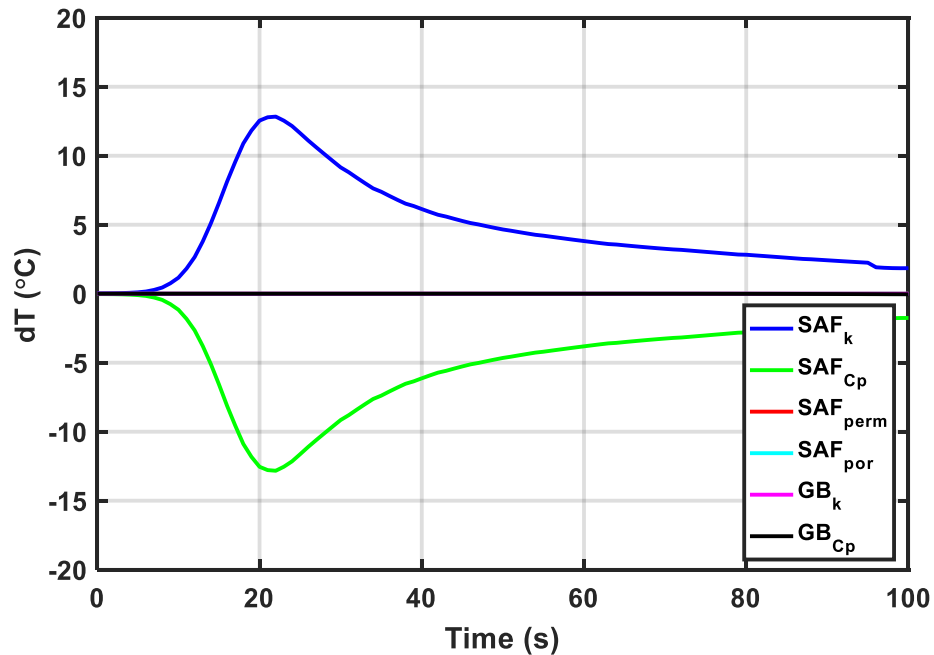
Figure 38: Run 2822 TC3 Sensitivity Analysis

68
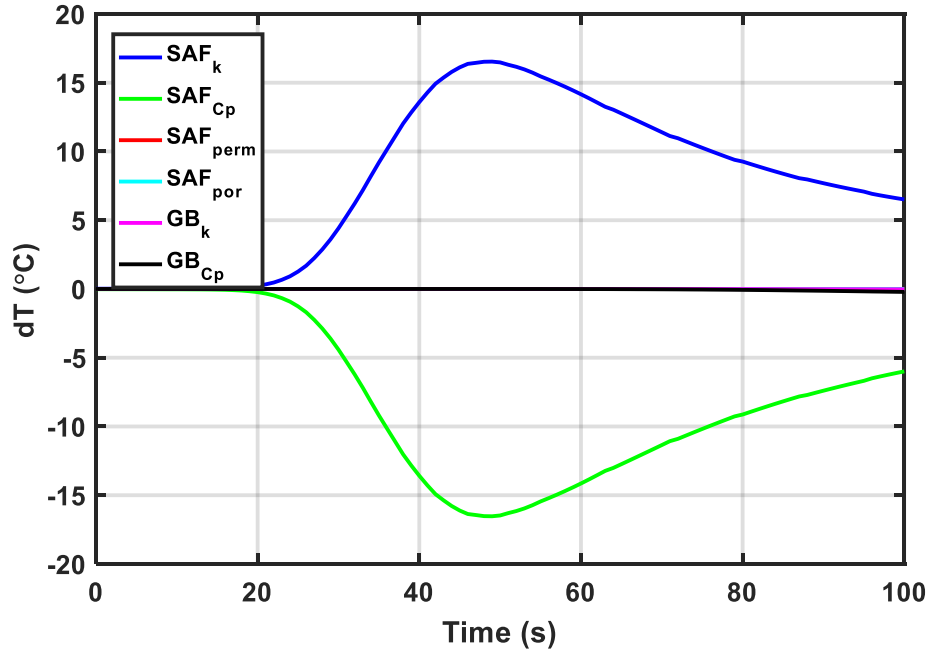
Figure 39: Run 2822 TC4 Sensitivity Analysis
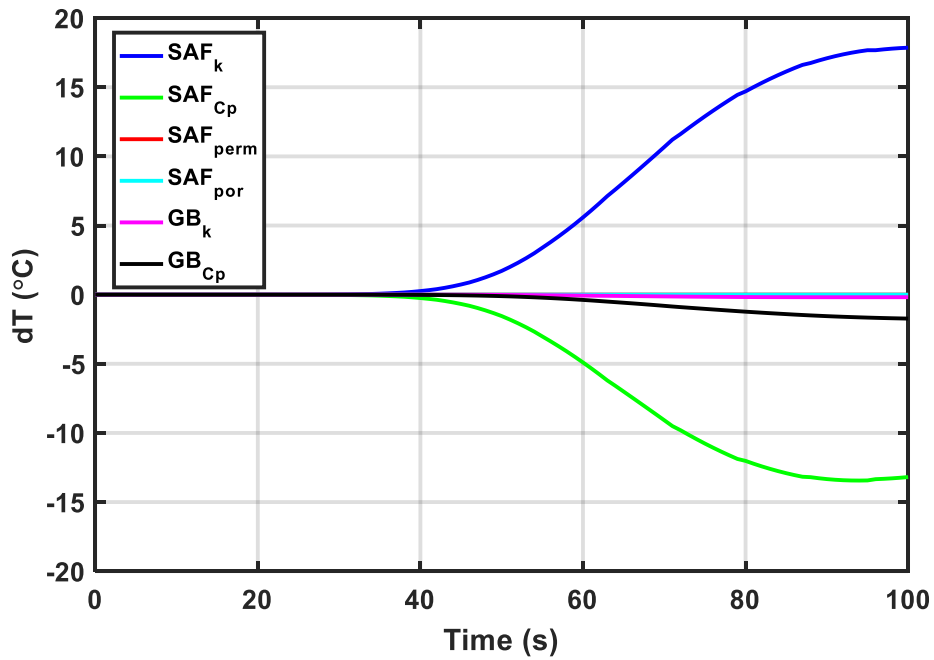
Figure 40: Run 2822 TC5 Sensitivity Analysis

All three figures illustrate the temperature difference from perturbed temperature predictions for each scale factor as a function of time. After examining the figures, one can

see that Saffil thermal conductivity and specific heat scale factors have a negative correlation close to 100% for all thermocouple locations. TC3 and TC4 have negligible contributions from other scale factors, but the next largest contributor at the TC5 location is the Kapton gas barrier specific heat scale factor. Table 6 shows the relative linear dependencies between scale factors in the form of a correlation table. While correlation tables were calculated for each TC independently, this table has averaged results from TC3, TC4, and TC5 together for simplicity.

Table 6: Run 2822 Sensitivity Analysis Averaged Correlation Coefficients for TC3, TC4, and TC5

TC3-5 Avg	SAF k	SAF Cp	SAF Perm	SAF Por	GB k	GB Cp
SAF-k	1					
SAF-Cp	-0.9993	1				
SAF-Perm	-0.7112	0.7198	1			
SAF-Por	-0.9617	0.9619	0.7203	1		
GB-k	-0.2151	0.2064	-0.0076	0.1720	1	
GB-Cp	-0.2127	0.2003	-0.0337	0.1650	0.9933	1

It is advantageous to use scale factors that were large contributors in the uncertainty analysis but not linearly dependent. Although Saffil thermal conductivity and Saffil specific heat scale factors were the largest contributors to uncertainty, they are nearly 100% correlated. As a result, one of these parameters must be neglected and replaced. Because the Saffil thermal conductivity scale factor contributed approximately 80% to uncertainty for TC3, TC4, and TC 5, it will move forward to inverse analysis. The Saffil specific heat scale factor will be neglected and replaced by a less correlated scale factor. According to Table 6, the parameter that is least correlated with the Saffil thermal conductivity scale factor is the Kapton gas barrier specific heat scale factor. As a result, both Saffil thermal conductivity and Kapton specific heat scale factors will be considered in the inverse analysis.

2.6.4 Inverse Analysis

For Test Case 2, the analyst used information from uncertainty and sensitivity analyses to select two scale factors to include in inverse analysis. The selected thermal-material property scale factors include Saffil thermal conductivity and Kapton specific heat. The Saffil thermal conductivity scale factor was selected using uncertainty analysis results that showed it contributes approximately 80% to thermal response model prediction uncertainty for TC3, TC4, and TC5. The Kapton gas-barrier scale factor was selected using sensitivity analysis results that showed it was the least correlated parameter to thermal conductivity. Using these two scale factors together for inverse analysis ensure that the methodology will have a large effect on thermal response model predictions and will not experience convergence instability or issues with solution uniqueness.
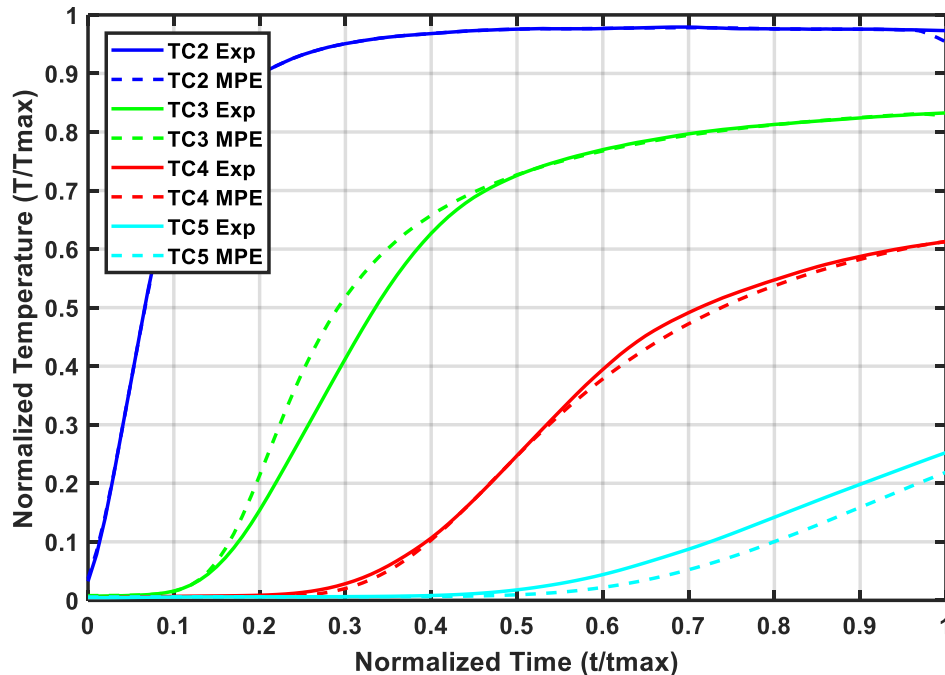
Figure 41: Run 2822 Inverse Analysis for Error-Minimized TC3, TC4, and TC5 Predictions

Inverse multi-parameter estimation was performed on the Layup 2 thermal response model for Test Case 2 using Equations 6 – 14 described earlier. The objective of this

71

procedure was to minimize error between arc-jet thermocouple temperature measurements and thermal response model temperature predictions. Iterations were performed until the stopping criteria was met specified in Equations 15 – 16. After the procedure was completed, the final scale factor values for Saffil thermal conductivity and Kapton specific heat were 0.882 and 0.925, respectively. Using these scale factors, the improved thermal response model temperature predictions are shown in Figure 41.

After comparing these improved predictions to nominal predictions in Figure 32, the reader will notice an interesting result. Nominal predictions over-predicted TC3 and TC4 significantly, but were fairly close to TC5. The sum of squared errors (SSE) objective function that is reduced during inverse analysis considers errors from each thermocouple equally. In order to reduce TC3, TC4, and TC5 combined SSE value, the Saffil thermal conductivity scale factor was lowered from 1 to 0.882. While this allowed for a 33.64% reduction in RMSE and better matches for TC3 and TC4 predictions, it produced a worse match for TC5.

There are a few reasons for this. First, the thermal-material properties for Saffil paper are strongly dependent on each production batch. The thermal conductivity for Saffil paper was measured approximately a decade ago, but since then, the Saffil production recipe has changed slightly. Changes in material production warrant re-measuring of thermal-material properties. The extended inverse parameter estimation methodology was able to account for a significant amount of error due to outdated thermal-material properties. Obtaining updated material properties would eliminate more sources of error likely leading to even better temperature prediction improvement.
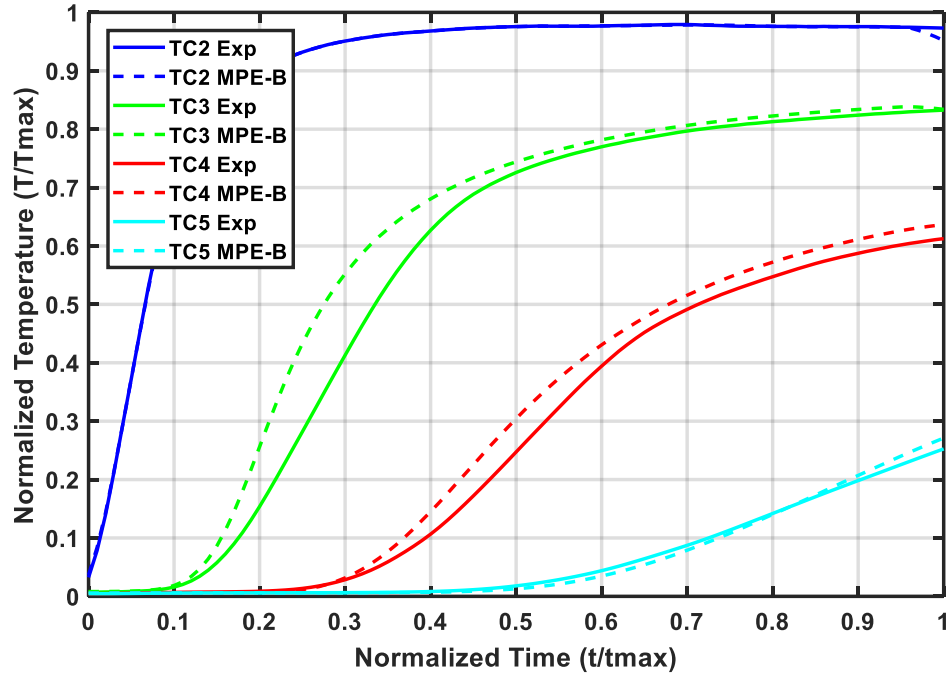
Figure 42: Run 2822 Inverse Analysis for Error-Minimized TC5 Prediction Only

Second, multiplicative scale factors essentially move all temperature prediction curves up or down by the same proportion. For example, Test Case 1 showed significant improvement for both temperature predictions by increasing the KFA5 thermal conductivity scale factor. For Test Case 2, the nominal analysis showed that TC3 and TC4 overpredict by approximately the same proportion, but TC5 did not overpredict measurements. In this situation, adjusting Saffil thermal conductivity to match the TC5 prediction leads to a much larger average RMSE value due to significant inaccuracies in TC3 and TC4. For comparison, Figure 42 shows the resulting predictions if one was only matching the TC5 prediction, referred to as Multi-Parameter Estimation of the Bondline (MPE-Bond). Table 7 shows the average RMSE values for nominal predictions, MPE-Bond predictions, and MPE predictions shown in Figure 41.

Table 7: Run 2822 Comparison of Root Mean Square Error (RMSE) of TC3, TC4 and TC5

Prediction	TC3 (°C)	TC4 (°C)	TC5 (°C)	Avg. (°C)	Avg. % Improved
Nominal	94.99	53.88	17.69	63.874	NA
MPE - Bond	89.68	43.99	10.28	57.98	9.23%
MPE	61.75	14.48	36.98	42.39	33.64%

Obtaining a lower estimate for Saffil thermal conductivity and a slightly lower estimate for Kapton specific heat reduced MPE temperature prediction error by approximately 33.64%. In this case, the improvements in TC3 and TC4 predictions far outweigh the resulting TC5 prediction that is slightly higher. The methodology can also be used to match only the TC5 bondline temperature as shown in Test Case 0, but it only reduces MPE-Bond prediction error by approximately 9.23%. In this case, the TC5 bondline prediction is the lowest, but at the cost of obtaining significantly worse predictions for TC3 and TC4.

To conclude, this study showed that the improved MPE predictions shown in Figure 41 are a significant improvement, and the corresponding thermal-material property adjustments will be carried forward into the final FTPS Dual-Insulator Design Methodology demonstration thermal response model.

2.7 Summary

Multiple FTPS layups were arc-jet tested in the Boeing LCAT facility to characterize thermal-material performance for future HIAD applications. A physics-based thermal response model was created using COMSOL in order to accurately predict measured thermocouple temperatures at multiple depths. After noticing a large modeling discrepancy with initial predictions, an extended inverse multi-parameter estimation methodology was implemented to reduce temperature prediction error by estimating the significant thermophysical properties embedded in the COMSOL model. Measurement uncertainties for thermocouples improved by this methodology were shown to be extremely small. Nominal, uncertainty, and sensitivity analyses provided valuable insight about solution uniqueness and stability, and were used to improve the thermophysical parameter

estimation process. The boundary condition of the thermal response model was driven by the thermocouple between the outer fabric and insulation regions to reduce model discrepancy. Using this TC driver approach, the LM method was implemented during inverse analysis over a nominally selected range to reduce prediction errors for thermocouples of interest.

The extended inverse multi-parameter estimation methodology was demonstrated on three test cases (Test Case 0, Test Case 1, and Test Case 2) corresponding to thermal response models of Layup 0, Layup 1, and Layup 2, respectively. Test Case 0 was a straightforward proof-of-concept that successfully improved the bondline thermocouple prediction for Layup 0 using two parameters from the Pyrogel 3350 thermal-material property scale factors. Test Case 1 successfully improved multiple thermocouple temperature predictions by updating KFA5 insulation scale factors for thermal conductivity and porosity. Finally, Test Case 2 improved multiple thermocouple temperature predictions by updating scale factors representing Saffil insulation thermal conductivity and the Kapton gas barrier specific heat.

These results were achieved by employing the TC driver approach and treating measured thermocouple temperature profiles from arc-jet experiments as "truth". Because measurement uncertainty was shown to be extremely small for analyzed thermocouples, the effects of these uncertainties on parameter estimation results are negligible. A full-scale FTPS requires stitching at certain locations to hold the heatshield materials together during flight. The act of stitching FTPS layers together increases compression that could cause slight variations in temperature measurements between layers. The same extended inverse multi-parameter estimation methodology presented here can be used to improve thermal response model predictions for stitched FTPS arc-jet sample experimental measurements.

The extended inverse multi-parameter estimation methodology was used to improve thermal response model temperature predictions for both Test Case 1 and Test Case 2. To improve Test Case 1 thermal response model predictions, KFA5 thermal conductivity and

porosity scale factors were adjusted to be 1.138 and 0.97, respectively. To improve Test Case 2 thermal response model predictions, Saffil thermal conductivity and Kapton specific heat scale factors were adjusted to be 0.882 and 0.925, respectively. These adjusted scale factors values are carried forward into the dual-insulator thermal response model described in Chapter 4.

While all test cases presented in Chapter 2 use two parameters for inverse analysis, this is not a limitation of the approach. If a different application reveals more than two scale factors that are significant contributors to temperature prediction uncertainty without significant linear-dependency, then a greater number of scale factors can be used in inverse analysis. These test cases prove the value of the developed extended inverse multi-parameter estimation methodology and further development to continue extending capabilities.

CHAPTER III

THERMOGRAVIMETRIC ANALYSIS OF FTPS INSULATION

3.1 Introduction

In an effort to achieve better temperature predictions in the thermal response model, a Thermogravimetric Analysis (TGA) test campaign was performed on virgin samples of two FTPS insulators, composed of carbon felt and aerogel felt, to characterize decomposition by obtaining its activation energy. Experiments were performed in a zero-moisture air and zero-moisture helium environment using Standard TGA and Modulated TGA methods with a TA Instruments Q5000IR experimental apparatus.

TGA is an established experimental procedure used to characterize the decomposition behavior of a material as a function of temperature and time. The primary objective of a TGA test campaign is to gain a deeper understanding of a material's decomposition in a controlled environment. In this case, determining the activation energy of FTPS insulation with TGA is used to obtain more accurate temperature predictions within the FTPS thermal response model. The candidate insulator's activation energy can be described as the minimum amount of thermal energy required for the decomposition process to occur. In this investigation, the activation energy of decomposing FTPS insulators is determined using two different TGA methods, the Standard TGA test method (Ozawa-Flynn-Wall) and a recently-developed Modulated TGA test method [84].

Additionally, the TGA test campaigns contain an embedded material testing methodology that approximates the probability distribution of activation energy. These distributions provide the thermal response model with experimentally-determined ranges

for activation energy used to investigate decomposition sensitivities in a probabilistic fashion.

3.2 TGA Experimental Determination of Activation Energy

A TGA experiment exposes a material sample to a specified temperature profile, pressure, and surrounding gas composition to measure sample mass loss as a function of temperature or time. In this work, the Arrhenius relation is used to model insulator mass decomposition [85], [86], [87]. The primary objective of the experimental campaign is to identify the activation energy of decomposing FTPS insulators.

3.2.1 Introduction to FTPS Thermal Response Model

Creating a thermal model that accurately predicts temperatures within an FTPS layup requires detailed understanding of the physical processes and thermal-material properties associated with each layer. The first step in developing a thermal response model is verifying that all pertinent physical processes are included and all thermal-material properties have been developed through testing or expert-opinion over the appropriate temperature and pressure range of interest. Next, the model must be validated by comparing recorded arc-jet test temperature data between FTPS layers to corresponding temperature predictions in the thermal response model. Finally, the performance of the thermal model is evaluated based on how closely the temperature predictions as a function of time match the arc-jet temperature data measured at each thermocouple location.

While many different configurations have been arc-jet tested experimentally, two configurations will be investigated in this analysis. Figure 43 below shows a pure KFA5 insulator layup (left) and a pure P2250 insulator layup (right). Each configuration contains two layers of outer fabric material, either COI Ceramics' Nicalon Silicon-Carbide (left) or Nextel BF20 (right). The KFA5 Layup contains two layers of Sigratherm's KFA5 carbon felt while the P2250 Layup contains four layers of Aspen Aerogel's Pyrogel 2250 (P2250). Finally, the KFA5 Layup contains one layer of Kapton gas-barrier material while the P2250 Layup contains one layer of Aluminized Kapton laminated to Kevlar (AKK) gas barrier

material. An additional layer of insulation called LI900 is included as a final layer of insulation only used during arc-jet testing as a safety precaution. Because LI900 is not part of the planned FTPS material that will be flown on HIAD, it is outside the scope of this work.
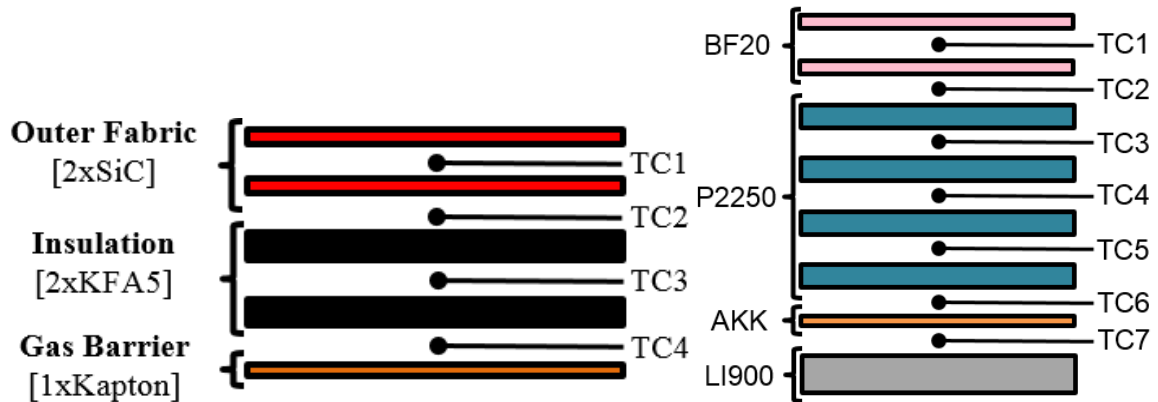
Figure 43: KFA5 Layup [SiC/KFA5/Kapton] (Left) and P2250 Layup [BF20/P2250/AKK] (Right)

During arc-jet testing, thermocouple sensors are placed between FTPS layers to obtain experimental temperature measurements with time at various depths (TC1, TC2, TC3, TC4, TC5, TC6, and TC7 from Figure 43). The COMSOL thermal response model is used to generate corresponding thermocouple temperature vs. time predictions at the same thermocouple depths within the FTPS layup. The goal of the modeling effort is to produce thermocouple predictions within an acceptable agreement to thermocouple measurements. The TC Driver Approach is used to apply boundary conditions to both thermal response models.

3.2.2 Introduction to TGA Experimentation

KFA5 carbon felt and P2250 aerogel felt serve as insulators for a wide variety of commercial applications. Both FTPS insulators have low thermal conductivity, low mass, high flexibility, and can dissipate heat efficiently through decomposition processes. As such, both felt insulators have proven to be viable candidates for the HIAD FTPS.

Previous arc-jet ground-tests have shown that KFA5 samples heated above 300℃ in zero-moisture air begin to experience significant decomposition due to carbon oxidation. Similar tests have shown that, as Pyrogel materials are heated to the region between 375℃ and 600℃, they begin to shrink in size while decomposing and emitting gases as a result of pyrolysis.

3.2.3 General Arrhenius Equation Applied to TGA

The Arrhenius equation, defined in Equation 2, was the chosen FTPS insulator decomposition model used in this investigation [44]. The fundamental form of the Arrhenius equation defines the approximate relationship between the rate constant (k) and the activation energy (E_a) for a material. This expression is a function of the pre-exponential factor (A), the universal gas constant (R), and the temperature (T) of the sample material. In order to fully define the Arrhenius equation for a material, one needs to expose the sample to a controlled thermal event by selecting the gaseous environment composition, pressure, and varied temperature profiles. This environment is achieved by performing a series of careful TGA experiments.

The activation energy can be calculated from prescribed data reduction procedures set forth by the American Society for Testing and Materials (ASTM) according to the type of TGA method. This investigation assumes that both KFA5 carbon felt and P2250 aerogel felt decomposition processes can be accurately modeled using the Arrhenius equation, which allows the experimental determination of resulting activation energies using ASTM prescribed calculation procedures.

Equation 17 relates the degree of conversion, (α), to standard quantities obtained through TGA testing, such as initial sample weight (W_o) and sample weight as a function of time (W_t). Equation 18 shows a general expression for the reaction rate ($\frac{d\alpha}{dt}$), in terms of the rate constant, $k(T)$, and the kinetic expression, $f(\alpha)$. Equation 19 is the familiar Arrhenius equation as a function of temperature. Equation 20 shows that an nth order

kinetic expression was chosen for this study. For simplicity, the reactions discussed in this study are considered first-order reactions, where n = 1. Finally, Equation 21 displays the reaction rate in terms of kinetic parameters.

$$\propto = \frac{W_0 - W_t}{W_0} \tag{17}$$

$$\frac{d\propto}{dt} = k(T)\, f(\propto) \tag{18}$$

$$k(T) = A\, exp\left(-\frac{E_a}{RT}\right) \tag{19}$$

$$f(\propto) = (1-\propto)^n \tag{20}$$

$$\frac{d\propto}{dt} = A\, exp\left(-\frac{E_a}{RT}\right)(1-\propto)^n \tag{21}$$

3.2.4 Standard TGA Method Summary

Decomposition kinetics for the Standard TGA method are modeled using the Ozawa/Flynn/Wall method outlined in the ASTM Standard Test Method E1641-15 [44]. The left portion of Figure 44 shows four sample TGA curves at different heating rates, while the right portion of Figure 44 shows the resulting Arrhenius plot one can create from Standard TGA data. Please refer to the ASTM method [44] for more details about the calculation method.
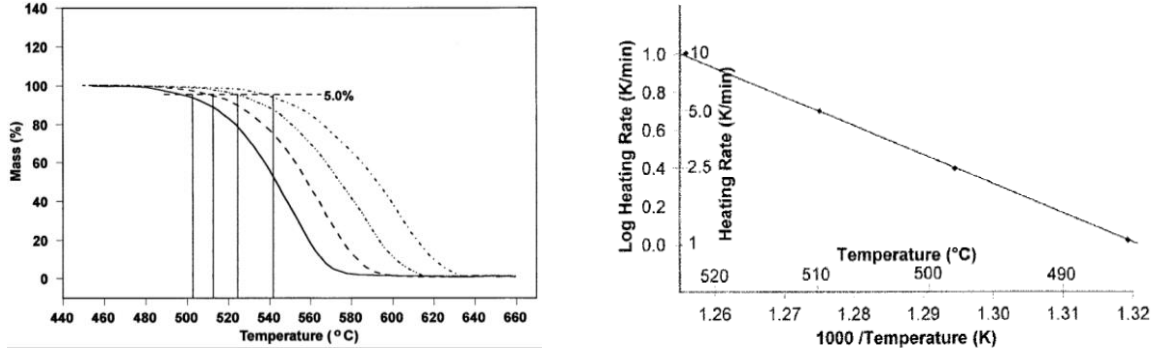
Figure 44: Sample Standard TGA Curves (Left) and Sample Arrhenius Plot (Right) [44]

The slope of the Arrhenius plot is a key quantity used to obtain the activation energy. Equation 22 shows how one can obtain the slope of the Arrhenius plot, referred to as (m). After obtaining this slope, and iterative procedure begins to converge on the activation energy. The Ozawa/Flynn/Wall method outlined in ASTM E1641-16 provides a lookup table to help complete this iteration procedure. The quantities referred to as (a), (b), and (E/RT) are all values listed in this table. The initial guess for activation energy using the (b) parameter comes from the solution of Equation 23. The calculations in Equations 23 and 24 are compared until convergence is achieved. Finally, the converged value for activation energy is used to calculate the pre-exponential factor shown in Equation 25.

$$m = \frac{\Delta(\ln \beta)}{\Delta\left(\frac{1}{T}\right)} \tag{22}$$

$$E_a = -\left(\frac{R}{b}\right)\frac{\Delta(\ln \beta)}{\Delta\left(\frac{1}{T}\right)} \tag{23}$$

$$E_{it} = \frac{E_a}{RT} \tag{24}$$

$$A = \frac{\beta\,R\,\ln(1-\alpha)\,10^a}{E_a} \tag{25}$$

82

3.2.5 Modulated TGA Method Summary

The Modulated TGA method was championed by researchers at TA instruments as a way to obtain the decomposition kinetics of a sample with less experimental effort. This method produces an "…oscillatory response in the rate of weight loss. Deconvolution of this response, using real-time discrete Fourier transformation (DFT), leads to the desired kinetic parameters (E and A)" [88]. Figure 45 shows an example of a modulated temperature profile, represented by the blue sinusoid, oscillating about the average temperature of a constant heating rate temperature profile, represented by the green line.
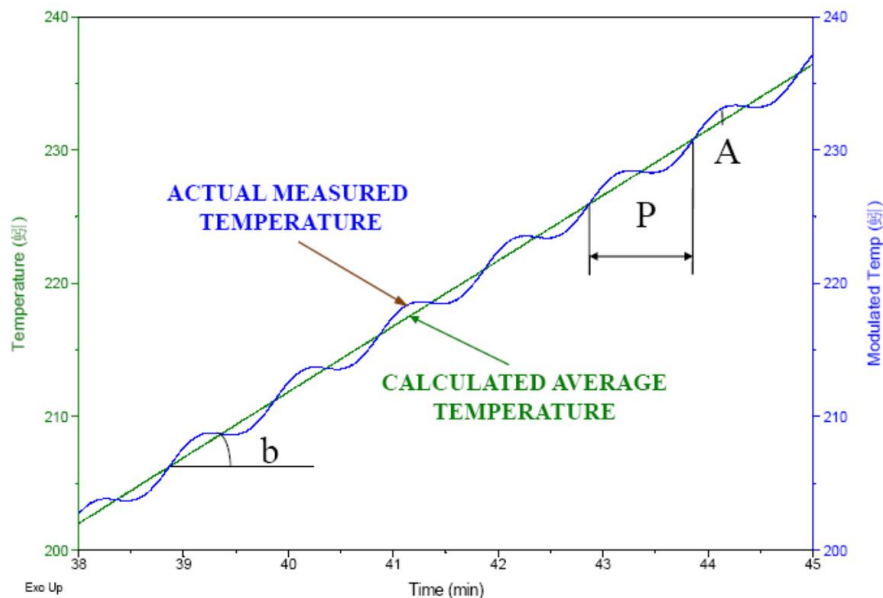
Figure 45: Modulated TGA Sample Signal [89]

ASTM Standard Test Method E2958 – 14 outlines the accepted testing procedure for a Modulated TGA experiment, which has been adhered to closely in the following analysis. Using slightly different expressions, Equations 26 – 28 briefly show how the calculation is performed to obtain the activation energy and the pre-exponential factor of a sample exposed to a single modulated ramp TGA test. In these equations, (T) represents the average temperature, (A_{MP}) represents the temperature half-amplitude, and (L) represents the amplitude of the natural log of the rate of weight change. ASTM E2958-14 specifies

appropriate values for modulated temperature period and amplitude during Modulated TGA to achieve at least five complete oscillations during the decomposition event. Please refer to References [89] and [90]for more information about these equations and related derivations.

$$E_a = \frac{R(T^2 - A_{MP}{}^2)L}{2A_{MP}} \qquad (26)$$

$$\text{where } L = \ln\left(\frac{d\alpha_p/dt}{d\alpha_v/dt}\right) \qquad (27)$$

$$\ln A = \ln\left(\frac{d\alpha}{1-\alpha}\right) + \frac{E_a}{RT} \qquad (28)$$

3.2.6 TGA Experimental Procedures for FTPS Insulation

The following TGA experimental campaign aims to provide many independent determinations of insulator activation energies to further characterize these decomposition processes. Inserting experimentally-derived values for activation energy into the COMSOL TRM is expected to improve correlation of FTPS thermal model temperature predictions to measured temperatures from arc-jet experimental data by providing additional understanding of material properties.

Two different types of TGA tests were performed to obtain the activation energy. The Standard TGA experimental method requires exposing samples to 4 different heating rates to obtain one determination of activation energy. In this study, the analyst chose to subject FTPS insulators to heating rates of 2°C/min, 5°C/min, 8 °C/min, and 10 °C/min. The Modulated TGA experimental method exposes the sample to a sinusoidal variation about a constant heat rate profile as shown in Figure 45. In this investigation, the chosen Modulated TGA experimental parameters included a heating rate of 2°C/min, a modulation period of 200 seconds, and a sinusoidal amplitude of ± 5 °C. Unlike the Standard TGA

method, the Modulated TGA method can obtain one determination of activation energy after only one experiment.

TGA testing was performed on carbon felt samples using a TA Instruments TGA Model Q5000IR, referred to as the TA Q5000IR from here forward. An image of the TA Q5000IR is shown below in Figure 46.
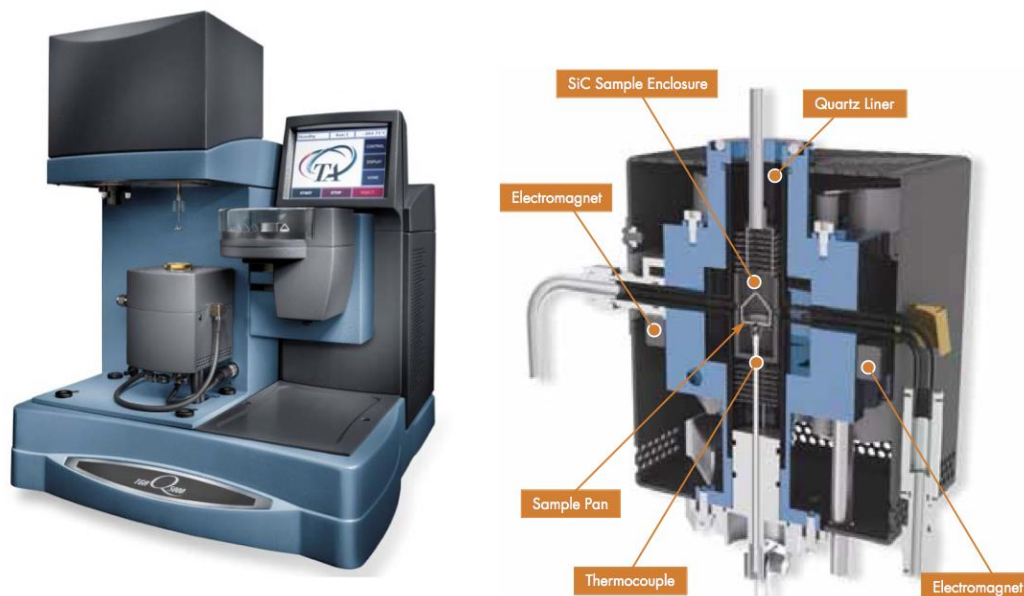
Figure 46: TGA Model TA Q5000IR (Left) and TA Q5000IR Furnace Cross Section (Right) [91]

The TA Q5000IR is a relatively new instrument that has many advanced capabilities. The "IR" refers to infrared furnace heating provided by internal lamps. Using infrared heating allows for high precision of temperature profiles and near instantaneous equilibration to specified temperatures for isothermal testing. In addition to having a high precision balance to measure weight loss as a function of time, the TA Q5000IR also has the ability to run a pre-defined sequence automatically. For each TGA run, the user is able to specify a detailed series of events that is carried out in a prescribed order. Also, the

instrument has the capability to transfer samples automatically using a rotating carousel. These capabilities were utilized and appreciated by the analyst in the following tests. Figure 46 shows a cross section of the furnace itself. It is important to note that the gas flows across the sample in the direction parallel to the ground. This eliminates the need to run a "blank" run to correct for buoyancy as one might have to do for a furnace with a vertical sample gas flow.

Figure 47 provides a detailed account of preparation and loading procedures of KFA5 samples into the TA Q5000IR furnace. A similar process was followed when testing P2250 samples. The order of succession in Figure 47 starts in the upper left corner and continues from left to right, row by row, until the final image in the bottom right corner. Samples of KFA5 and P2250 insulation were tested in the "as-received" felt form rather than powdered form to more accurately capture FTPS in-flight decomposition. Carbon felt or aerogel felt sample was cored directly from a larger disk of felt material from the manufacturer. Using the brass, T-shaped "coring" device, cylindrical cores of samples were sliced out of the larger piece, shown in the top-left corner. Once the samples were cut, they were placed into Alumina pans on the sample carousel and loaded into the TA Q5000IR furnace. Because KFA5 samples were approximately twice as thick as P2250 samples, a deeper alumina crucible was purchased to prevent exposed KFA5 material from being blown over the crucible lip during TGA experiments. Once closed, the furnace is heated to a maximum temperature a specified heating rate, shown in the bottom-right corner. Between rounds of testing, debris was routinely cleaned from the alumina pans through a prescribed bake out procedure in a muffle furnace.

Figure 47: Sample Loading Procedure of KFA5 Samples into TA Q5000IR

The flow rates of gas through the instrument were programmed to send a flow rate of 10 ml/min of Argon to the balance. A flow rate of 25 ml/min of zero-moisture Air was used for KFA5 samples and a flow rate of 25 ml/min of zero-moisture Helium was used for P2250 samples. Each TGA run shown in this study followed identical run sequences. Each run sequence contained two distinct stages: a moisture removal stage and a dynamic stage. The moisture removal stage took approximately 40 minutes, resulting in a dry sample and a dry environment inside the furnace at a temperature of approximately $30\,^\circ$C. The dynamic stage, followed directly after, consisted of a linear ramp to a specified final temperature for Standard TGA or sinusoidal ramp to a specified final temperature for Modulated TGA.

3.2.7 Results - Activation Energy for FTPS Insulation with TGA

After calibrating the TGA instrument to run at a heating rates of 2, 5, 8, and $10\,^\circ$C/min, a TGA experimental campaign using Standard and Modulated TGA was completed for both FTPS insulators. The following Figure 48 - Figure 51 show sample weight-loss curves and Arrhenius plots for one set of KFA5 carbon felt samples and one set of P2250 aerogel felt. Limited portions of the entire data set are shown here for brevity.

87
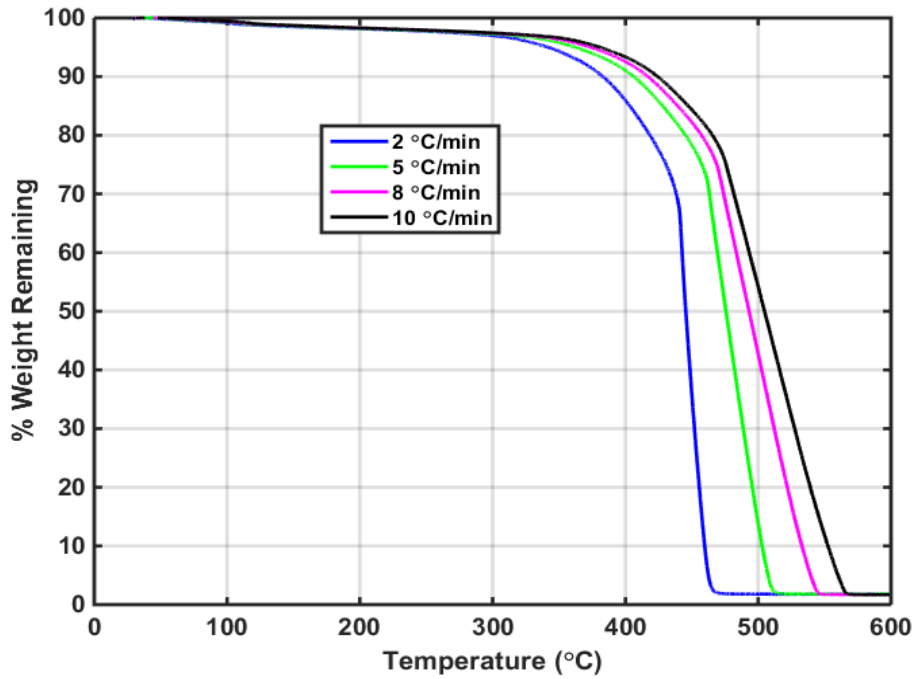
Figure 48: Sample Set of 4 Standard TGA Tests of KFA5 in zero-moisture Air at 2, 5, 8, and 10°C/min
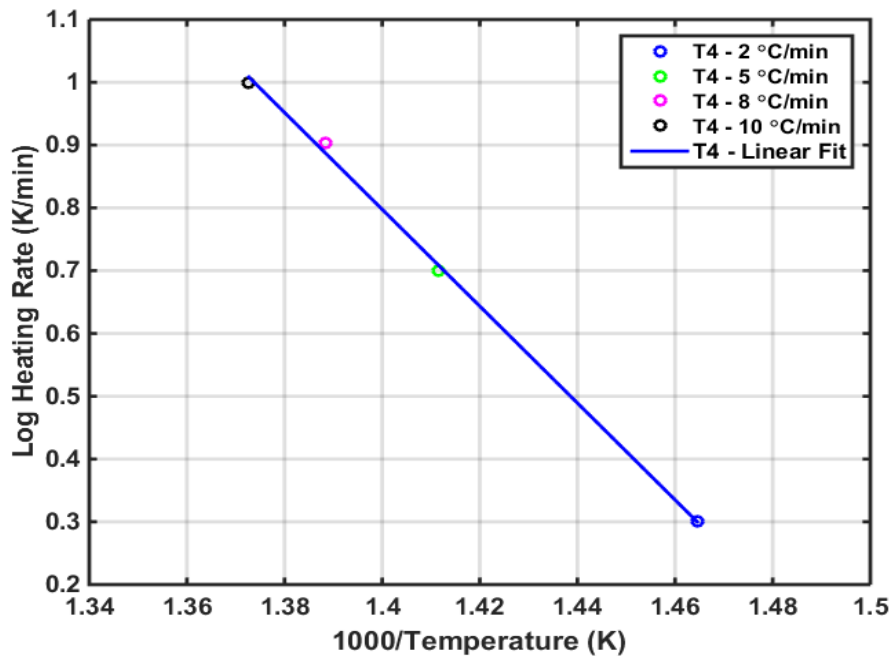
Figure 49: Sample Arrhenius Plot for a Set of 4 Standard TGA Tests of KFA5 in zero-moisture Air at 2, 5, 8, and 10°C/min with a Linear Fit
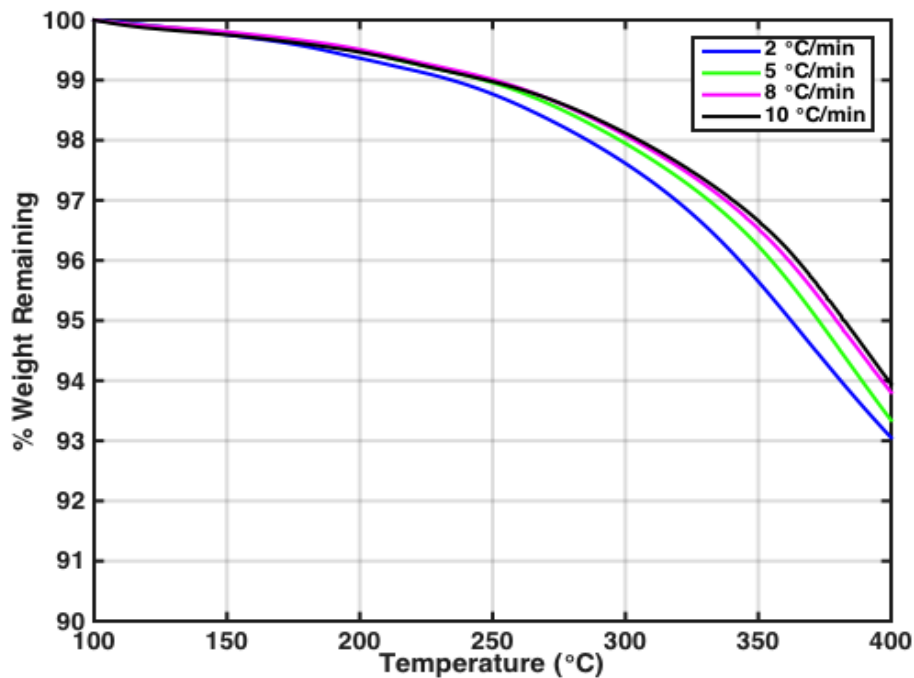
Figure 50: Sample Set of 4 Standard TGA Tests of Pyrogel 2250 in Helium at 2, 5, 8, and 10°C/min
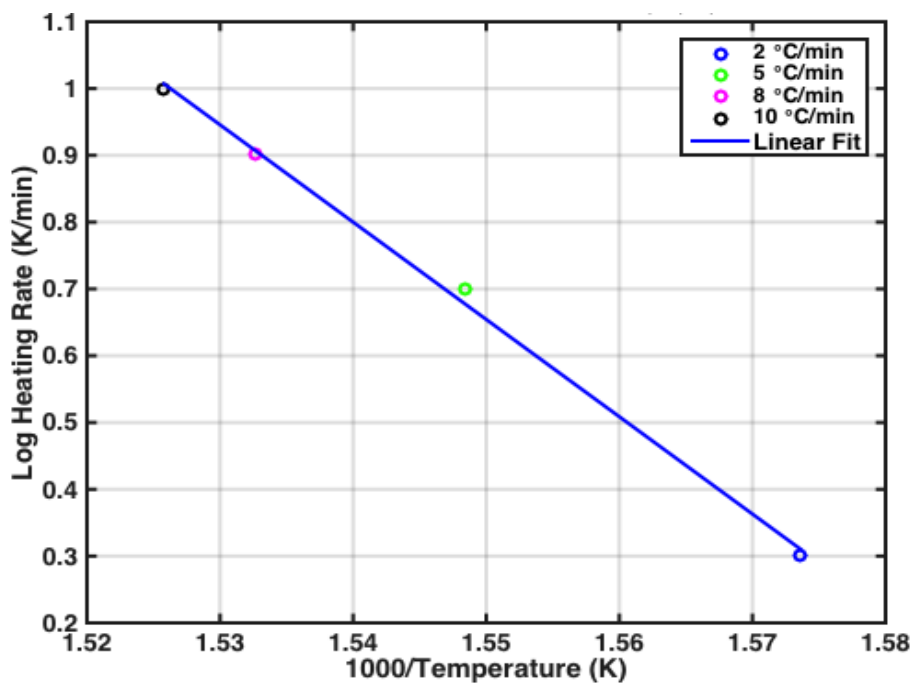
Figure 51: Sample Arrhenius Plot for a Set of 4 Standard TGA Tests of Pyrogel 2250 in Helium at 2, 5, 8, and 10° C/min with a Linear Fit

Figure 48 and Figure 50 show the weight loss profiles for families of 4 Standard TGA tests at heating rates of 2, 5, 8, and $10\,^\circ$C/min as a function of temperature for both FTPS insulators. While each experiment was performed up to a chosen final temperature, this investigation focuses on finding the activation energy for the region of constant conversion of the decomposition event, which was determined to occur at a weight loss remaining percentage of 83% and a temperature of approximately $408\,^\circ$C for KFA5 carbon felt samples. Appendix A provides more information about how 83% weight loss remaining was selected. For P2250 aerogel felt samples, the region of constant conversion for the first decomposition event was determined to occur at a weight loss remaining percentage of 95% and a temperature of approximately $375\,^\circ$C. After selecting the region of constant conversion for each FTPS insulator, one can create corresponding Arrhenius plots to calculate activation energies, shown in Figure 49 and Figure 51. The linear fit is fairly accurate in both cases, showing that the Arrhenius relation can accurately capture decomposition for these materials. First order reaction behavior was assumed for the both decomposition events.

Figure 52 and Figure 53 show typical modulated TGA sinusoidal temperature profiles and weight loss curves for each FTPS insulator. The green curves represent insulator weight-loss as a function of time while the magenta sinusoids show the modulated temperature profiles oscillating about a constant heating rate of $2\,^\circ$C/min.
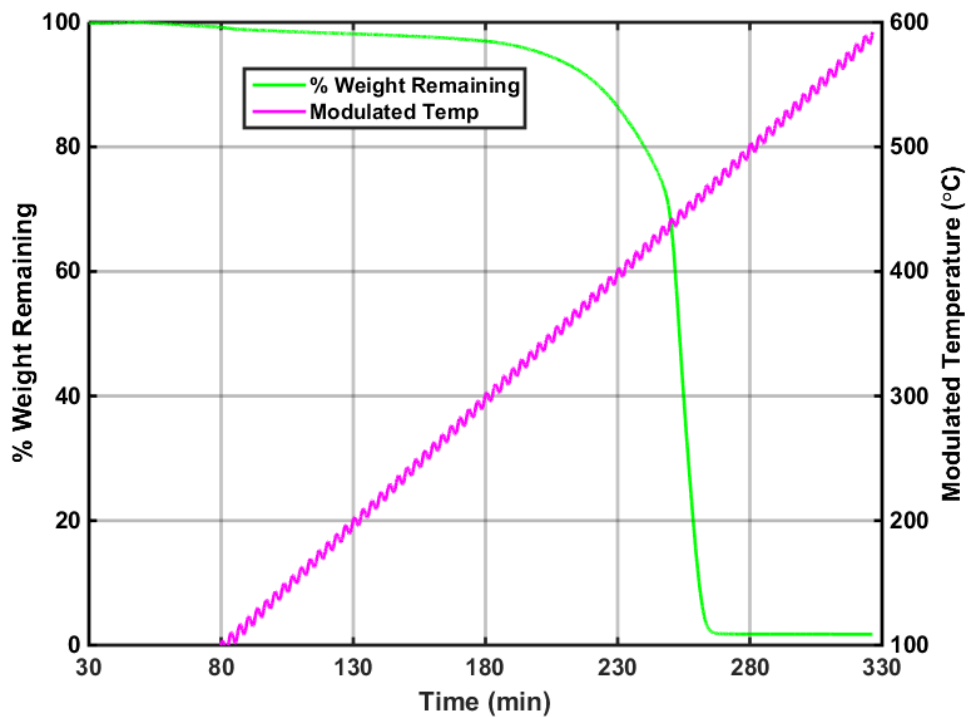
Figure 52: Sample Modulated TGA Test of KFA5 in Zero-Moisture Air at 2°C/min
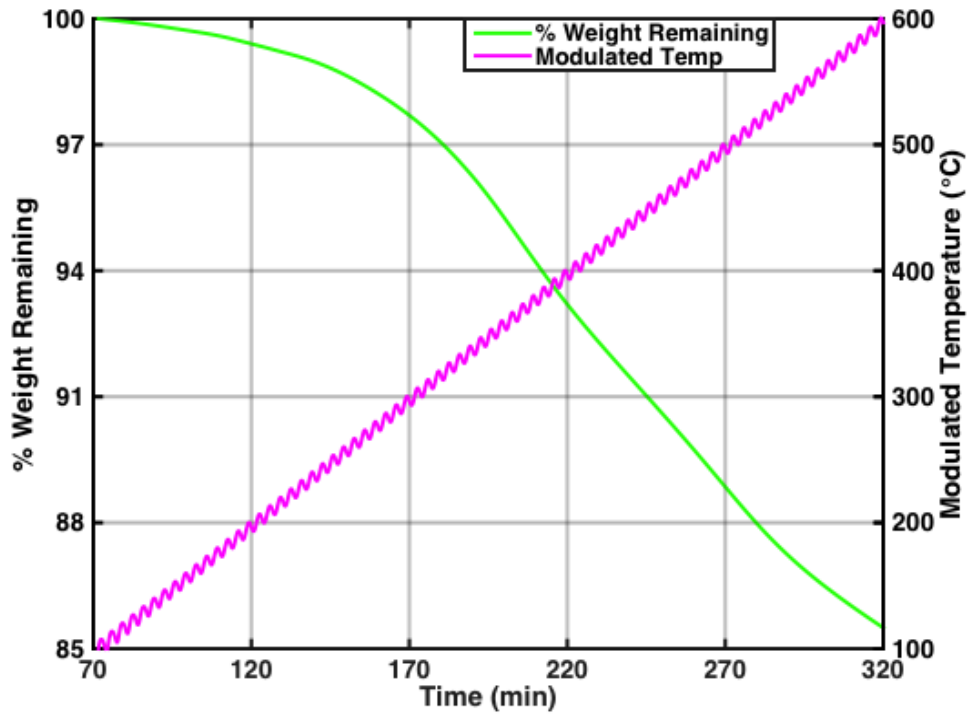
Figure 53: Sample Modulated TGA Test of Pyrogel 2250 in Helium at 2°C/min

Previously mentioned calculation procedures set forth by ASTM were followed to calculate activation energy from Standard and Modulated TGA experiments. The following section describes a novel methodology presented in this dissertation used to approximate the activation energy probability distributions of KFA5 carbon felt and P2250 aerogel felt insulators for both TGA methods.

3.3 Approximation of Activation Energy Probability Distribution

Due to scarcity of experimental resources, TGA testing is performed sparingly. For example, to find the activation energy of one material, a traditional experimentalist may perform one repeated test (2 tests) at three different heating rates (6 tests total) before estimating its activation energy. If one seeks to obtain the associated activation energy probability distribution to characterize uncertainty, this challenge of limited resources is even more constraining.

A key finding showed that many materials are assumed to have normally distributed activation energies, as described by the Distributed Activation Energy Model (DAEM) [92], [93], [94]. If the analyst makes this common assumption, he may approximate the activation energy probability with an experimental t-distribution. The more experiments that are performed, the closer the t-distribution approaches a normal distribution. The present work defines a methodology to obtain an approximate probability distribution of activation energy by completing repeated tests, providing a straightforward method to characterize its uncertainty. This method is demonstrated here as a proof-of-concept can be extended to other material properties as well.

3.3.1 Activation Energy Probability Distribution Approximation Methodology

Thermophysical properties can be measured with confidence using traditional experimental methods, but characterization of property uncertainties is particularly challenging. The following methodology uses experimental repetition to establish the $\pm 3\sigma$

uncertainty bounds for a specific material property to enable future probabilistic analysis methods.

In this investigation, the probability distribution of activation energy is approximated using two types of TGA testing. The confidence level describes the percentage of a distribution that fits between a specified confidence interval. As the number of total TGA experiments increases (including repetitions), the percentage of the t-distribution within the ± 3σ uncertainty bounds, or confidence level, increases. The left portion of Figure 54 compares a normal distribution to two t-distributions with varying degrees of freedom. Degrees of Freedom (DoF) were varied between 1 and 10 for t-distributions to find the minimum degrees of freedom required to exceed the 95% confidence level between ± 3σ uncertainty bounds. As shown in the right portion of Figure 54, a minimum of 4 DoF's, or 5 experiments, are required to exceed a confidence level of 95%.
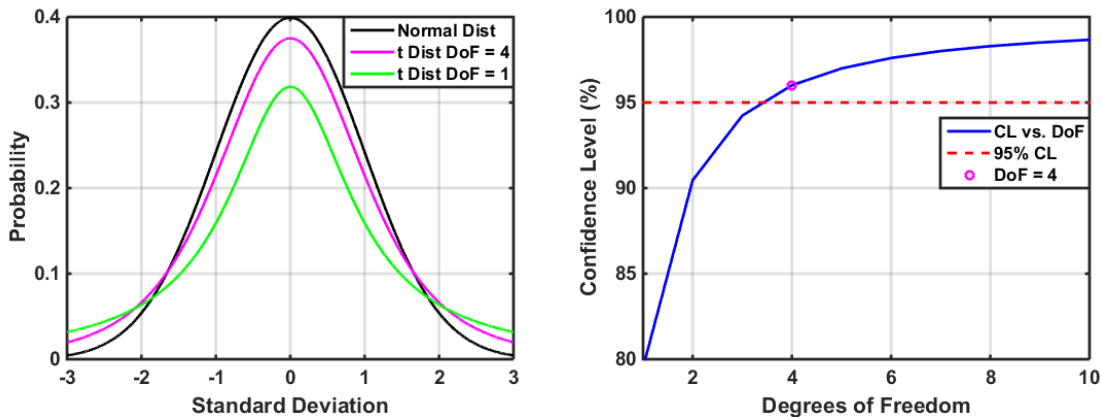
Figure 54: Sample t-Distributions vs. Normal Distribution (Left) and Degrees of Freedom Required for a t-Distribution to Exceed a Confidence Level of 95% Between ± 3σ (Right)

These results suggest two important conclusions: a t-distribution with a 95% confidence level between ± 3σ closely approximates a normal distribution and 5 experiments are required at each TGA testing condition to obtain this t-distribution for activation energy. After completing 5 TGA tests at each condition for Standard and Modulated TGA, 5

independent determinations of activation energy may be performed for each method. The sample mean and sample variance can then be calculated.

3.3.2 Results - Approximate Activation Energy Probability Distributions

After completing five sets of Standard TGA experiments at heating rates of 2, 5, 8, and 10°C/min, the analyst could complete five Modulated TGA experiments at a heating rate of 2°C/min. Figure 55 shows weight loss curves as a function of temperature, along with their corresponding activation energy signals, for the set of five Modulated TGA experiments performed on KFA5 carbon felt samples zero-moisture air. Figure 56 shows only weight loss curves for the set of five Modulated TGA experiments performed on P2250 aerogel felt samples in Helium. Resulting activation energies were obtained using the calculations described in the previous section assuming first order reaction behavior at the region of constant conversion of each decomposition event.
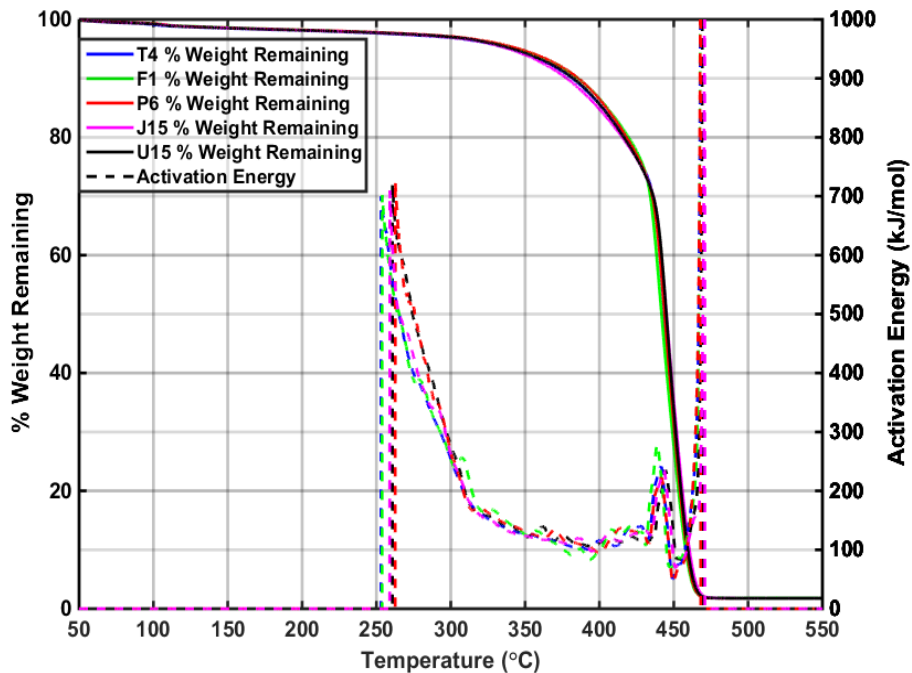
Figure 55: 5 Sample Modulated TGA Tests of KFA5 in zero-moisture Air at 2°C/min
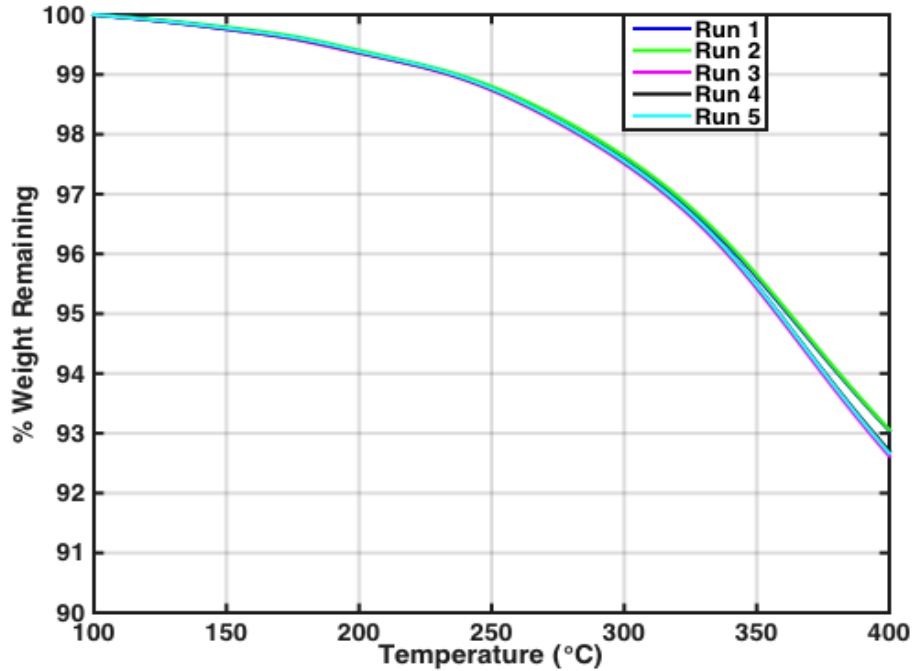
Figure 56: 5 Sample Modulated TGA Tests of Pyrogel 2250 in Helium at 2°C/min

After reducing all experimental data and following the presented methodology, t-distributions for activation energy could be obtained for both KFA5 carbon felt and P2250 aerogel felt for both Standard and Modulated TGA methods. Figure 57 shows the approximated activation energy t-distributions for KFA5 carbon felt with corresponding ± 3σ standard deviation bounds for each t-distribution. Figure 58 shows the approximated activation energy t-distributions for P2250 aerogel felt with corresponding ± 3σ standard deviation bounds. Distributions are shown on the same plot for scale with blue curves representing the Standard TGA method and green curves representing the Modulated TGA method.
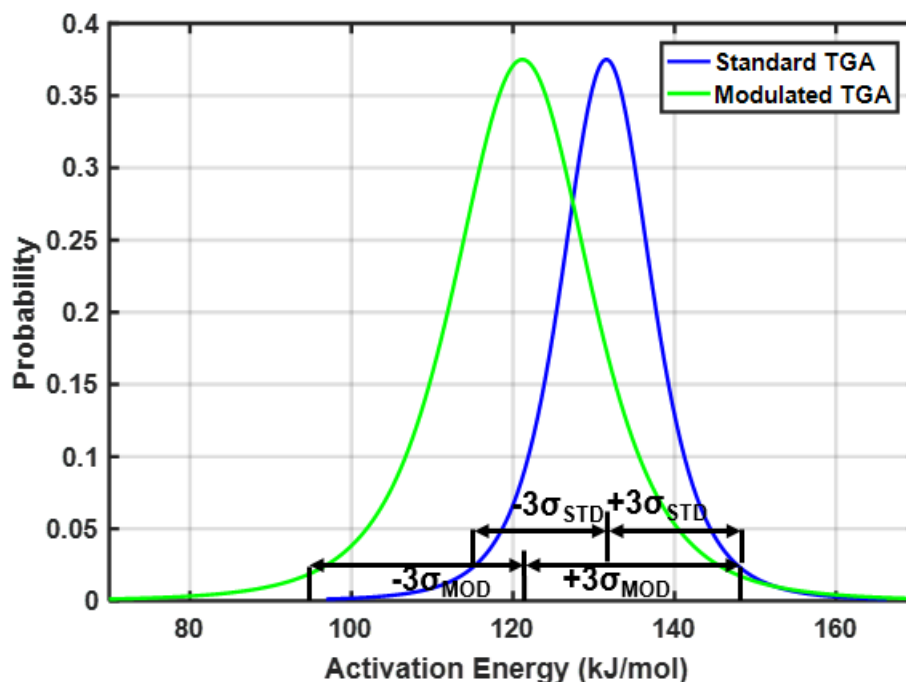
Figure 57: Location of ± 3σ Uncertainty Bounds on KFA5 Activation Energy t-
Distributions Obtained from Standard and Modulated TGA Testing

For KFA5 carbon felt, the mean and standard deviation of the Standard TGA t-distribution is approximately 131.56 kJ/mol and 5.79 kJ/mol, respectively. The mean and standard deviation of the Modulated TGA t-distribution is approximately 121.16 kJ/mol and 8.66 kJ/mol, respectively.

The mean of activation energy for both distributions are fairly close together and show excellent agreement. The mean obtained from the Standard TGA method is slightly higher by approximately 10 kJ/mol, which may be contributed to the calculation procedure averaging results over 4 heating rates (2, 5, 8, and 10°C/min) that are greater than or equal to the heating rate used for Modulated TGA (2°C/min).

One can also see that the standard deviation of activation energy is slightly higher for Modulated TGA than that of Standard TGA. Accepted procedure for Modulated TGA instructs the analyst to establish the activation energy in the region of constant conversion, which should be apparent as a "valley" in the activation energy signal, signifying the point where the decomposition event is proceeding at a constant rate. Figure 55 shows the stable

"valley" for the activation energy signals obtained from Modulated TGA occurs just above 400° C. This finding shows strong agreement with the region of constant conversion obtained from Standard TGA at 408° C, and therefore, strong agreement between both methods. It is important to note that the weight loss curves in Figure 55 begin to span a wider range as each sample enters the region of constant conversion, which is likely due to manufacturing variation between samples. This wider range is passed on to the corresponding activation energy signals, which is the main reason why the standard deviation of Modulated TGA exceeds that of Standard TGA.
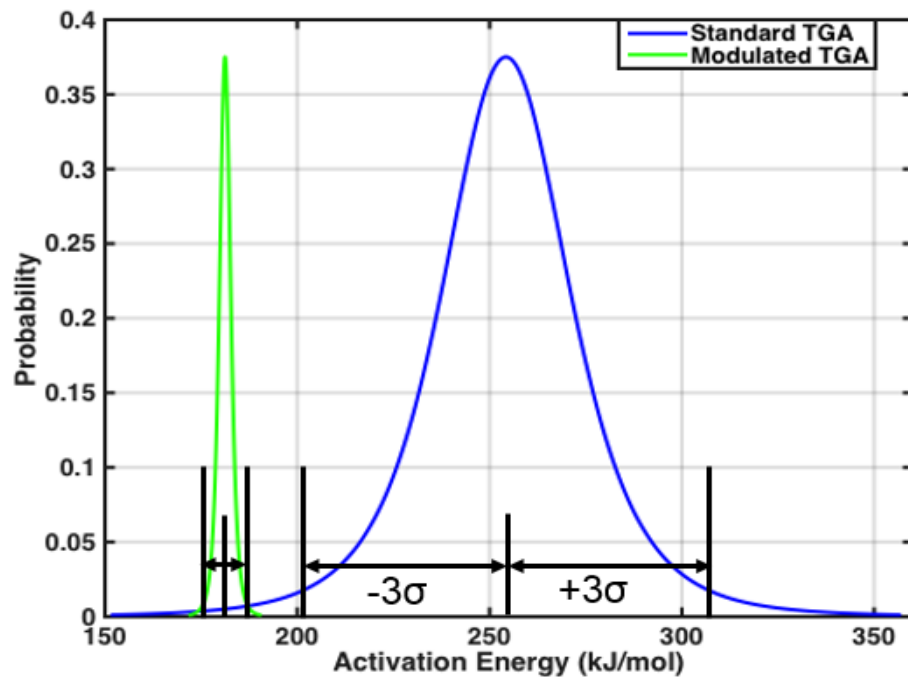
Figure 58: Location of ± 3σ Uncertainty Bounds on t-Distributions for Activation Energy for Pyrogel 2250 Obtained from Standard and Modulated TGA Testing

For P2250 aerogel felt, the mean and standard deviation of the Standard TGA t-distribution is approximately 257 kJ/mol and 17 kJ/mol, respectively. The mean and standard deviation of the Modulated TGA t-distribution is approximately 181 kJ/mol and 1.5 kJ/mol, respectively. The mean of activation energy between the two methods are fairly similar, but much further apart than corresponding KFA5 distributions.

It is important to observe that P2250 Standard TGA experiments drew samples randomly from only a few material disks while the KFA5 Standard TGA experiments completed one activation energy determination per disk. Despite several attempts, the analyst was not able to obtain additional batches of material, so experimental results are limited to one batch for KFA5 disks and one batch for P2250 disks. Additionally, P2250 Modulated TGA experiments drew all samples from one disk while KFA5 Modulated TGA experiments again drew one sample per disk. This sampling method is most likely what causes the means of Standard and Modulated TGA distributions to be farther apart, and also what causes the standard deviation of the Modulated TGA distribution to be much tighter than the spread of the Standard TGA distribution. This is an interesting result that suggests the sampling method is crucial and warrants future investigation.

3.4 FTPS Thermal Response Modeling with Insulator Decomposition

Generally, material property testing is performed over discrete temperature and pressure ranges to improve the validity of the thermal response model. In limited instances, arc-jet test conditions can potentially produce temperatures that exceed the bounds of collected thermophysical data, forcing the analyst to extrapolate to provide continuity. In other cases, experimentally determined thermophysical property data is not available, and properties must be estimated. Before this investigation, the decomposition module within the FTPS thermal response model contained only estimated properties based on expert opinion.

The primary motivation for executing the previously described TGA campaign was to rigorously characterize the decomposition of attractive FTPS insulators to improve thermal model temperature predictions. Determined activation energies and uncertainties for KFA5 carbon felt and P2250 aerogel felt insulators in this work have now enabled the decomposition module within the thermal response model to be grounded in experimental data rather than estimation. The overall objective of conducting further material property testing is to provide the FTPS thermal model with a more detailed, accurate material

database to reduce the discrepancies between in-depth thermocouple predictions and thermocouple measurements from arc-jet tests.

As thermal response model temperature predictions at depth become more accurate, heatshield thickness and mass margins become more exact, leading to significant mass savings. Minimizing the gap between thermal model temperature predictions and arc-jet temperature measurements facilitates progress towards model validation.

3.4.1 Results - FTPS Thermal Response Modeling with Experimental Activation Energy

The resulting mean activation energies from Standard and Modulated TGA methods were input into a COMSOL thermal response model simulating arc-jet Run 2627 for an FTPS layup containing KFA5 carbon felt insulation and Run 2602 for a layup containing P2250 aerogel felt insulation. The TC Driver approach was used to implement temperature boundary conditions at TC 2 and the physical processes simulated within the insulation stack of the thermal response model predict temperatures at deeper thermocouple locations (TC 3, TC 4, TC 5, and TC 6). The primary reason for placing this boundary condition at the TC 2 location was to focus on the improvement of temperature predictions between layers of insulation, which are most highly effected by changing the insulator decomposition model.

The resulting accuracy of temperature profile predictions after replacing old estimated activation energies with new values determined from the TGA experimental campaign are shown in Figure 59 through Figure 62. Figure 59 and Figure 60 show improvement from KFA5 carbon felt TGA experiments on arc-jet Run 2627 while Figure 61 and Figure 62 show results from P2250 aerogel felt TGA experiments on arc-jet Run 2602.

Figure 59 shows nominal FTPS thermal model predictions with the original decomposition model, created by Sullivan and Baker, where prediction lines (solid lines) are compared with experimentally measured temperatures (symbols) during the arc-jet run. Changes made to this decomposition model feature the updated activation energy and a corresponding updated pre-exponential factor. All other decomposition parameters in the

99

model remained the same, including a reaction order of 1 for simplicity and total weight lost after full decomposition of 97% according to TGA experimental data.
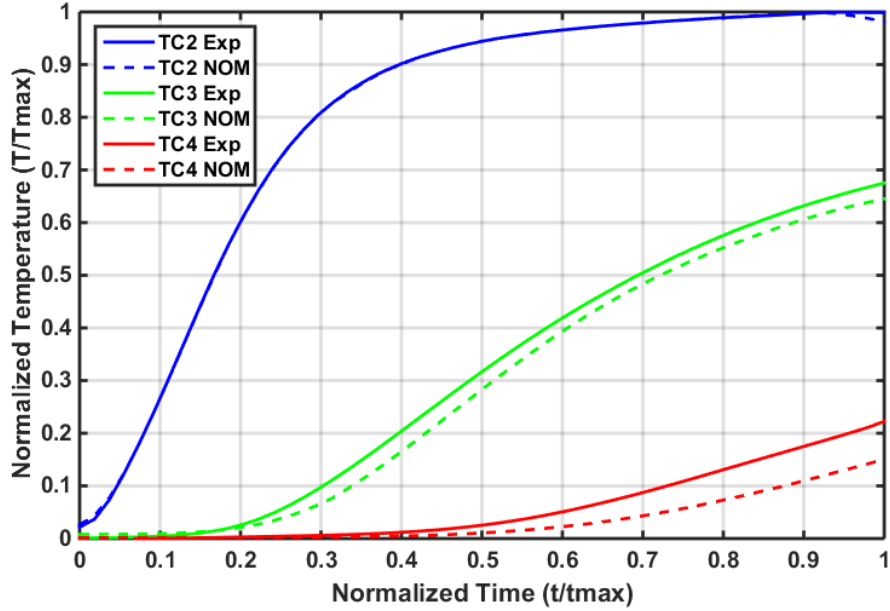
Figure 59: Initial FTPS Thermal Response Model Comparison Between Arc-Jet Thermocouple Measurements (Symbols) and Predictions (Solid Lines) at Depth for KFA5 Run 2627
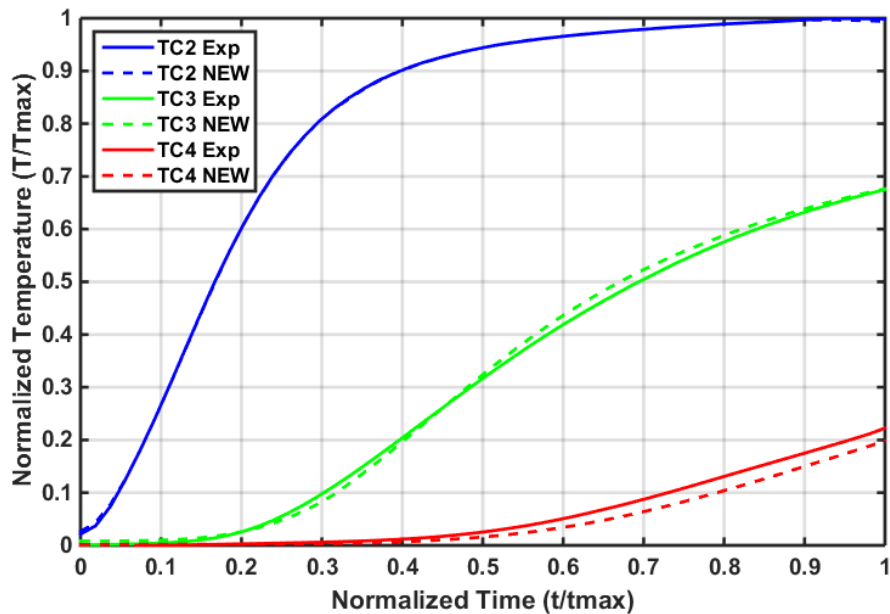
Figure 60: Improved FTPS Thermal Response Model Comparison at Depth for KFA5 Run 2627 Using Activation Energy Determined from Standard and Modulated TGA

Using the mean values for activation energy obtained from the Standard TGA method, the resulting temperature predictions are shown in Figure 60. This plot shows the thermal response model predictions at depth after inputting the mean activation energy value of 131.56 kJ/mol obtained from Standard TGA. Very similar results were obtained if the activation energy was changed to the mean activation energy value of 121.16 kJ/mol from Modulated TGA. Figure 60 shows significantly improved predictions for TC 3 and TC 4.
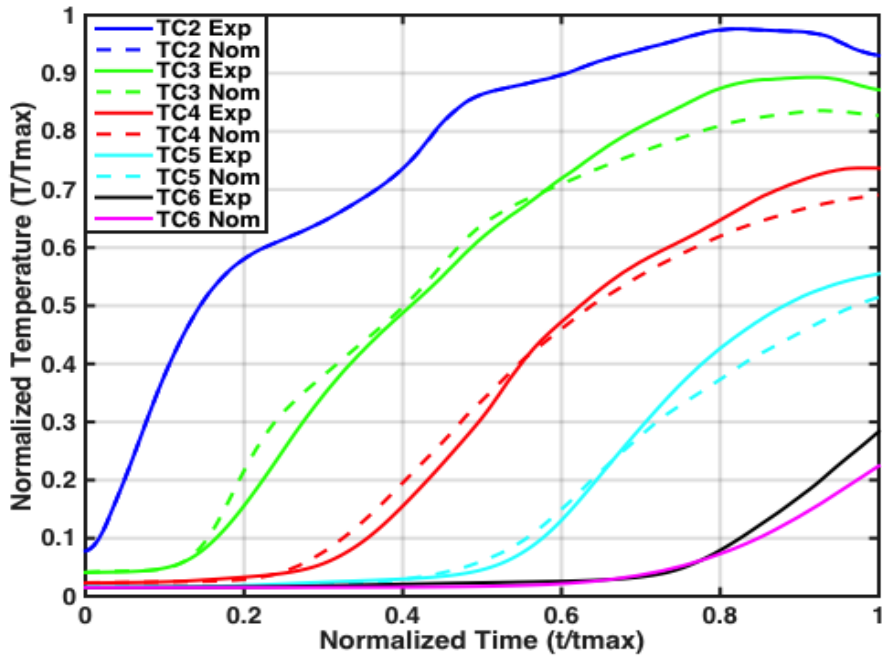
Figure 61: FTPS Thermal Response Model Temperature Prediction Comparison at Depth for Run 2602
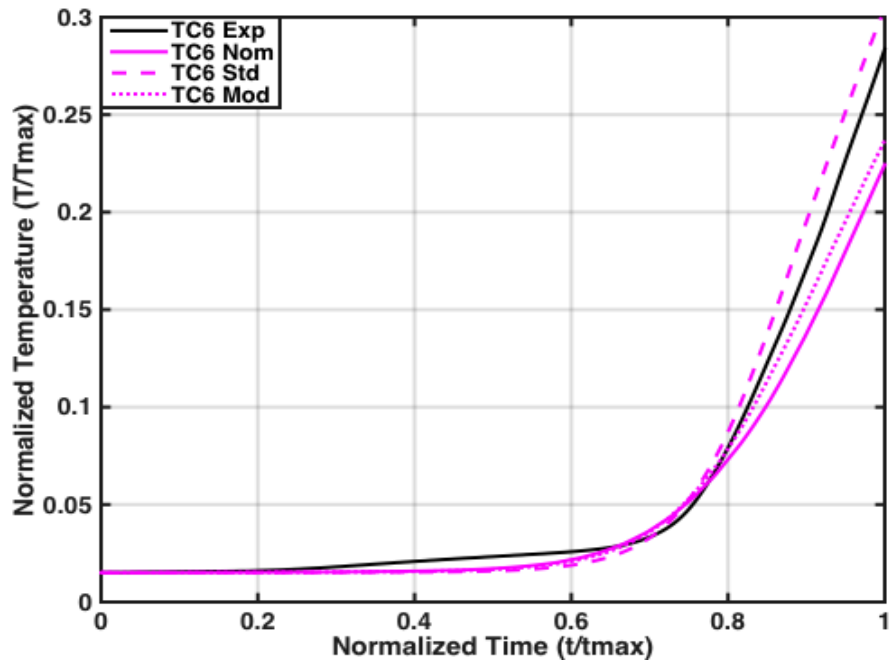
Figure 62: FTPS Thermal Response Model Temperature Prediction Comparison at Depth for Run 2602 Using Activation Energy from Standard and Modulated TGA Testing

The resulting mean activation energies from Standard and Modulated TGA methods for P2250 aerogel felt were also input into a similar thermal response model to observe the resulting accuracy of temperature profile predictions at the bondline (TC6). Figure 61 shows the nominal FTPS thermal model predictions with the original two-reaction decomposition model created by Sullivan and Baker where prediction lines (dashes) are compared with experimentally measured temperatures in an arc-jet (solid lines). The only changes that were made to this decomposition model were applied to the first decomposition event. The activation energy was changed according to the data gathered above and the reaction order of the first reaction was changed from 16 to 1 for simplicity. Resulting bondline predictions were assessed in Figure 62. This plot shows the bondline temperature predictions at depth using the mean activation energy of 254 kJ/mol obtained from Standard TGA testing and 181 kJ/mol obtained from Modulated TGA testing. Figure 62 shows significantly improved predictions at the bondline (TC6) for both Standard and Modulated TGA methods.

3.5 Summary

Higher-fidelity conceptual thermal models have been created to simulate arc-jet testing and predict temperatures at depth through FTPS stackups. Previous work has estimated the activation energy of FTPS insulators using little or no TGA experiments. This produces a very rough estimate of activation energy without treatment of uncertainty.

The Standard TGA (Ozawa-Flynn-Wall) method requires at least one TGA experiment at each of 4 different heating rates over a relevant temperature range that encapsulates the desired decomposition event. The Modulated TGA method only requires one experiment to calculate activation energy. The activation energies are calculated according to previously described ASTM procedures, and the corresponding uncertainty distributions are obtained according to the methodology presented in this work.

The mean activation energy for KFA5 carbon felt was determined to be 131.56 kJ/mol and 121.16 kJ/mol for Standard and Modulated TGA methods, respectively. Limited TGA testing resources in the past have resulted in rough approximations FTPS insulator activation energy with little knowledge of uncertainty. This TGA experimental campaign determined the corresponding activation energy uncertainty for carbon felt samples using an experimental t-distribution. The activation energy standard deviation was determined to be 5.79 kJ/mol and 8.66 kJ/mol for Standard and Modulated TGA methods, respectively. For P2250 aerogel felt, the mean and standard deviation of the t-distribution obtained from Standard TGA experiments are approximately 257 kJ/mol and 17 kJ/mol, respectively. The mean and standard deviation of the t-distribution obtained from Modulated TGA experiments is approximately 181 kJ/mol and 1.5 kJ/mol, respectively.

Preliminary thermal model response results with updated values for the activation energy show great promise for the new decomposition models. Knowledge of these quantities furthers the understanding of how KFA5 carbon felt behaves at high temperatures in an oxidative environment and how P2250 aerogel felt behaves at high temperatures in an inert environment. Significant improvement in the thermal response

model temperature predictions was achieved at thermocouple locations between layers of FTPS insulation for KFA5 carbon felt and at the bondline for P2250 aerogel felt. Additionally, the mean and standard deviation values of activation energy t-distributions for both methods show excellent agreement, which suggests that Modulated TGA should be pursued as a technique to obtain similar activation energy measurements as Standard TGA while saving 75% of the experimental effort.

CHAPTER IV

FTPS DUAL-INSULATOR DESIGN METHODOLOGY

4.1 Introduction

In traditional TPS design, it is common to perform an exhaustive ground-test series to design heatshield materials. Such an approach uses a great deal of resources. Integrating a validated FTPS thermal response model into the design process has the potential to allow efficient exploration of the insulation configuration design space. Not only will this reduce experimental resources required in design of a FTPS insulation configuration, it will provide insight into mission performance to promote more accurate FTPS margining. This new methodology combines thermal response modeling techniques with simulation-based design concepts to design a FTPS insulation stack.

4.1.1 Insulation Design Methodology Developed for FTPS

Thermal response models containing layers from attractive insulators are developed to find FTPS insulation stackup alternatives that meet nominal mission requirements. Currently, FTPS insulator configuration selection is heavily based on performance in the arc-jet facility. Whichever layup produces the lowest peak bondline temperature is seen as the "best" layup. This investigation presents a streamlined and efficient process that can be used to design a dual-insulator configuration of an FTPS insulator stack for EDL on an atmospheric body while conserving experimental resources. Focus will be placed on potential HIAD atmospheric entry Earth missions as a proof of concept, but the interested designer can apply this methodology for EDL to other atmospheric entry missions as well.

4.2 FTPS Dual-Insulator Design Methodology

The FTPS insulator design methodology proposed in this investigation is shown in Figure 63. Major contributions from this dissertation are highlighted by thick, green

borders on boxes. It is assumed that unattractive candidate insulators have already been eliminated from the starting FTPS candidate insulator pool. The "Thermal Material Properties" box represents the experimental determination of decomposing insulator activation energy and its associated distribution. The "Extended Inverse Estimation Methodology" box is used to validate thermal response models for design. The "Monte Carlo Probability of Success" box represents the probability of success calculation that will be used to evaluate FTPS insulator stackup configurations for specific atmospheric entry trajectories. As a final result, FTPS insulator design alternatives will be shown as feasible solutions for a specific upcoming atmospheric entry mission.

The FTPS dual-insulator design methodology includes the inputs, the validation process, the design process, and the outputs illustrated in Figure 63. This methodology allows for designers to use simulation-based decision-making when designing the FTPS insulation stack, which is a significant advancement beyond the current ad-hoc, ground-test based decision-making process. As a result, the presented methodology can obtain feasible dual-insulator designs while saving a great deal of experimental resources.
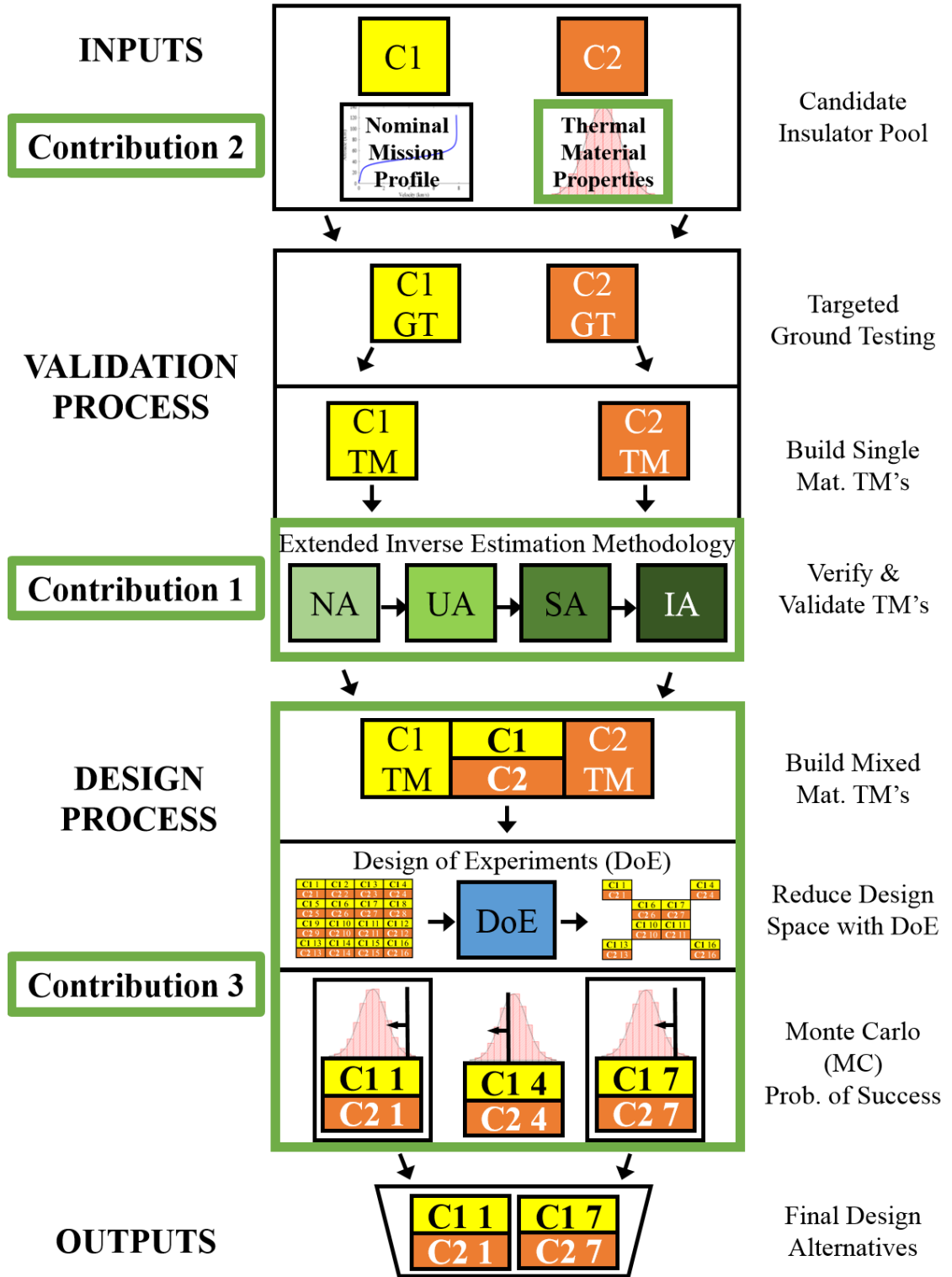
Figure 63: FTPS Dual-Insulator Design Methodology

4.2.1 Inputs

The methodology begins with a pre-screened pool of candidate insulators (C1 and C2), the corresponding thermal-material properties for each insulator, and a nominal atmospheric entry mission profile shown at the top of the flowchart in Figure 63.

4.2.2 Validation Process

After assembling inputs into the methodology, the design process can begin to efficiently find the most attractive dual-insulator stackup configuration alternatives for specific mission scenarios with limited resources. Targeted arc-jet testing is performed on FTPS layups containing multiple layers of one insulation type. The extended inverse multi-parameter estimation methodology developed in Chapter 2 is implemented on two single-insulator thermal response models to improve thermal-material property estimates and achieve temperature prediction validation with multiple arc-jet thermocouple measurements. In other words, parameter estimation was performed on one thermal response model containing insulation layers of only the C1 insulator and another containing insulation layers of only the C2 insulator. The improved material properties from the parameter estimation methodology are then incorporated into a dual-insulator thermal response model in the beginning of the design process.

4.2.3 Design Process

In order to use the thermal response model as a design tool, one must apply the appropriate flight-relevant boundary conditions. After trajectory dispersions have been generated, realistic estimates for heat flux and surface pressure profiles are obtained. These profiles are then imported into FTPS thermal response models as boundary conditions to generate temperature predictions between FTPS layers for the nominal mission architecture.

A full-factorial design space search evaluates every possible combination of designs. After achieving validation, a full-factorial search would require the analyst to create and evaluate one thermal response model for each FTPS insulator configuration combination,

which is extremely time consuming. Design of Experiments (DoE) methods are is utilized to enable an efficient exploration of FTPS insulator configuration design space under the constraint of limited experimental resources. This work assumes that the final FTPS layup consists of a fixed number of total insulation layers from 2 different types of FTPS insulation materials. Approximately four insulation stack configurations of C1 and C2 layers will be evaluated, each requiring its own thermal model for evaluation. Using a DoE for down-selection near the final steps of the design methodology reduces the number of FTPS thermal response models that need to be evaluated to arrive at a final FTPS insulator configuration design.

4.2.4 Outputs

After the FTPS insulator configuration down-selection is executed with a DoE, a Monte Carlo simulation can be performed on each thermal model by varying boundary conditions and material properties within their $\pm 3\sigma$ uncertainty bounds. This will produce a resulting probability distribution of peak-bondline temperatures used to evaluate which candidate insulators have the highest probability of mission success, or lowest peak bondline temperatures, for a specified trajectory type and atmosphere. Based on these results, the final FTPS insulator configuration layups are presented as design alternatives with a known probability of success.

4.3 HULA Nominal Mission Description

The HULA atmospheric entry mission was chosen to demonstrate the FTPS dual-insulator design methodology. Over the past decades, ULA has been one of the nation's leaders in supplying payloads access to space. Recently, ULA has considered using a HIAD to return its Centaur second-stage to Earth's surface, allowing re-use of the system. For the past three years, the HIAD team at NASA Langley Research Center has worked closely with ULA to design a flight test as a proof of concept for returning the Centaur second-stage.

4.3.1 Background

The HULA concept mission has strong heritage traced back to previous HIAD missions. The most recent HIAD flight test was IRVE-3 performed in 2012 by the HIAD team at NASA LaRC [2], [60]. A preliminary concept of operations is shown for IRVE-3 in Figure 64.
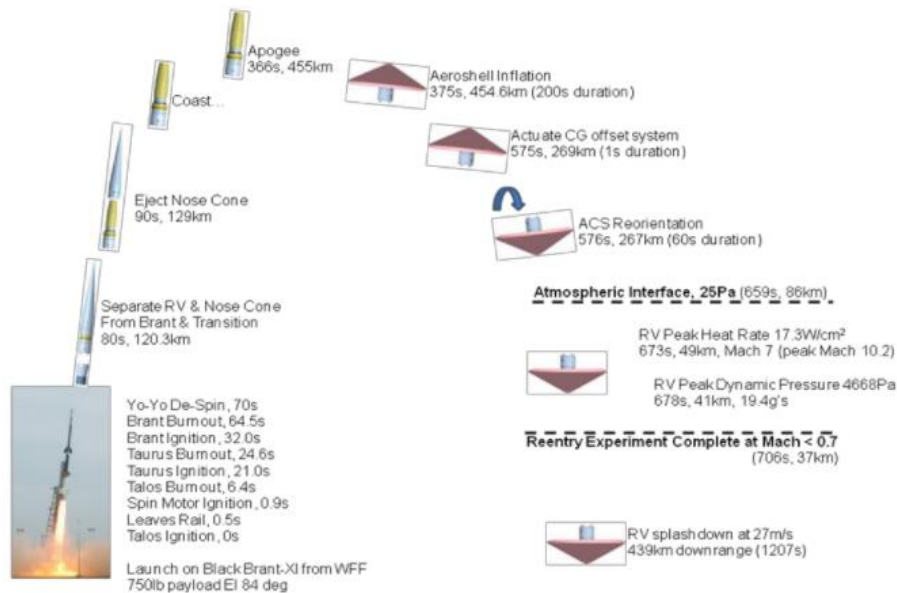
Figure 64: IRVE-3 Concept of Operations [95]

IRVE-3 was 3 meters in diameter at full deployment with a 60-degree half-cone angle shape. IRVE-3 demonstrated that a HIAD can survive a sub-orbital Earth-entry with a peak heat flux of 15 W/cm^2. It also demonstrated a novel center-of-gravity (CG) shifting device that allowed the HIAD to fly a lifting trajectory. Key elements from the IRVE aerodynamic database were used to develop the aerodynamic database for the next proposed HIAD mission, called HEART.

The years that followed IRVE-3 pushed for a new proposed mission (HEART) that aimed to deliver downmass cargo from the International Space Station (ISS) to the surface [96]. The HEART vehicle was designed to have a fully-deployed diameter of 8.5 meters with 55 degree half-cone angle [2]. Peak heat rate was expected to be slightly higher than IRVE-3, approximately 25 W/cm^2. A concept of operations for HEART is shown in

Figure 65. Figure 66 compares a fully deployed HEART vehicle with Mars Science Laboratory (MSL), illustrating that the HIAD concept can have a larger deployed diameter and lower ballistic coefficient than a launch vehicle shroud would allow.
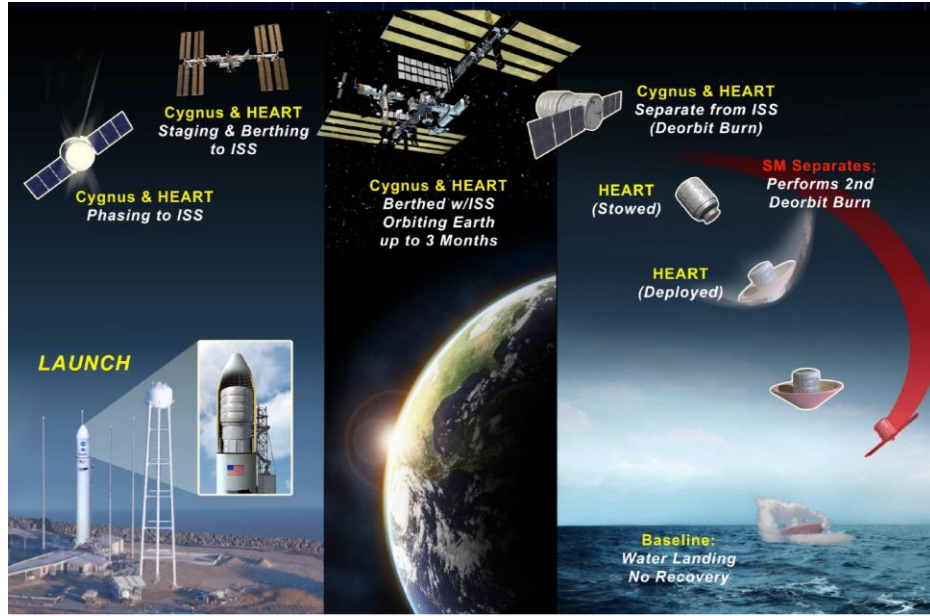
Figure 65: HEART Concept of Operations [97]
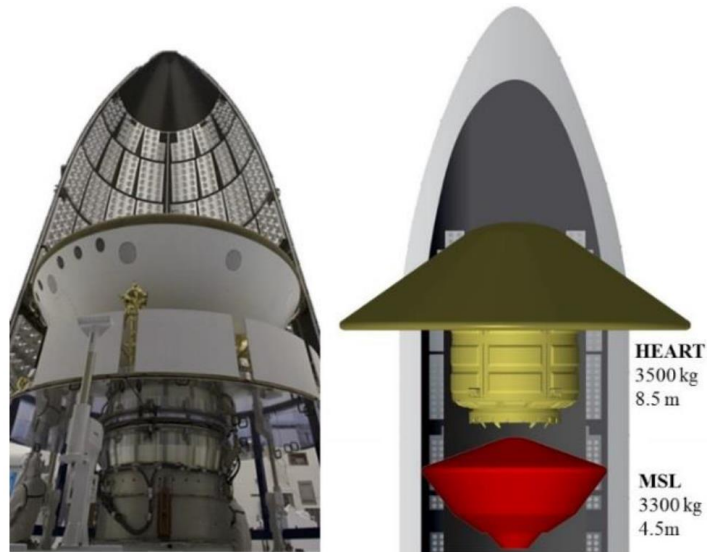
Figure 66: Heatshield Diameter vs. Shroud Diameter for MSL and HEART [60]

HEART was poised to advance the HIAD technology beyond IRVE-3 by entering from Low Earth Orbit (LEO) with a larger payload mass and a higher expected peak heat flux. Although the mission was ultimately cancelled, the analysis used to develop the HEART mission concept was carried over to develop HULA. Most notably, the aerodynamic database developed for HEART was used to design the HULA nominal mission with acceptable accuracy. A conceptual design of the HULA vehicle is shown in Figure 67 for reference.
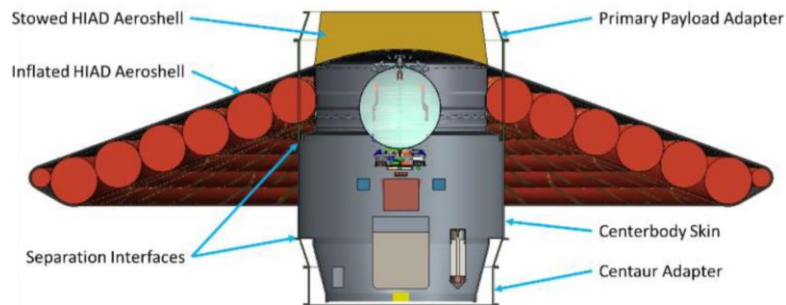
Figure 67: HULA Conceptual Design [60]

HULA is most similar to HEART because it is delivering a payload safely to Earth's surface from LEO. However, there are a few key differences in HULA's vehicle design. The fully-deployed diameter is designed to be 6 meters with a 70 degree half-cone angle shape. These design differences are driven by the expected peak heat-flux of approximately 50 W/cm^2, which is about twice as high as HEART. In contrast, HULA is still significantly larger than it's predecessor, IRVE-3, as shown in Figure 68.

Figure 68: IRVE-3 (Left) vs. HULA (Right) [60]

4.3.2 Mission Objectives

The primary objective of the HULA mission is to provide ULA with the capability to return the Centaur second-stage safely to the Earth's surface for re-use. A HIAD provides a solution to increase drag area and protect Centaur from atmospheric entry heating without adding significant mass.
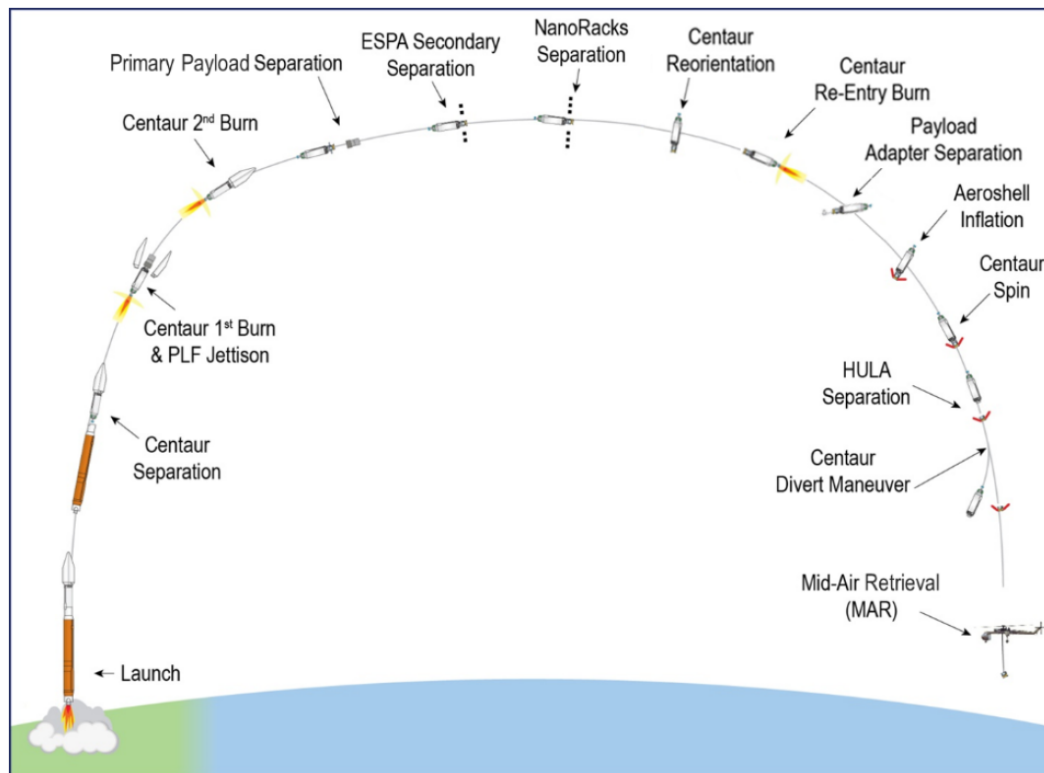
Figure 69: HULA Concept of Operations [62]

The nominal HULA mission considered in this investigation is the first of several flight-tests, and a preliminary concept of operations is shown in Figure 69. The left side of the figure shows a ULA launch vehicle followed by separation of the Centaur second-stage from the first-stage booster. The Centaur vehicle jettisons the payload into LEO and performs a burn to prepare for re-entry. The HIAD is deployed and the vehicle is spun up to provide stability throughout entry. For this first flight-test, the HIAD will only protect

the Centaur second-stage for the first portion of entry. The Centaur will perform a divert maneuver to separate from the HIAD. The Centaur will fall into the ocean while the HIAD will deploy a parasail to be retrieved in mid-air by a helicopter.

4.3.3 Trajectory Analysis

Trajectory analysis for the HULA mission was performed using the Program to Optimize Simulated Trajectories II (POST2). POST2 is a multiple degree of freedom (DOF) tool used at NASA LaRC to analyze launch trajectories, entry trajectories, and many types of additional trajectories [98]. POST2 does have the ability to optimize trajectories, but the current investigation makes use of its ability to predict atmospheric and heating boundary conditions during atmospheric entry.

For this study, POST2 was used to generate a nominal HULA ballistic Earth entry trajectory with 3DOF. Earth's atmosphere was modeled using Earth Global Reference Atmosphere Model (GRAM) 2010 version 4. The aerodynamic database was a modified version of the HEART aerodynamic database developed by Korzun [61]. This database included free molecular solutions at high altitude, HEART solutions from Mach 25 to Mach 3, and IRVE-3 solutions for velocities less than Mach 3. Finally, an aerothermal database developed by Johnston was used to estimate atmospheric entry heating. In the HIAD Mission Applications study, Johnston used state-of-the-art coupled LAURA (Langley Aerothermodynamic Upwind Relaxation Algorithm) and HARA (High-temperature Aerothermodynaic RAdiation) solutions to calculate estimates for convective and radiative heating [61].

4.4 FTPS Design Methodology Inputs for HULA

The FTPS dual-insulator design methodology has three inputs: two candidate insulators, corresponding thermal-material properties for both insulators, and a nominal atmospheric entry mission. As mentioned previously, this methodology is performed at a high-level to find which dual-insulator combination is best suited for the selected nominal mission. Once the methodology is complete, high-performing design alternatives will be assessed for

further arc-jet testing. As such, this simulation-based design methodology filters out poor-performing dual-insulator combinations early-on, before significant arc-jet testing begins.

4.4.1 Nominal Mission Profile

The HULA vehicle had a diameter of 6 meters, a half-cone angle of 70 degrees, and a ballistic coefficient of 40 kg/m^2. The nose radius of the vehicle was assumed to be 25% of the HIAD deployed diameter and the total vehicle mass was calculated to be 1784.4 kg [60]. Nominal trajectory profiles are shown in Figure 70. Some quantities of note include a peak heat flux of approximately 55 W/cm^2, a peak dynamic pressure of approximately 4000 Pa, and an integrated heatload of approximately 3500 J/cm^2.
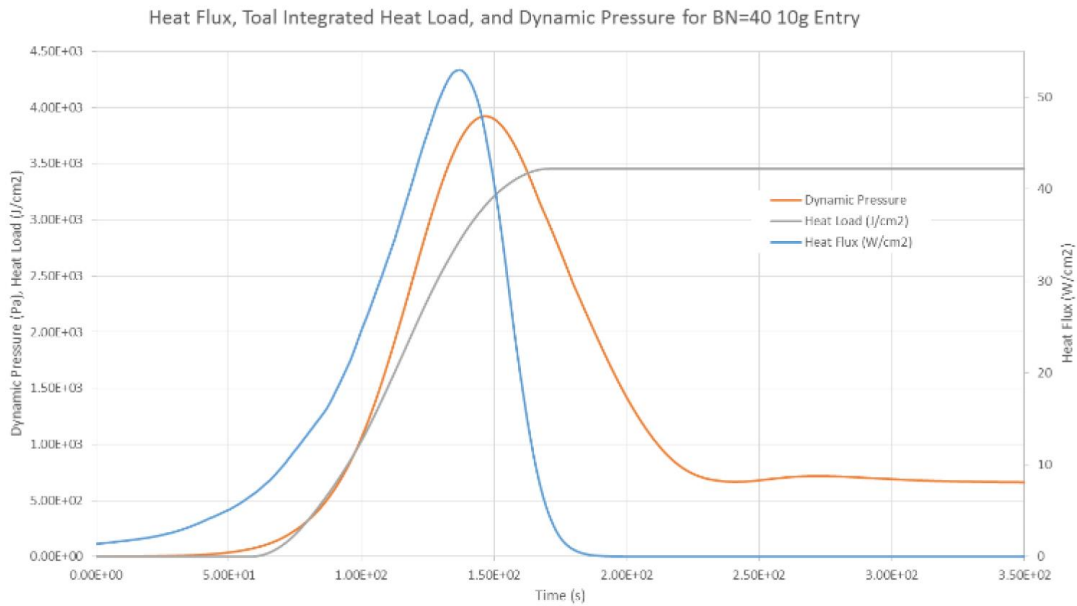
Figure 70: HULA Nominal Trajectory Profiles[60]

In the HULA concept of operations, it is assumed that the Centaur second-stage provides a delta-v to decrease the entry flight-path angle. The Centaur engine specific impulse (Isp) was assumed to be 450 s producing an instantaneous delta-v of approximately 108.3 m/s at apogee. As a result, a peak deceleration of approximately 10g's was assumed.

Using POST2, Zumwalt produced trajectory dispersions about the HULA nominal trajectory [99]. A total of 2000 trajectories were produced using a Monte Carlo simulation. Inputs such as aerodynamics, delta-v at apogee, and total vehicle mass were varied between their $\pm 3\sigma$ uncertainty bounds to produce trajectory dispersions. The $\pm 3\sigma$ uncertainty for aerodynamics results in a $\pm 3\%$ uncertainty for C_D at atmospheric entry interface and a $\pm 20\%$ uncertainty upon ocean landing. The $\pm 3\sigma$ uncertainty for delta-v translated to a $\pm 2\%$ delta-v uncertainty and a $\pm 2.5\%$ flight path angle uncertainty at atmospheric interface.

4.4.2 Candidate Insulators in FTPS Layup

The main purpose of the FTPS dual-insulator design methodology is to perform an efficient evaluation of two FTPS insulators that have not yet been tested together in an arc-jet. The two candidate insulators considered in this investigation to demonstrate the methodology are KFA5 and Saffil. Figure 71 shows an exploded view of the HULA vehicle FTPS heatshield attached to the inflated aeroshell.
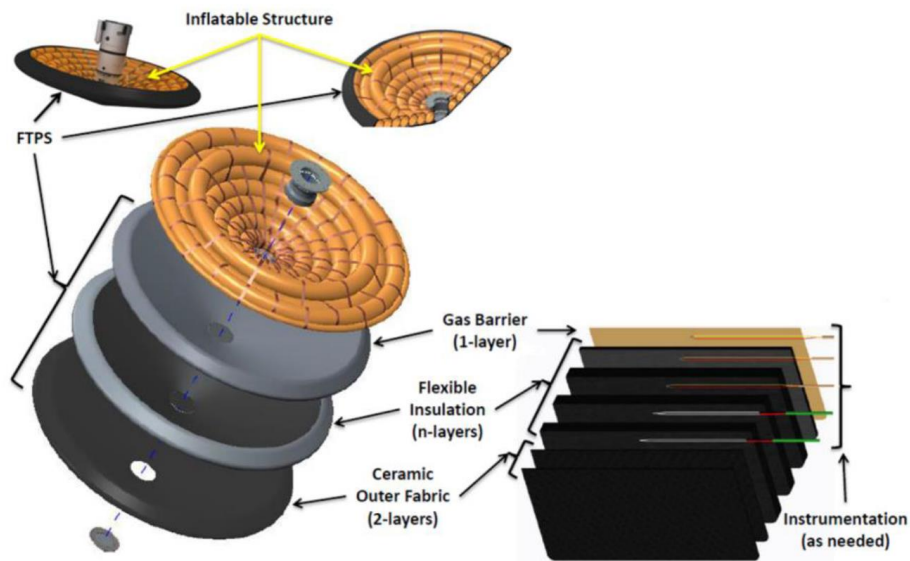
Figure 71: HIAD Exploded View of FTPS and TC Instrumentation [62]

Note that, in the reference [62] design, the two layers of outer fabric material and one layer of gas barrier material have been fixed, meaning the number of layers and material type has already been decided. However, this investigation assumes Silicon-Carbide (SiC)

116

for the outer fabric material and Kapton for the gas barrier material. The insulation region is denoted by "n-layers" which means it can be tailored depending on the selected nominal mission. The proposed dual-insulator design methodology is aimed at doing just that – finding out what that insulator configuration should be.

4.4.3 Thermal-Material Properties

Chapter 2 used an extended inverse multi-parameter estimation methodology to improve thermal response model predictions for layups containing layers of only KFA5 and layers of only Saffil. Arc-jet thermal response model improvements have been incorporated into the HULA thermal response model by adjusting key thermal-material properties within their $\pm 3\sigma$ uncertainty bounds. These thermal-material properties were adjusted using scale factors multiplied by corresponding thermal-material properties. Nominal values of all scale factors was 1 (no effect). The following discussion shows which scale factors were adjusted and how their input distributions were changed. The scale factor adjustments obtained from KFA5 and Saffil thermal response models in Chapter 2 are summarized in Table 8.

Table 8: Updated Uncertainty Analysis Scale Factor Distribution Statistics

Distribution Statistics	KFA5 k (SF)	KFA5 Por (SF)	SAF k (SF)	GB Cp (SF)
(μ) Mean	1.138	0.97	0.882	0.925
(σ) Std. Dev.	0.100	0.010	0.100	0.025
($+3\sigma$) Value	1.438	1	1.182	1
(-3σ) Value	0.838	0.94	0.582	0.850
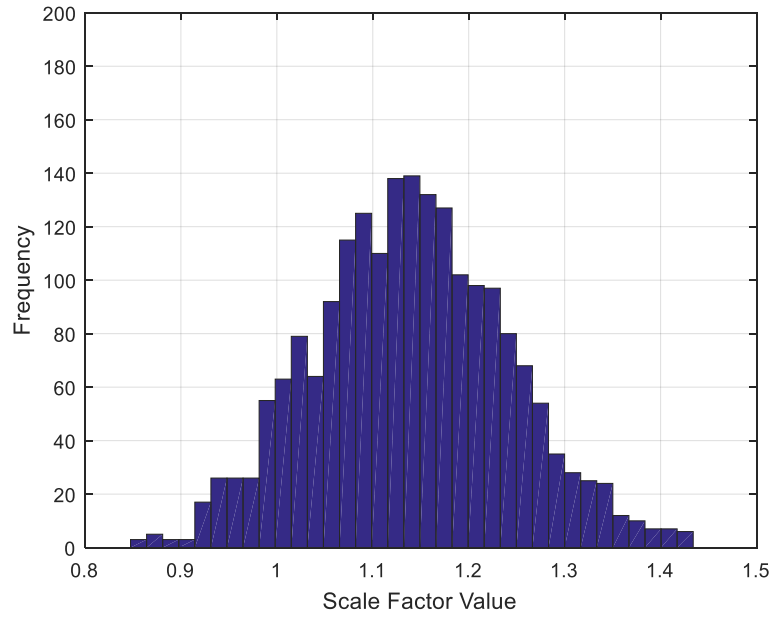
Figure 72: KFA5 Thermal Conductivity Shifted Scale Factor Distribution
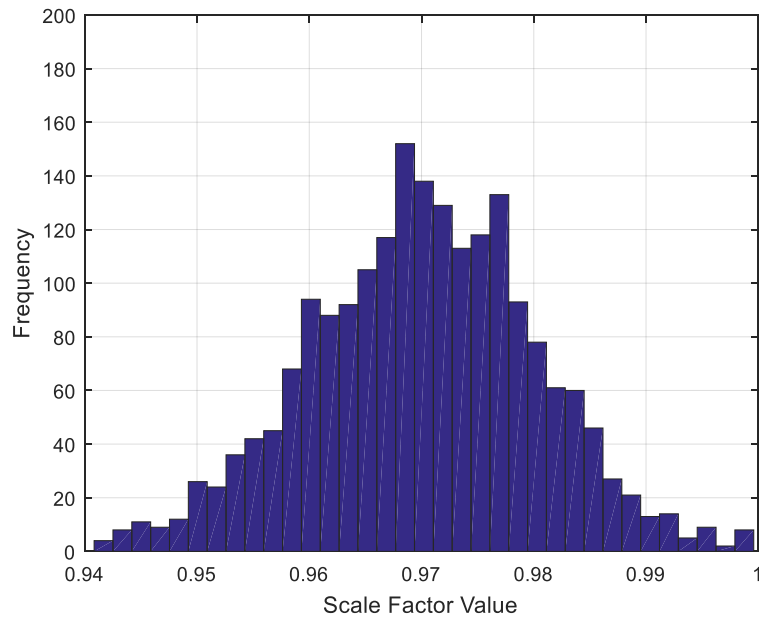
Figure 73: KFA5 Porosity Shifted Scale Factor Distribution

The extended inverse multi-parameter estimation methodology performed on the KFA5 thermal response model suggested adjusting thermal conductivity and porosity to reduce error in temperature predictions. The original scale factor distribution for thermal

118

conductivity had a mean of 1, a standard deviation of 0.1, and resulting ±3σ bounds ranging from 0.7 to 1.3. As for porosity, the original scale factor distribution had a mean of 1, a standard deviation of 0.01, and resulting ±3σ bounds ranging from 0.97 to 1.03. Performing inverse analysis with these two parameters yielded slightly adjusted values of 1.138 for thermal conductivity and 0.97 for porosity. In order to carry these improvements over to the HULA thermal response model, the means of the scale factor input distributions for KFA5 thermal conductivity and porosity were shifted to reflect the values from inverse analysis. The new KFA5 thermal conductivity scale factor input distribution shown in Figure 72 has mean of 1.138, the same standard deviation of 0.1, and resulting ±3σ bounds ranging from 0.838 to 1.438. The new KFA5 porosity scale factor input distribution shown in Figure 73 has mean of 0.97, the same standard deviation of 0.01, and resulting ±3σ bounds ranging from 0.94 to 1.00.
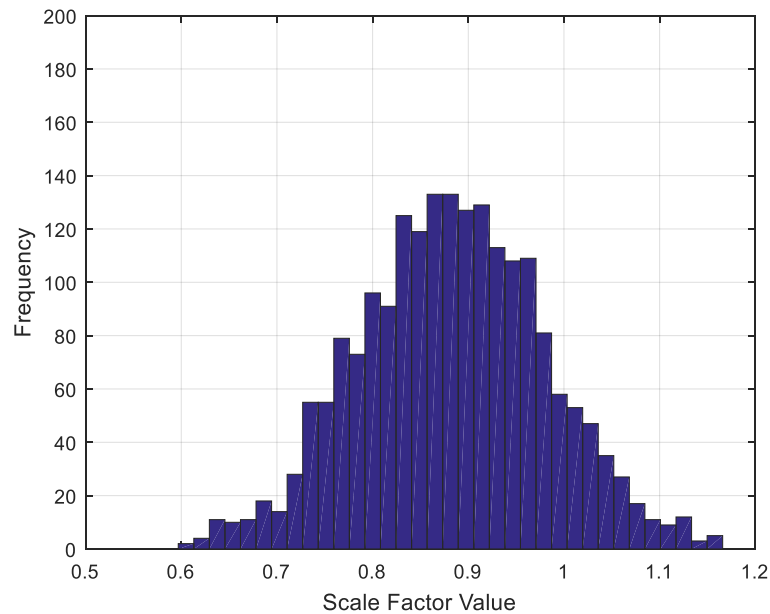
Figure 74: Saffil Thermal Conductivity Shifted Scale Factor Distribution
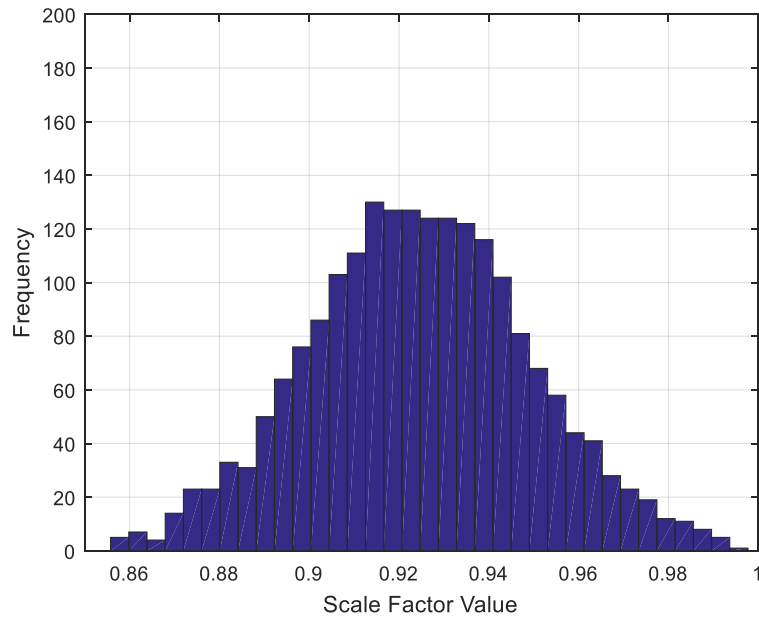
Figure 75: Gas Barrier Specific Heat Shifted Scale Factor Distribution

Similar adjustments were made using the results of the extended inverse multi-parameter estimation methodology performed on the Saffil thermal response model. The methodology results recommended adjusting the scale factors for Saffil thermal conductivity and the Kapton Gas Barrier specific heat. The original scale factor distribution for Saffil thermal conductivity had a mean of 1, a standard deviation of 0.1, and resulting $\pm 3\sigma$ bounds ranging from 0.7 to 1.3. As for the Kapton Gas Barrier specific heat, the original scale factor distribution had a mean of 1, a standard deviation of 0.025, and resulting $\pm 3\sigma$ bounds ranging from 0.925 to 1.075. Performing inverse analysis with these two parameters yielded slightly adjusted values of 0.882 for Saffil thermal conductivity and 0.925 for Kapton specific heat. Like before, the means of these scale factor input distributions were shifted accordingly in the HULA thermal response model. The new Saffil thermal conductivity scale factor input distribution shown in Figure 74 has mean of 0.882, the same standard deviation of 0.1, and resulting $\pm 3\sigma$ bounds ranging from 0.582 to 1.182. The new Kapton Gas Barrier specific heat scale factor input distribution shown in

Figure 75 has mean of 0.925, the same standard deviation of 0.025, and resulting $\pm 3\sigma$ bounds ranging from 0.85 to 1.00.

4.4.4 FTPS Dual-Insulator Thermal Response Model

A thermal response model can apply boundary conditions that a ground-test cannot replicate, making it a useful tool in evaluating performance for a nominal entry mission trajectory. In this thermal response model, boundary conditions are applied to the FTPS surface throughout each trajectory and in-depth temperature predictions are produced between layers of FTPS. The most important boundary conditions applied to the HULA thermal response model are the heat flux profile and pressure profile obtained from trajectory analysis. The most important temperature prediction is located at the bondline between the last layer of insulation and the gas barrier layer because the maximum temperature must remain under 400 °C at all times to avoid catastrophic failure.

It is important to note that this investigation focuses only on designing the insulation stack for the vehicle's nose, or the stagnation point. Figure 71 shown previously illustrates a circular cutout through the center of the aeroshell and the FTPS heatshield. In its place is a small aluminum piece that behaves as a metal aeroshell on the vehicle's nose. The HULA thermal response model accounts for this by assuming an aluminum backside sitting behind the last layer of FTPS, which is the gas barrier.

One thermal response model was created for each dual-insulator configuration demonstrated in the proposed methodology. Each insulator configuration was evaluated by running its corresponding thermal response model for all 2000 Monte Carlo trajectory dispersions described earlier. Peak bondline temperatures for each trajectory are presented in histograms to determine the resulting mean and expected $+3\sigma$ upper bound values.

121

4.5 FTPS Dual-Insulator Configurations for HULA

4.5.1 HULA FTPS Design Demonstration Assumptions

The proposed methodology designs an FTPS insulation configuration for a nominal HULA mission using two attractive insulators that have never been tested in a wind tunnel together. Different regions of the HIAD FTPS heatshield may suggest different thicknesses, but this investigation focuses on protecting the vehicle's nose location. A Design of Experiments (DOE) technique is used to gain sufficient information about characteristics of the best performing dual-insulator configurations. Generally, a DOE chooses a reduced set of a full-factorial design space to evaluate performance trends efficiently. The problem must be set up properly before applying a DOE to reduce the dual-insulator configuration design space. Both KFA5 and Saffil are considered in this investigation and a sample dual-insulator configuration is shown in Figure 76.

Figure 76: Sample FTPS Dual-Insulator Configuration

It is important to note that one layer of KFA5 and one layer of Saffil have very different thicknesses. A KFA5 layer is a few centimeters thick while a Saffil layer is almost as thin as a sheet of paper. Multiple layers of Saffil were grouped together in order to obtain a more accurate evaluation of relative performance with KFA5. The analyst chose 4 individual Saffil layers to be considered one group because this roughly matched the KFA5 areal weight (mass/area) measurement. Figure 76 shows a sample three-layer dual-insulator configuration containing both KFA5 and Saffil. In addition, this figure specifies that one black layer is equivalent to one layer of KFA5 and one white layer is equivalent to four layers of Saffil. The DOE will only be applied to three-layer dual-insulator

configurations. Second, the four layers of Saffil will be assumed to be "glued together" and treated as one Saffil layer group with an areal weight equivalent to one layer of KFA5.

4.5.2 Initial FTPS Dual-Insulator Configuration Design Space

There are 8 unique three-layer dual-insulator combinations to consider. Figure 77 shows this full-factorial design space.

Config. 1   Config. 2   Config. 3   Config. 4

Config. 5   Config. 6   Config. 7   Config. 8
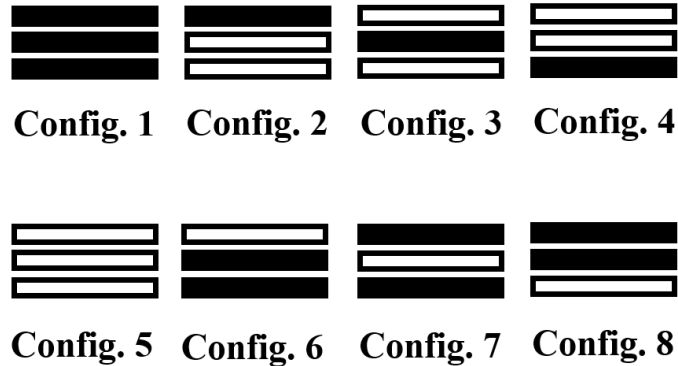
Figure 77: Three-Layer Dual Insulator Configurations

One way to efficiently explore this configuration design space without evaluating every single option enlists the use of a DOE. Specifically, a Taguchi Orthogonal Array DOE has been selected to reduce the analysis set while maximizing experimental information.

4.5.3 Design Space Reduction with Taguchi Orthogonal Array DOE

Taguchi orthogonal arrays are commonly used for experimental applications to maximize the amount of information for a minimum amount of experimental effort. Taguchi arrays are often selected based on the complexity of the problem. For this application, a Taguchi array was selected among other possible DOEs because of its simplicity. The motivated analyst can modify this methodology to use other DOEs to efficiently explore the design space in the future.

Generally, Taguchi arrays become more efficient at reducing experimental effort as the number of options increase. In other words, the more complex the problem is, the more benefit Taguchi arrays provide. Figure 78 visually represents the problem formulation used

123

to reduce the three-layer dual-insulator configuration design space using an L4 Taguchi array.

$$L_4(2^3)$$

Exps.   Levels   Factors

Factors

L1 = Layer 1
L2 = Layer 2
L3 = Layer 3

Levels

━━━━━ = C1: 1 x KFA5 **(1)**

▭ = C2: 4 x Saffil **(2)**
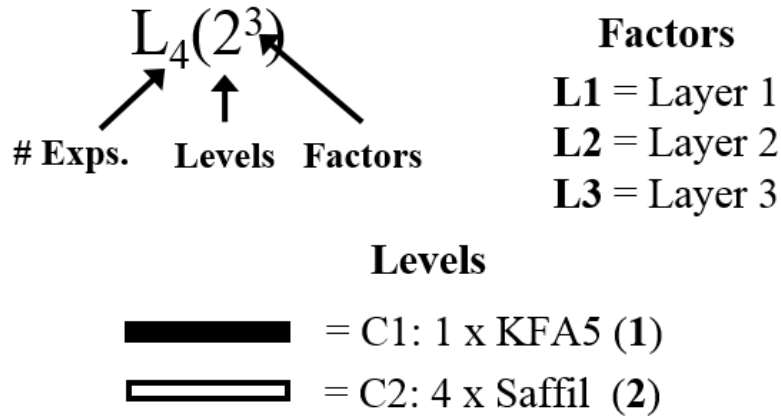
Figure 78: Problem Formulation for Taguchi Orthogonal Array

A $L_4(2^3)$ Taguchi array only requires 4 experiments to efficiently explore the design space. For this application, each insulator is considered one "Level" and each layer is considered one "Factor". C1 refers to the first candidate insulator group, which is equivalent to one layer of KFA5 and represented by a "1". C2 refers to the second candidate insulator group, which is equivalent to four layers of Saffil and represented by a "2". Additionally, specific layers are represented by L1 (top layer), L2 (middle layer), and L3 (bottom layer). Using these problem formulation assumptions, the corresponding Taguchi array is shown in Figure 79. The first column identifies three-layer dual-insulator configurations. Each row specifies a "1" or a "2" for each possible layer (L1, L2, and L3).

$L_4(2^3)$ Taguchi Orthogonal Array

Config. #	L1	L2	L3
1	1	1	1
2	1	2	2
3	2	1	2
4	2	2	1

Figure 79: L4 Taguchi Orthogonal Array

The previous section showed the 8 configurations that compose the full three-layer dual-insulator configuration design space in Figure 77. After reducing the design space using a $L_4(2^3)$ Taguchi array, the 4 configurations analyzed are shown in Figure 80.

Config. 1   Config. 2   Config. 3   Config. 4
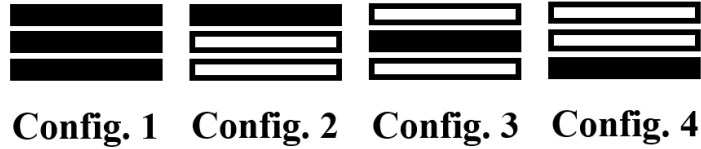
Figure 80: Reduced FTPS Dual-Insulator Configuration Set

Although Config. 1 does not technically contain both insulators, it is prescribed by the $L_4(2^3)$ Taguchi array and becomes a vital comparison metric during the design process.

4.6 FTPS Dual-Insulator Design Demonstration for HULA Using Three-Layered Insulation Stacks

The HULA thermal response model described in section 4.5 is used to evaluate the reduced dual-insulator configuration set shown in Figure 80. One thermal response model is created and evaluated for each of four layups. Boundary conditions derived from the set of dispersed HULA trajectories described in section 4.3 are applied to each thermal response model. Each of the 2000 dispersed trajectories is run for each thermal response model to evaluate simulated performance for the HULA mission. It took approximately four days to run each thermal response model for all dispersed trajectories. Focus is placed on collecting results for the bondline to make sure the temperature limit is not exceeded. In this case, the maximum temperature constraint is influenced by the gas barrier, Kapton, as it begins to disintegrate at approximately 400° C. Therefore, the bondline is considered to be at the TC5 location between the bottom of the last insulation layer and the top of the gas barrier layer. Dec's HIAD FTPS margin policy created in 2013 suggested that the maximum bondline temperature limit should be 250° C, which is a Factor of Safety (FoS) of approximately 60% when compared to the maximum use temperature of 400° C for Kapton [100]. The same maximum bondline temperature constraint of 250° C will be used

in this investigation to evaluate each layup for all dispersed trajectories. Layup performance characteristics are compared and final dual-insulator configurations are suggested for further arcj-jet testing.

4.6.1 Dual-Insulator Configurations – Probability of Success

Four three-layer dual-insulator configurations (Config. 1, Config. 2, Config.3, and Config. 4) were evaluated to compare performance for an upcoming HULA mission. These configurations are referred to as Layup 1, Layup 2, Layup 3, and Layup 4, respectively, from here forward.
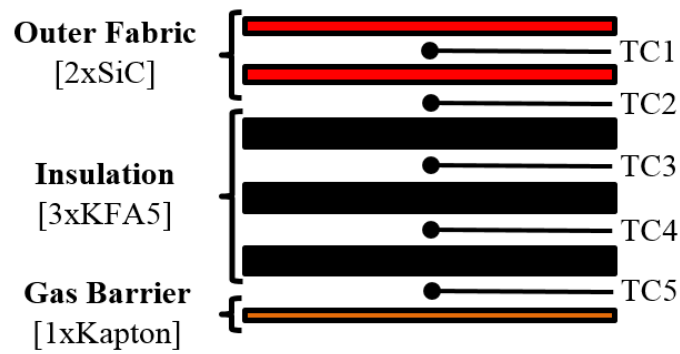
Figure 81: FTPS Dual-Insulator Configuration Design Layup 1

A detailed schematic of Layup 1 is shown in Figure 81. The outer fabric region is composed of 2 layers of SiC fabric and the gas barrier is composed of 1 layer of Kapton. The insulation region is composed of three layers of KFA5 which is abbreviated by using the identifier "3K" (KFA5/KFA5/KFA5). Numbered thermocouple locations are shown between each FTPS layer with focused placed on the TC5 bondline temperature. Bondline temperature predictions for Layup 1 are shown in Figure 82 for all dispersed trajectories. The nominal prediction is shown as a thick, black line while approximated +3σ and -3σ temperature profiles are shown as a red-dashed line and a blue-dashed line, respectively. Finally, the complete set of bondline temperature predictions are shown as thin, green lines. Figure 83 is a histogram of peak bondline temperatures for each trajectory case that is normally distributed.

126

Figure 82: Layup 1 Bondline Monte Carlo Temperature Predictions

Figure 83: Layup 1 Peak Bondline Temperature Distribution

The bondline temperature profiles for Layup 1 shown in Figure 82 have the widest uncertainty bounds near nominal peak temperature around 150 seconds. The peak bondline temperature distribution shown in Figure 83 has a mean of 68.40° C and a standard

deviation of 7.92° C. The corresponding +3σ value is 92.21° C, which is well below the maximum temperature constraint of 250° C.
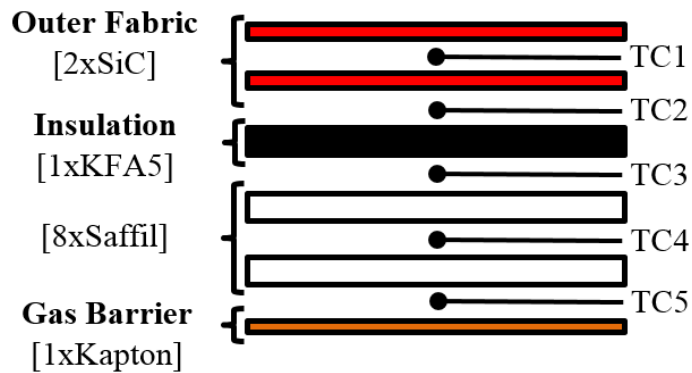
Figure 84: FTPS Dual-Insulator Configuration Design Layup 2

A detailed schematic of Layup 2 is shown in Figure 84. The outer fabrics and gas barrier configurations will remain the same for all layups in this investigation. For Layup 2, the insulation region is composed of one top layer of KFA5 followed by two layer groupings (8 layers) of Saffil, which is represented with the identifier "KSS" (KFA5/Saffil/Saffil). Bondline temperature predictions for Layup 2 are shown in Figure 85 for all dispersed trajectories. A normally distributed histogram of peak bondline temperatures for Layup 2 is shown in Figure 86.
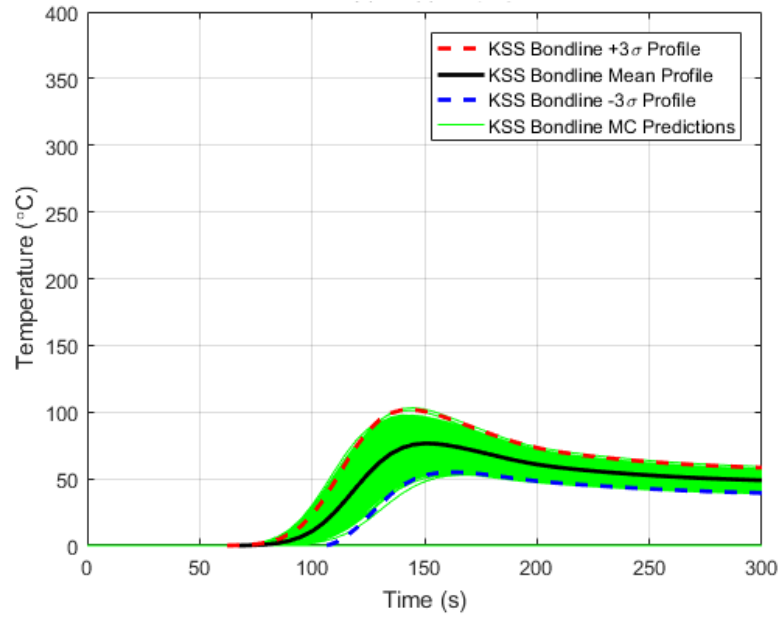
Figure 85: Layup 2 Bondline Monte Carlo Temperature Predictions
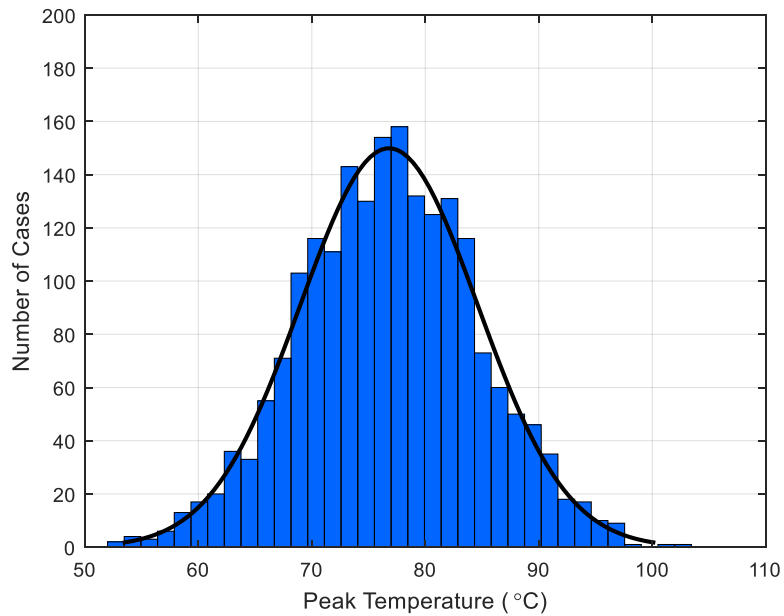
Figure 86: Layup 2 Peak Bondline Temperature Distribution

The bondline temperature profiles for Layup 2 shown in Figure 85 have the widest uncertainty bounds near nominal peak temperature just before 150 seconds. The peak bondline temperature distribution shown in Figure 86 has a mean of 76.80° C and a

standard deviation of 7.82° C. The corresponding +3σ value is 100.27° C, which is well below the maximum temperature constraint of 250° C.
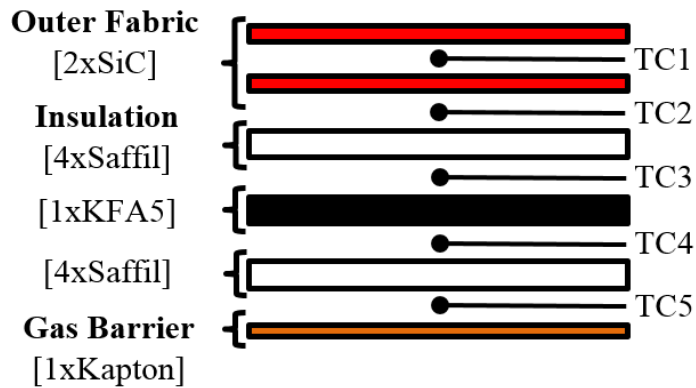
Figure 87: FTPS Dual-Insulator Configuration Design Layup 3

A detailed schematic of Layup 3 is shown in Figure 87. For Layup 3, the insulation region is composed of one top layer grouping of Saffil, one middle layer of KFA5, and one bottom layer grouping of Saffil, which is represented with the identifier "SKS" (Saffil/KFA5/Saffil). Bondline temperature predictions for Layup 3 are shown in Figure 88 for all dispersed trajectories. A normally distributed histogram of peak bondline temperatures for Layup 3 is shown in Figure 89.
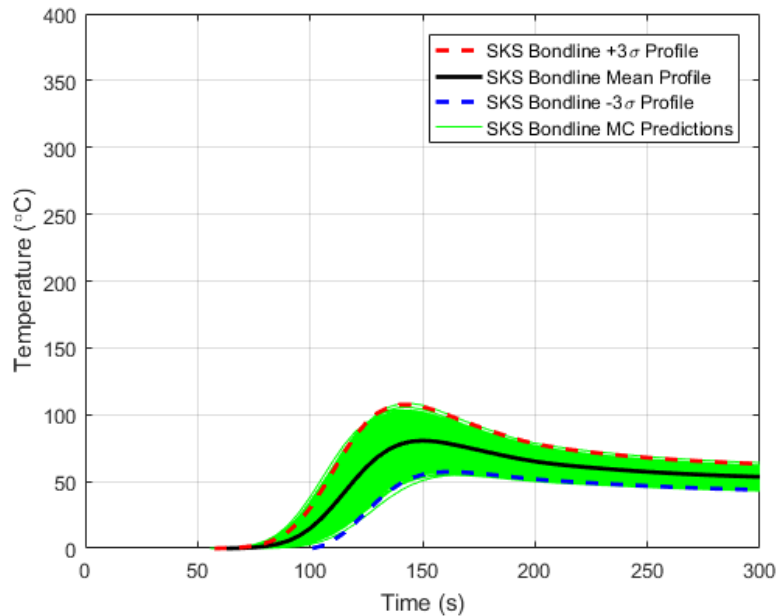
Figure 88: Layup 3 Bondline Monte Carlo Temperature Predictions

130
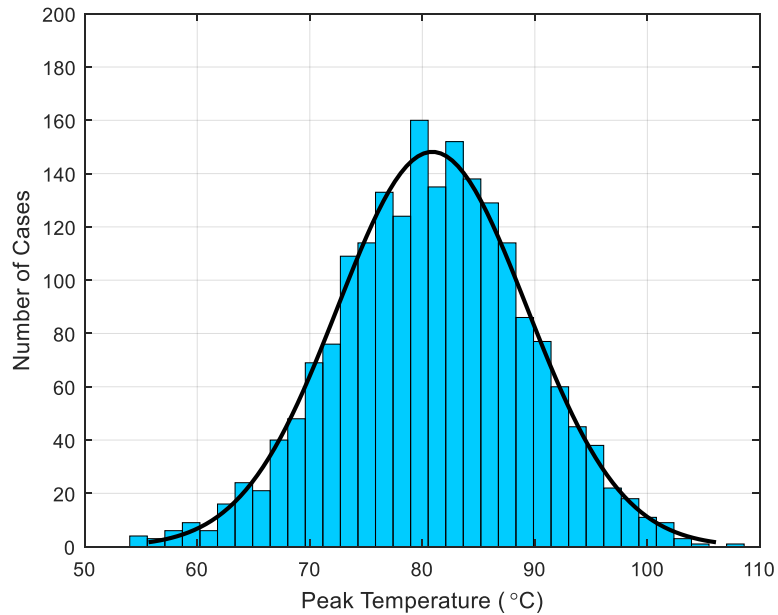
Figure 89: Layup 3 Peak Bondline Temperature Distribution

The bondline temperature profiles for Layup 3 shown in Figure 88 have the widest uncertainty bounds near nominal peak temperature just before 150 seconds. The peak bondline temperature distribution shown in Figure 89 has a mean of 80.83° C and a standard deviation of 8.41° C. The corresponding +3σ value is 106.10° C, which is well below the maximum temperature constraint of 250° C.
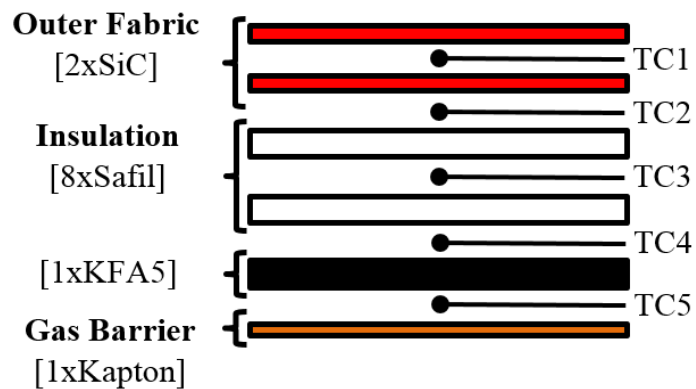
Figure 90: FTPS Dual-Insulator Configuration Design Layup 4

A detailed schematic of Layup 4 is shown in Figure 90. For Layup 4, the insulation region is composed of two top layer groupings of Saffil and one bottom layer of KFA5,

which is represented with the identifier "SSK" (Saffil/Saffil/KFA5). Bondline temperature predictions for Layup 4 are shown in Figure 91 for all dispersed trajectories. A normally distributed histogram of peak bondline temperatures for Layup 4 is shown in Figure 92.
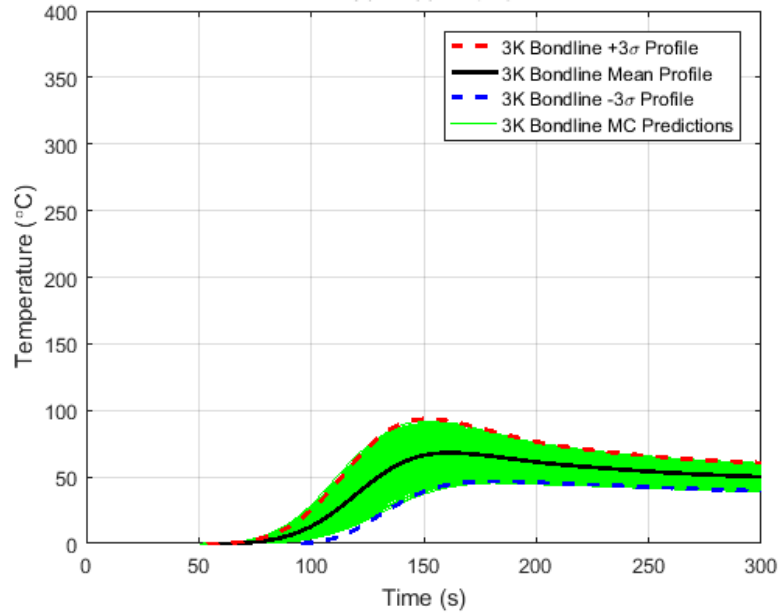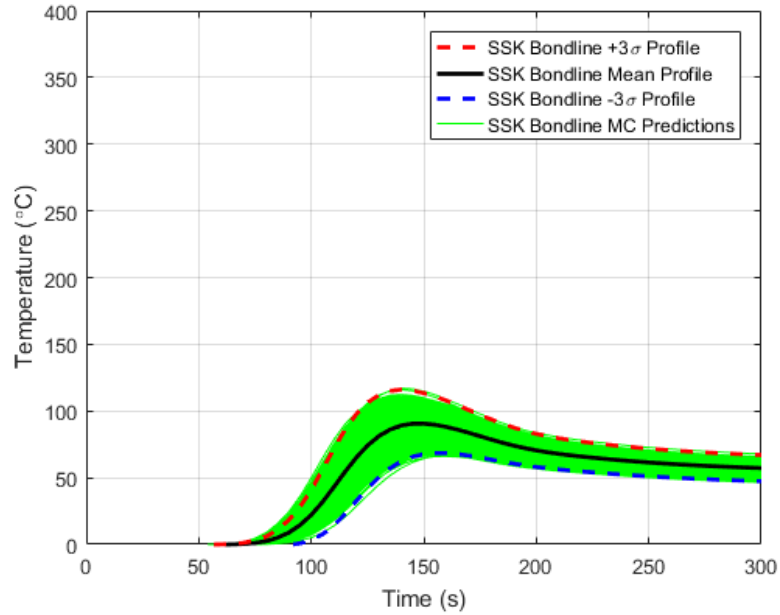

Figure 91: Layup 4 Bondline Monte Carlo Temperature Predictions
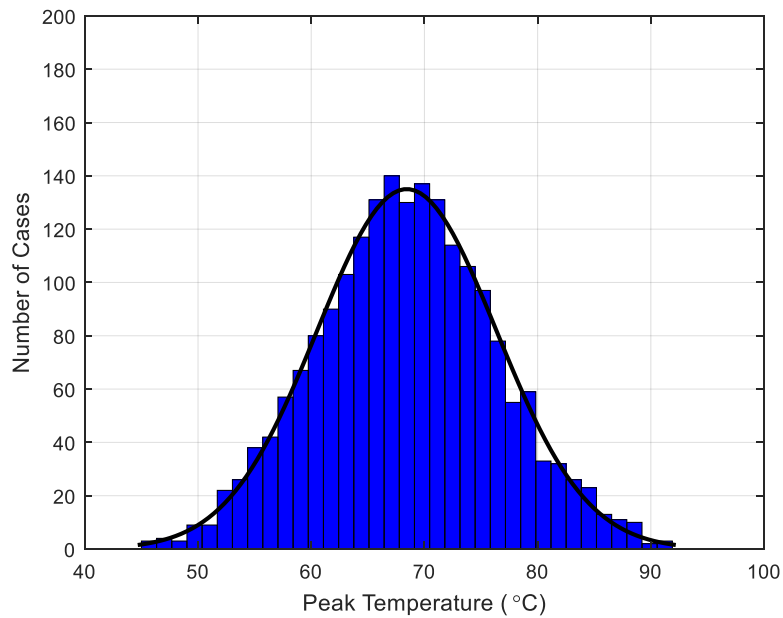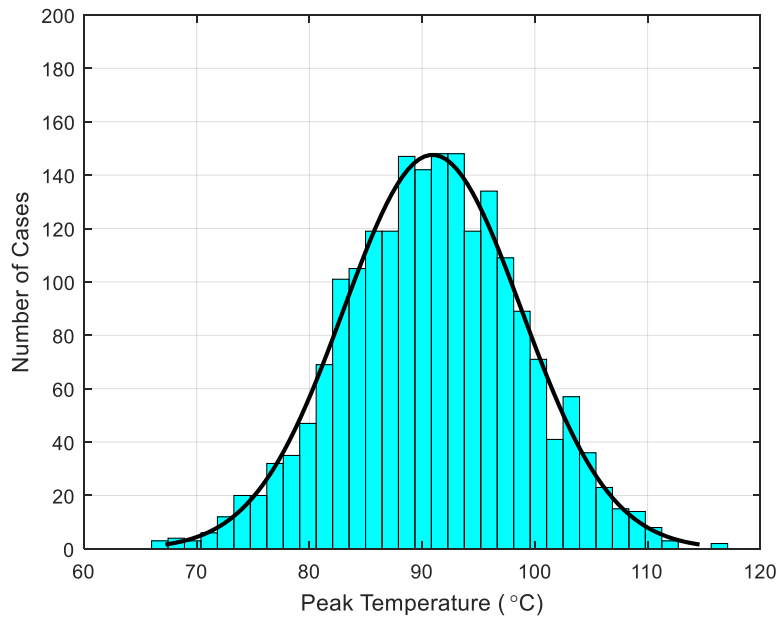

Figure 92: Layup 4 Peak Bondline Temperature Distribution

132

The bondline temperature profiles for Layup 4 shown in Figure 91 have the widest uncertainty bounds near nominal peak temperature just before 150 seconds. The peak bondline temperature distribution shown in Figure 92 has a mean of 90.92° C and a standard deviation of 7.90° C. The corresponding +3σ value is 114.61° C, which is well below the maximum temperature constraint of 250° C.

4.6.2 Additional Selection Criteria

Overall, Layups 1-4 had a peak bondline temperature distribution +3σ value far below the maximum temperature constraint of 250° C. This means that all four three-layer dual insulator configurations are potentially viable for the nominal HULA mission. Other important characteristics, such as insulation mass and thickness, need to be considered in the selection process as well.

One layer of KFA5 has a thickness of 0.242 inches and an areal mass of 0.559 (kg/m^2). Four layers of Saffil have a combined thickness of 0.1792 inches and an areal mass (mass per unit area) of 0.6 (kg/m^2). As an initial comparison, one layer of KFA5 is 35% thicker than one grouped layer of Saffil (four layers of Saffil). Conversely, one grouped layer of Saffil is 7% more massive than one KFA5 layer.

The thickness and areal mass of Layup 1 are 0.73 inches and 1.68 (kg/m^2), respectively. The remaining layups (Layups 2, 3, and 4) have the same thickness and areal mass of 0.6 inches and 1.76 (kg/m^2), respectively. Overall, Layup 1 is 21% thicker and only 5% less massive than Layups 2, 3, and 4.

4.6.3 Dual-Insulator Configurations - Final Design Alternatives for HULA

When it comes to designing FTPS heatshields, the first priority is to keep the maximium bondline temperature under its maximum temperature constraint. However, thickness and mass are not equal priorities. FTPS is unique because it must be flexible and foldable without losing performance. Therefore, foldability is a crucial characteristic that must be prioritized, and thinner layups are preferred for better foldability. Another significant difference is that mass is no longer directly coupled to thickness. Because multiple

materials can be used in the FTPS layup, the total mass depends on the average thickness and density of all layup materials. Mass, or areal mass, must now be considered independently from thickness for each individual configuration.

Table 9: FTPS Design Methodology Summary Three-Layer Insulation Stacks

Layup #	+3σ Peak Bond TC (°C)	Thickness (in)	Areal Mass (kg/m²)	Suggested Ranking
Layup 1	92.21	0.73	1.68	3
Layup 2	100.27	0.6	1.76	1
Layup 3	106.10	0.6	1.76	2
Layup 4	114.61	0.6	1.76	4

The FTPS ranking shown in Table 9 helps the analyst make recommendations for the final insulator design for a nominal HULA mission. All layups meet the first priority by yielding bondline temperatures well under the maximum constraint of 250° C. Layup 1 was the best performer with a peak bondline temperature +3σ value of 92.21° C. The next best performer was Layup 2 with a peak bondline temperature +3σ value of 100.27° C, which is approximately 8.7% higher than Layup 1. Layup 3 and Layup 4 followed in performance with peak bondline temperature +3σ values of 106.10° C and 114.61° C, respectively, which were approximately 15.06% and 24.29% higher than Layup 1, respectively. The second priority is to find the thinnest insulator stack. Layups 2, 3, and 4 are approximately 21% thinner than Layup 1, making them clearly better than Layup 1 from this perspective. Finally, the third priority is to find the least massive configuration. Layup 1 is favored here by being approximately 5% less massive than Layups 2, 3, and 4.

An initial comparison will be drawn between Layup 1 and Layup 2. Layup 1 outperforms Layup 2 by producing a peak bondline temperature that is 8.7% lower and is also 5% less massive. This comes at the expense of thickness as Layup 2 is 21% thinner than Layup 1. Because thickness is such an important characteristic for FTPS to maintain

foldability, it becomes the deciding factor here, making Layup 2 the better overall dual-insulator design for a nominal HULA mission.

A similar comparison can be drawn between Layup 1 and Layup 3. Layup 1 outperforms Layup 3 by producing a peak bondline temperature that is 15.06% lower while the same thickness and mass comparisons stand from the previous example. Again, because thickness is such an important factor, Layup 3 is a more attractive overall option than Layup 1. Finally, Layup 1 outperforms Layup 4 by producing a peak bondline temperature that is 24.29% lower. The temperature difference is now significant enough to warrant a 21% thicker design, leaving Layup 1 more attractive than Layup 4.

By considering the peak bondline temperature, thickness, and areal mass, the proposed FTPS dual-insulator design methodology selects Layup 2 (Figure 84) and Layup 3 (Figure 87) as final design alternatives for a nominal HULA mission. As such, the methodology recommends further arc-jet testing for these configurations at flight-relevant conditions to select the final insulator configuration.

As mentioned, all layups in this analysis had peak bondline temperature $+3\sigma$ values well below the maximum temperature constraint of 250° C. While this is a desirable result, it also suggests that layups thinner than three-layers could possibly be used to satisfy mission requirements. The following section evaluates performance of insulation stacks that are thinner than the three-layer configurations presented in this section.

4.7 FTPS Design Demonstration for HULA Using Thinner Insulation Stacks

The previous section showed that three-layer dual-insulator configurations produced peak bondline temperature $+3\sigma$ values less than 115° C. This is significantly lower than the maximum temperature constraint of 250° C. Previous discussion highlighted the importance of minimizing thickness for FTPS layups to maximize heatshield foldability. To this end, it is beneficial for the designer to investigate insulation stack options thinner than three-layers. The following sections will evaluate performance of two two-layer dual-insulator configurations along with two single-layer insulation configurations. A DOE was

not needed to select these thinner configurations because there are not many combinations to evaluate. Nevertheless, the evaluation technique will follow the same rigor as the previous section.

4.7.1 Thinner Configurations – Probability of Success

Four insulator configurations thinner than three-layers were evaluated to compare performance for an upcoming HULA mission. These configurations are referred to as Layup 5, Layup 6, Layup 7, and Layup 8. The following discussion will introduce each layup, briefly discuss performance metrics for each layup, and then summarize performance comparisons. As mentioned, performance comparisons are centered around the bondline thermocouple located between the last insulation layer and the gas barrier.
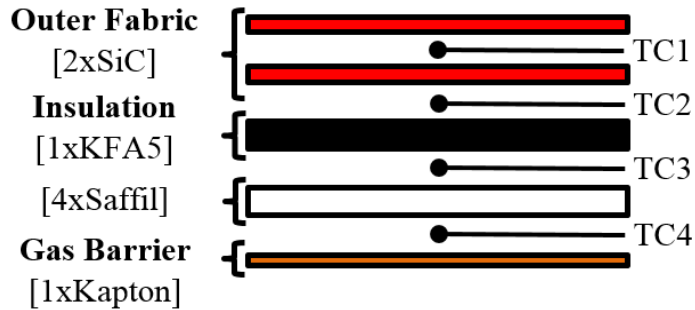
Figure 93: FTPS Thinner Configuration Design Layup 5

A detailed schematic of Layup 5 is shown in Figure 93. The outer fabric region is composed of 2 layers of SiC fabric and the gas barrier is composed of 1 layer of Kapton. The insulation region is composed of one top layer of KFA5 and one bottom layer grouping of Saffil, which is abbreviated by using the identifier "KS" (KFA5/Saffil). Numbered thermocouple locations are shown between each FTPS layer with focused placed on the TC4 bondline temperature. Bondline temperature predictions for Layup 5 are shown in Figure 94 for all dispersed trajectories. The nominal prediction is shown as a thick, black line while approximated +3σ and -3σ temperature profiles are shown as a red-dashed line and a blue-dashed line, respectively. Finally, the complete set of bondline temperature

136

predictions are shown as thin, green lines. Figure 95 is a histogram of peak bondline temperatures for each trajectory case that is normally distributed.

Figure 94: Layup 5 Bondline Monte Carlo Temperature Predictions
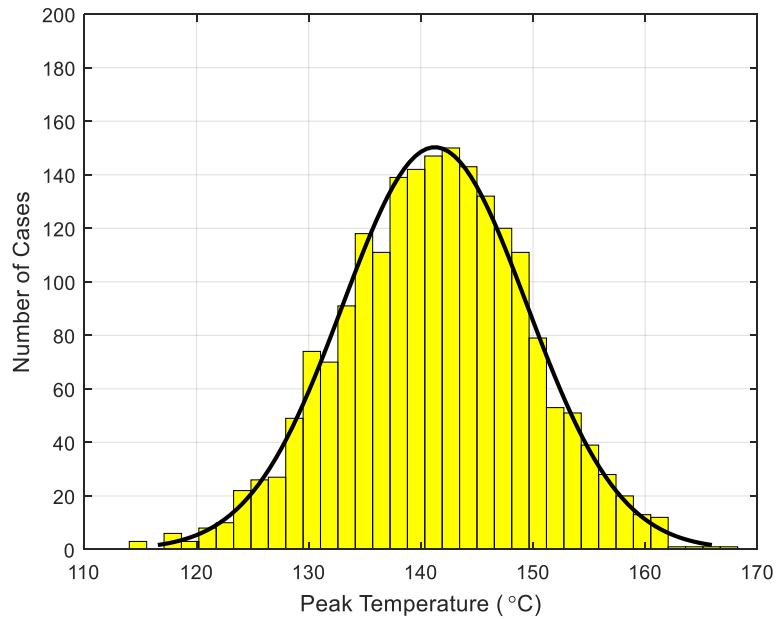
Figure 95: Layup 5 Peak Bondline Temperature Distribution

The bondline temperature profiles for Layup 5 shown in Figure 94 have the widest uncertainty bounds near nominal peak temperature around 125 seconds. The peak bondline temperature distribution shown in Figure 95 has a mean of 141.25° C and a standard deviation of 8.23° C. The corresponding +3σ value is 165.95° C, which is still well below the maximum temperature constraint of 250° C.
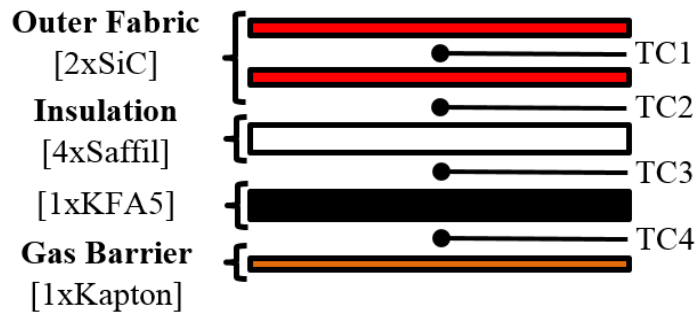
Figure 96: FTPS Thinner Configuration Design Layup 6

A detailed schematic of Layup 6 is shown in Figure 96. For Layup 6, the insulation region is composed of one top layer grouping of Saffil followed by one layer of KFA5, which is represented with the identifier "SK" (Saffil/KFA5). Bondline temperature predictions for Layup 6 are shown in Figure 97 for all dispersed trajectories. A normally distributed histogram of peak bondline temperatures for Layup 6 is shown in Figure 98.
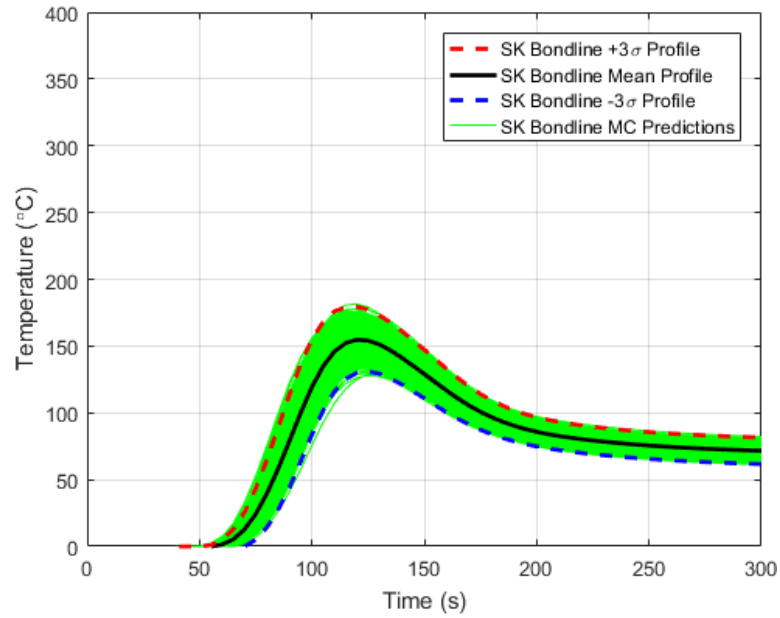
Figure 97: Layup 6 Bondline Monte Carlo Temperature Predictions
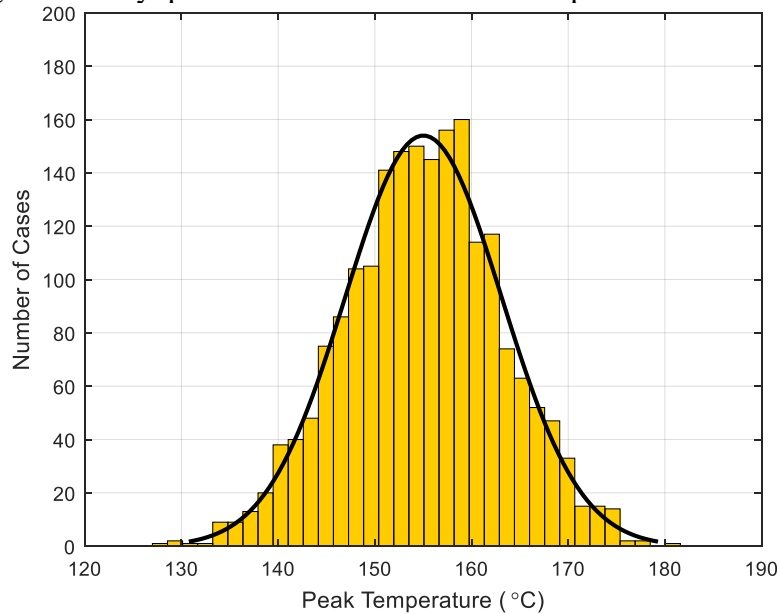
Figure 98: Layup 6 Peak Bondline Temperature Distribution

The bondline temperature profiles for Layup 6 shown in Figure 97 have the widest uncertainty bounds near nominal peak temperature just before 125 seconds. The peak bondline temperature distribution shown in Figure 98 has a mean of 155.03° C and a standard deviation of 8.09° C. The corresponding +3σ value is 179.28° C, which is still well below the maximum temperature constraint of 250° C.
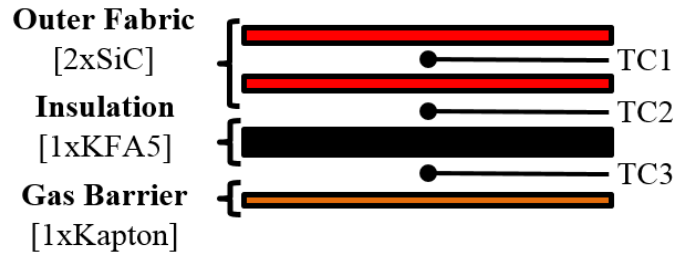
Figure 99: FTPS Thinner Configuration Design Layup 7

A detailed schematic of Layup 7 is shown in Figure 99. For Layup 7, the insulation region is composed of only one layer of KFA5, which is represented with the identifier "K" (only KFA5). Bondline temperature predictions for Layup 7 are shown in Figure 100 for all dispersed trajectories. A normally distributed histogram of peak bondline temperatures for Layup 7 is shown in Figure 101.
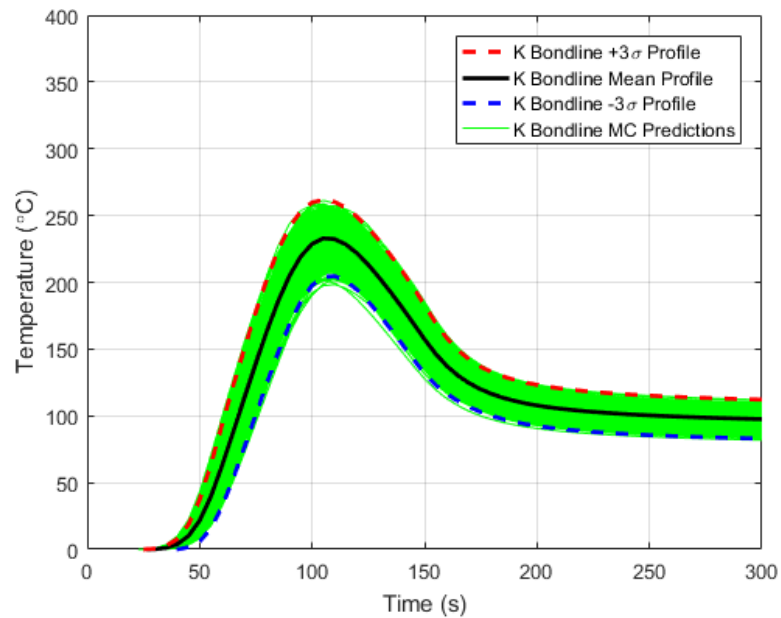
Figure 100: Layup 7 Bondline Monte Carlo Temperature Predictions
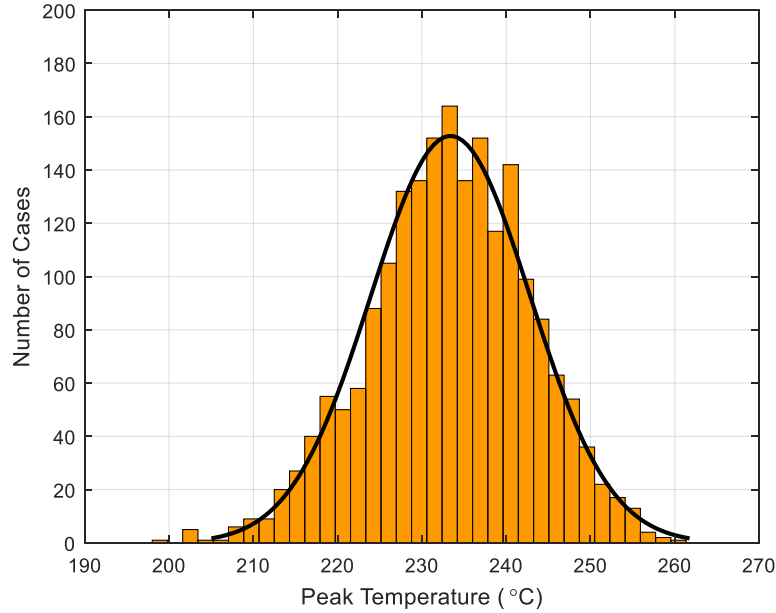
Figure 101: Layup 7 Peak Bondline Temperature Distribution

The bondline temperature profiles for Layup 7 shown in Figure 100 have the widest uncertainty bounds near nominal peak temperature just after 100 seconds. The peak bondline temperature distribution shown in Figure 101 has a mean of 233.39° C and a standard deviation of 9.46° C. The corresponding +3σ value is 261.76° C, which is above the maximum temperature constraint of 250° C.
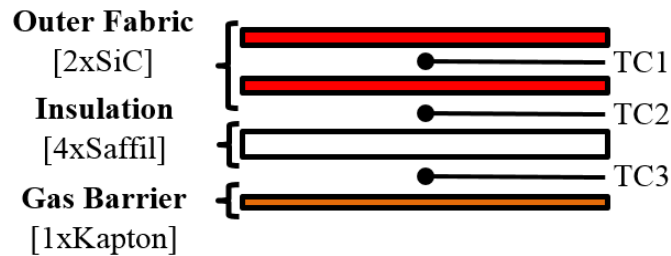
Figure 102: FTPS Thinner Configuration Design Layup 8

A detailed schematic of Layup 8 is shown in Figure 102. For Layup 8, the insulation region is composed of only one grouping layer of Saffil, which is represented with the identifier "S" (only Saffil). Bondline temperature predictions for Layup 8 are shown in

141

Figure 103 for all dispersed trajectories. A normally distributed histogram of peak bondline temperatures for Layup 8 is shown in Figure 104.
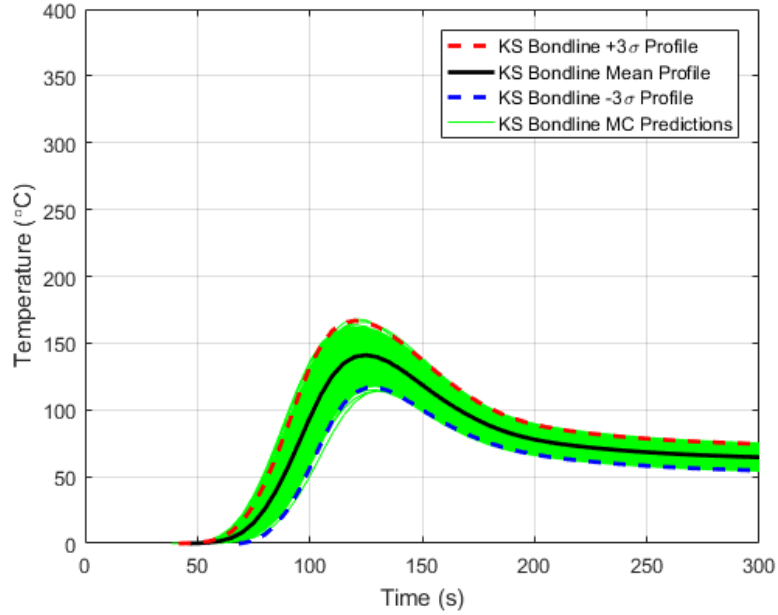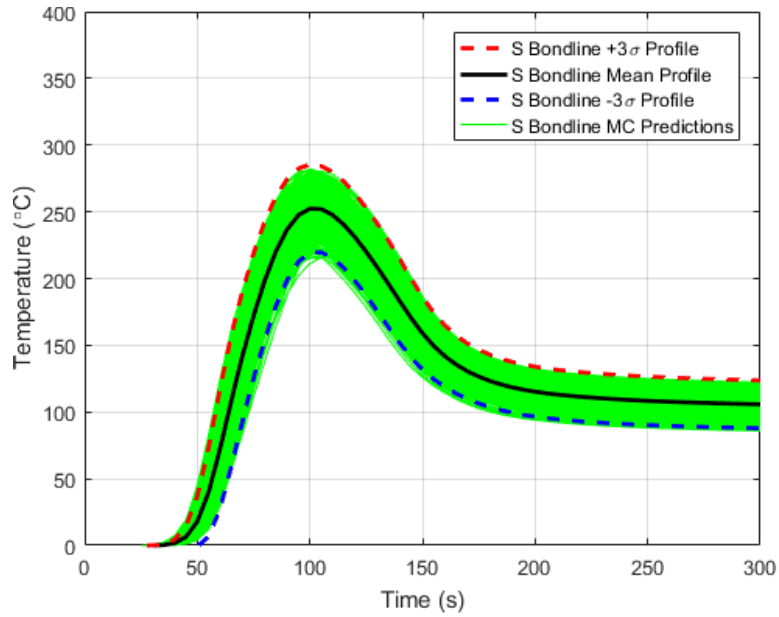

Figure 103: Layup 8 Bondline Monte Carlo Temperature Predictions
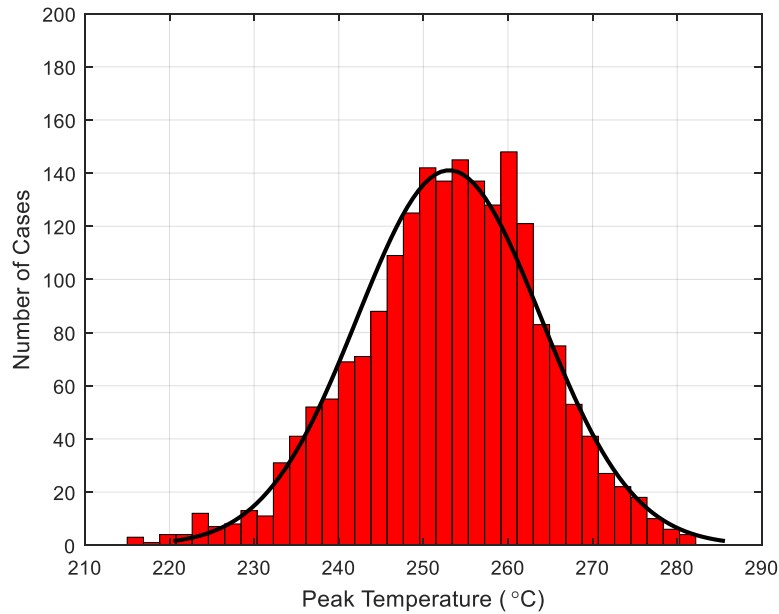
Figure 104: Layup 8 Peak Bondline Temperature Distribution

The bondline temperature profiles for Layup 8 shown in Figure 103 have the widest uncertainty bounds near nominal peak temperature at around 100 seconds. The peak

bondline temperature distribution shown in Figure 104 has a mean of 253.05° C and a standard deviation of 10.87° C. The corresponding +3σ value is 285.65° C, which is above the maximum temperature constraint of 250° C. Layup 8 yields the highest peak bondline temperature +3σ value out of all previous layups.

4.7.2 Additional Selection Criteria

To perform an accurate evaluation of Layups 5-8, it is important to consider the top three priorities for FTPS heatshields mentioned earlier, including peak bondline temperature, thickness, and areal mass.

Layup 5 and Layup 6 have the same thickness and areal mass of 0.42 inches and 1.16 (kg/m^2), respectively. Layup 7 has a thickness of 0.242 inches and an areal mass of 0.559 (kg/m^2). Additionally, Layup 8 has a thickness of 0.179 inches and an areal mass of 0.6 (kg/m^2). Because Layup 5 and Layup 6 have the same thickness and areal mass, they will be compared by peak bondline temperature performance. However, Layup 7 is 35% thicker and only 7% less massive than Layups 8.

4.7.3 Feasibility of Thinner Configurations for HULA Nominal Mission

The FTPS priority ranking helps the analyst make useful comparisons for thinner insulator configurations a nominal HULA mission. Only two layups meet the first priority by yielding bondline temperatures under the maximum constraint of 250° C. The following discussion will compare Layups 5-8 to metrics from Layup 1 (3 Layers of KFA5) for consistency. Key discussion points are shown in Table 10.

Table 10: FTPS Design Methodology Summary Thinner Insulation Stacks

Layup #	+3σ Peak Bond TC (°C)	Thickness (in)	Areal Mass (kg/m^2)	Suggested Ranking
Layup 5	169.95	0.42	1.16	1
Layup 6	179.28	0.42	1.16	2
Layup 7	261.76	0.242	0.559	NF
Layup 8	285.65	0.179	0.6	NF

Layup 5 was the best performer with a peak bondline temperature $+3\sigma$ value of $165.95°$ C, which is approximately 80% higher than Layup 1. The next best performer was Layup 6 with a peak bondline temperature $+3\sigma$ value of $179.28°$ C, which is approximately 94.43% higher than Layup 1. Layup 7 and Layup 8 followed in performance with peak bondline temperature $+3\sigma$ values of $261.76°$ C and $285.65°$ C, respectively, which were approximately 284% and 310% higher than Layup 1, respectively. However, these peak bondline temperature $+3\sigma$ values exceed the maximum temperature constraint of $250°$ C. As such, Layup 7 and Layup 8 are designated as Not Feasible (NF) in Table 10 and eliminated from consideration.

The second and third priorities are to find the thinnest and least massive insulator stacks, respectively. Layup 5 and Layup 6 both have the same thickness and areal weight, which are approximately 73% thinner and 45% less massive than Layup 1, respectively. Overall, the ranking for feasible insulator configurations thinner than three layers must be decided by peak bondline temperature $+3\sigma$ values. As such, Layup 5 is ranked above Layup 6 for having a peak bondline temperature $+3\sigma$ value that is approximately $10°$ C lower. To summarize, the most attractive insulator configurations thinner than three-layers are Layup 5 followed by Layup 6. Layup 7 and Layup 8 were eliminated for exceeding the maximum peak bondline temperature constraint of $250°$ C.

4.8 Summary

A rigorous ground-test based FTPS design process has been executed over the past decade to achieve a feasible insulator stackup configuration for a HIAD atmospheric entry mission. Although extensive arc-jet testing can eventually find the best insulator configuration for a nominal atmospheric entry mission, it requires a great deal of resources. To advance the state-of-the-art in FTPS design and conserve experimental resources, a simulation-based design process has been proposed to efficiently obtain final FTPS dual-insulator design configurations that are feasible for a nominal Earth-entry mission.

The proposed design methodology uses information from a nominal mission profile along with insulator material properties to construct various thermal response models. Pre-selected insulators are ground-tested sparingly in combined configurations to enable thermal response model verification and validation. Defining performance characteristics allows for the evaluation of mission-relevant candidate insulators with the highest probability of success. FTPS thermal response models of multiple configurations were evaluated to determine which designs meet mission requirements. Because the design process relies heavily on thermal model simulations, the final FTPS designs are obtained by using minimal ground testing.

The most critical performance characteristic was the $+3\sigma$ peak bondline temperature value for Layups 1-8, where lower temperatures were more desirable. To be considered feasible for the presented HULA mission, layups could not exceed a maximum $+3\sigma$ peak bondline temperature constraint of 250 ° C. Figure 105 shows peak bondline temperature distributions for Layups 1-8 on the same plot. Layups 1-6 have $+3\sigma$ peak bondline temperature values in the feasible region. Layups 7-8 have $+3\sigma$ peak bondline temperature values exceeding the 250 ° C constraint, and therefore, are considered **infeasible** designs.
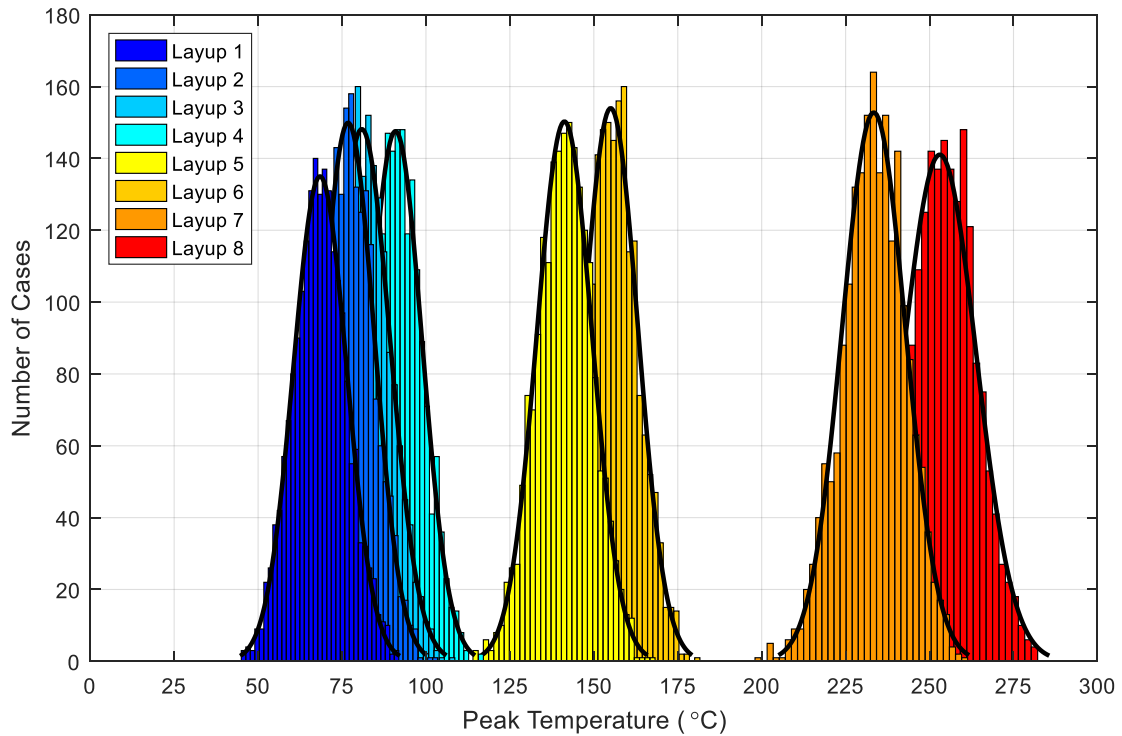
Figure 105: Peak Bondline Temperature Distributions for Layups 1-8

Insulator configurations for Layups 1-4 were obtained by using a $L_4(2^3)$ Taguchi orthogonal array (Configurations 1-4) to efficiently explore the three-layer insulator design space. One additional benefit of using a Taguchi array allows the designer to infer results for designs that were left out of the array (Configurations 5-8). Based on the results shown for Layups 1-4 (Configurations 1-4) in Figure 105, one can see that configurations with KFA5 insulator layers closer to the surface of the sample result in lower peak bondline temperatures. Using this information, one could infer that the best performing insulator design among untested Configurations 5-8 would be Configuration 8 because its first two layers are KFA5. Configuration 7, Configuration 6, and Configuration 5 would follow in order of best to worst performers by observing how close KFA5 layers are to the top of the insulator stack.

Performance characteristics used to evaluate Layups 1-8 included $+3\sigma$ peak bondline temperature, thickness, and areal weight. Figure 106 illustrates these performance

metrics for Layups 1-8 in one succinct chart. After acknowledging that Layups 7-8 exceed the maximum +3σ peak bondline temperature constraint and are infeasible, one can use this chart to compare performance metrics for remaining feasible layups. The two-layer insulator designs (Layups 5-6) meet the temperature constraint with relatively low thickness and areal weight. The three-layer insulator designs do produce significantly lower peak bondline temperatures, but their relatively large thickness and areal weight metrics make them less attractive for the HULA mission.
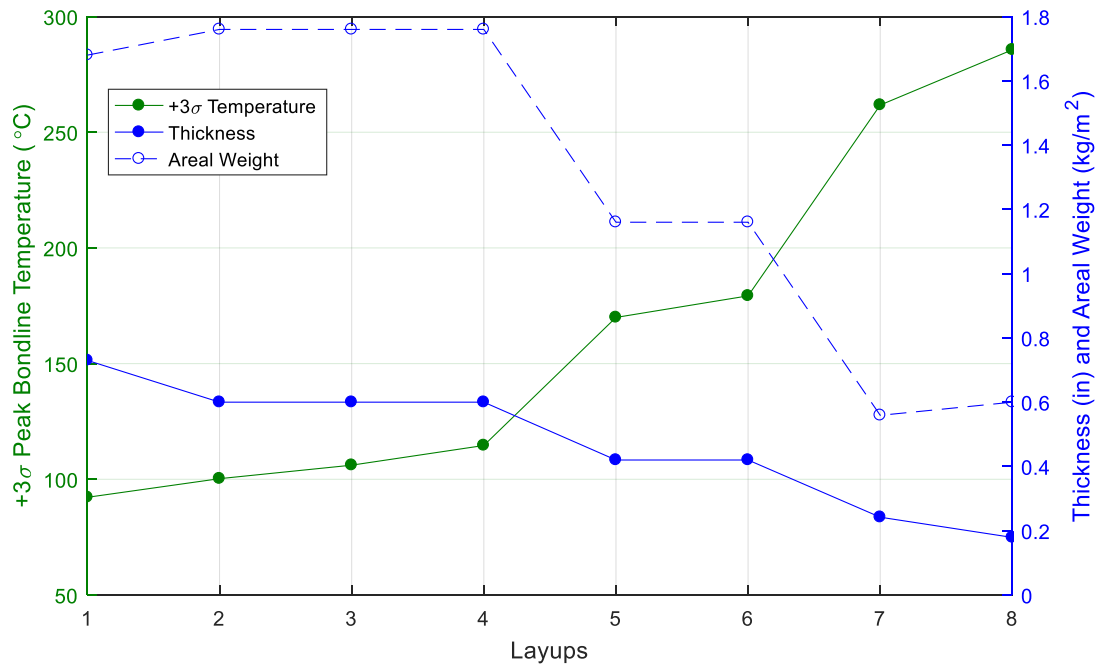
Figure 106: Figures of Merit for Layups 1-8 including +3σ Peak Bondline Temperature, Thickness, and Areal Weight

In this instance, it is not advantageous to present this information as a 2D Pareto frontier or a 3D Pareto surface because there are only two solution types, two-layer and three-layer insulator designs. The result would show only two non-dominated solutions, resulting in trivial line or plane for a Pareto frontier or surface, respectively. In this case, Figure 106 is a more direct approach that allows simpler decision-making between two-layer and three-layer insulator configuration. If the designer uses the FTPS dual-insulator design

methodology for an application that investigates many more than two solution types, it becomes more advantageous to present layup performance information in the form of a Pareto surface.

It should be noted that the main purpose of performing the FTPS dual-insulator design methodology is not necessarily to come up with a final answer for the best layup. The main objective is to provide mission-specific design information that greatly reduces follow-on experimental effort to determine the "best" layup. For the HULA mission, the FTPS team was initially determined to embark on an extensive arc-jet testing campaign to find the best three-layer insulator design configuration. The presented FTPS dual-insulator design methodology showed that two-layer insulator design configurations are feasible and advantageous. It also showed that layups tend to produce lower $+3\sigma$ peak bondline temperatures when KFA5 layers are located closer to the top of the insulation stack. Ideally, the FTPS team would then use this information to plan a final arc-jet test campaign considering two-layer insulator configurations and three-layer insulator configurations with KFA5 layers near the top of the stack. In this regard, using this simulation-based decision-making methodology provides significant benefits over the original, ad-hoc ground-based testing decision-making process. Using the FTPS dual-insulator design methodology allows the designer to use simulation-based decision making to obtain a final insulator configuration, tailored to a specific nominal mission, with significant savings in experimental effort.

This design process can be readily extended beyond the application of an FTPS heatshield. Applications ranging from emergency fire shelters to spacecraft insulation can make use of this simulation-based insulator screening and design methodology to efficiently explore an insulator stack configuration design space. Suggestions for future work will provide the reader with a framework to generalize the proposed FTPS design methodology to accommodate a larger number of insulator stackup configurations for wide-ranging applications.

CHAPTER V

SUMMARY AND FUTURE WORK

This dissertation presents multiple methodologies to streamline the FTPS thermal response modeling and design process for a HIAD atmospheric entry mission. Each novel methodology presented in this dissertation extends rigid, ablative TPS thermal modeling and design methods to accommodate the unique, multi-layered, multi-material nature of FTPS. These methods take a probabilistic approach to verifying and validating FTPS thermal response models, experimentally determining FTPS material properties, and designing the best-performing dual-insulator material combinations. This dissertation advances the state-of-the-art of conceptual thermal response modeling, testing, and design of FTPS.

5.1 Summary

This investigation presents three methodologies to overhaul and streamline the FTPS modeling and design process. The first methodology extended an existing inverse multi-parameter estimation methodology to improve FTPS thermal response model temperature prediction accuracy. Mahzari's previously developed methodology was specifically designed to improve rigid-ablative TPS thermal response models. This investigation bridges the gap between traditional and non-traditional thermal response model improvement correlation by extending methods used for rigid-ablators to FTPS. The second methodology presented further improves FTPS thermal predictions by experimentally determining the activation energy of decomposing insulators using TGA. Previous FTPS thermal response models did not describe decomposition with experimentally derived quantities, leaving uncertainty in this governing parameter. In this investigation, the activation energy distribution is obtained experimentally and efficiently.

After the FTPS thermal response models were verified and validated, a combined dual-insulator FTPS thermal response model was utilized to design the best-performing dual-insulator stackup for a HIAD Earth-entry mission.

Chapter 1 motivated this investigation by performing background research and showing gaps in the literature where work was needed to accomplish near-term goals. Specifically, a new HIAD concept has been gaining traction as a means of delivering high-mass payloads to the surface of Mars. Because the aeroshell inflates around the rigid payload, the FTPS heatshield protecting the aeroshell from atmospheric entry heating must be flexible, which is unlike rigid-ablative TPS designed in the past. The Chapter 1 literature search demonstrated that although advancements have been made in rigid-ablative TPS thermal response modeling, these techniques had yet to be developed for heterogeneous material stacks like those found in FTPS.

Chapter 2 used concepts from probabilistic analysis to develop a Monte Carlo simulation around an FTPS thermal response model to characterize input parameter uncertainties. In the past, thermal analysts painstakingly correlated FTPS models manually adjusting one thermal parameter at a time until simulation predictions match experimental results. In this investigation, methods from inverse heat transfer analysis and parameter estimation are applied to obtain more accurate simulation predictions. An extended inverse multi-parameter estimation methodology developed specifically for FTPS materials identified the most significant input parameter contributors to temperature response uncertainty, the linear correlation between these significant contributors, and input parameter estimates that minimize error between FTPS temperature predictions and experimental measurements.

Chapter 3 completed a thermogravimetric (TGA) testing campaign to obtain the activation energy for two FTPS fibrous insulators. Standard and Modulated TGA methods were used to characterize the decomposition of both insulators. For each insulator, the resulting activation energies from both TGA methods were compared, showing reasonable

agreement. After making a common assumption that activation energy is normally distributed, a novel material testing methodology was developed to estimate its standard deviation uncertainty with repeated experiments. This methodology reduces the parametric uncertainty for input parameters and can be used for many material properties. These activation energies were inserted into FTPS thermal response models to refine simulated insulator mass decomposition expressions. Not only does this information help analysts simulate insulator mass decomposition more accurately, it allowed the sensitivity of activation energy to be investigated using the extended inverse multi-parameter estimation methodology.

Chapter 4 demonstrated a simulation-based FTPS insulator design methodology developed to efficiently obtain a final dual-insulator configuration for a nominal atmospheric-entry mission. The FTPS dual-insulator design process began with two attractive insulators that had not been ground-tested together in a dual-insulator configuration. The extended inverse multi-parameter estimation methodology uses minimal arc-jet ground testing to verify and validate FTPS thermal response models each containing a multi-layered insulation stack composed of only one insulation material type. The first FTPS thermal response model insulation stack was composed of purely KFA5 layers and the second was composed of only Saffil layers. Once both thermal response models were verified and validated independently, a dual-insulator thermal response model was created to evaluate peak bondline temperature performance. Rather than evaluating every possible dual-insulator combination, a Design of Experiments (DOE) technique was used to filter out similar dual-insulator designs and eliminate redundancy. Only dual-insulator designs that are significantly different, prescribed by the selected DOE, were evaluated to ensure efficient exploration of the dual-insulator configuration design space. The final output of this methodology provided a probabilistic evaluation of dual-insulator design peak bondline temperature distributions under mission-relevant conditions. Final dual-insulator configurations were selected to inform further arc-jet ground-testing.

5.2 Suggestions for Future Development of Extended Inverse Methodology

A Thermocouple (TC) Driver approach was used to drive the FTPS thermal response models of arc-jet ground tests, meaning the boundary condition was defined to be a transient temperature profile measured by a thermocouple embedded between FTPS layers during the arc-jet test. The TC driver approach was used for two reasons, to focus on the insulator thermal-material response problem and to use a well-known, measured boundary condition.

The inverse multi-parameter estimation methodology presented here focused on solving the FTPS insulator thermal-material response problem, and for this reason, the selected driving thermocouple sat between the last outer fabric layer and the first insulation layer. All thermocouples that were physically touching insulation were predicted and improved for the insulation stack within the FTPS thermal response model. Because this dissertation is primarily focused on improving modeling and design methods of only FTPS insulation, it is appropriate to drive the thermal response model with temperature data located closest to the first layer of insulation and improve prediction accuracy for deeper insulation layers.

Another reason the TC Driver approach proved beneficial was because the Boeing LCAT arc-jet boundary conditions were not well-known at the time of the analysis. The boundary conditions on the surface of the FTPS sample cannot be measured directly without effecting the flow around the layup. Detailed CFD must be performed to estimate heating conditions on the surface of arc-jet samples. At the time of this investigation, the only available boundary condition data was not based on relevant CFD and contained significant uncertainty bounds. Large uncertainties from experimental arc-jet boundary conditions cause in-depth temperature predictions to vary widely, making it very difficult to gain accurate estimates of each parameter's contribution to temperature prediction uncertainty. Added challenges are experience during inverse multi-parameter estimation

152

because large boundary condition uncertainties overshadow parameter uncertainties, making it difficult to obtain realistic parameter estimates to reduce temperature prediction error.

However, if arc-jet boundary conditions derived from high-fidelity CFD are readily available, one can modify the presented extended inverse multi-parameter estimation methodology to include them. Additionally, aerothermal properties derived from these boundary conditions can be considered and estimated with the improved method. Mahzari included aerothermal properties in his inverse multi-parameter estimation methodology used for a rigid-ablative TPS because he had access to validated boundary conditions for arc-jet testing and a simpler material response problem to solve. As an item of future development, the analyst can use well-defined LCAT arc-jet aerothermal boundary conditions at the surface of the FTPS layup in the thermal response model. Boundary conditions of interest in this situation include surface heat flux, surface pressure, and surface catalysis processes. Depending on how the boundary condition estimation analysis was completed, one could define the uncertainties of key aerothermal input parameters and integrate them into the extended inverse multi-parameter estimation methodology presented herein.

Accurate measurement of thermal-material properties is notoriously difficult. Further, if a thermal-material property is a function of temperature, experimental measurements may be more accurate at lower temperatures and less accurate at higher temperatures. The extended inverse multi-parameter estimation methodology presented in this work estimates thermal-material parameters with scalar multipliers. For thermal-material properties that are functions of temperature, multiplying by a scalar value does not change the underlying functional form. To increase the fidelity of the presented methodology, one can consider the temperature dependency of some thermal-material properties and estimate the entire temperature-dependent function. Doing so would require significant development beyond the current method because the problem would now be

characterized as functional estimation rather than parameter estimation. New algorithms would need to be added to the method for functional estimation. While this adds another level of analysis complexity, it would provide more capability by only adjusting portions of the thermal-material property functions that are less accurate, which can make the thermal response model validation effort more effective.

The uncertainty analysis presented in Chapter 2 shows the reader that the influence of FTPS thermal-material properties varies with time during ground-testing. The current methodology performs nominal analysis by only considering the time region between FTPS model injection and model extraction from the arc-jet flow. While this allows for treatment of the experimental region, it forces the analyst to average top-contributing thermal-material properties over the duration of the experiment. Instead, the total experimental time could be broken into smaller segments. The methodology can be performed for each of these smaller segments in time and results can be pieced together. Essentially, this would allow the analyst to adjust mid-test behavioral anomalies with more rigor, potentially leading to a more accurate thermal response model. Another area of improvement includes more rigorous treatment of the thermocouple sensor data recorded from arc-jet experiments. One of the reasons thermocouple data is treated as "truth" is because the analysis team does not have a proven method to estimate the bias of thermocouple temperature measurements. If a reliable method is executed to yield accurate estimates for thermocouple measurement bias, it can be considered in the extended inverse multi-parameter estimation methodology.

The presented extended inverse multi-parameter estimation methodology verifies and validates FTPS thermal response models using experimental data from one corresponding arc-jet ground-test. While this is sufficient to perform nominal, uncertainty, sensitivity, and inverse analyses, the final estimated properties may be biased by run-specific behavior. To reduce this type of bias, solutions for multiple arc-jet test runs could be computed for the same FTPS layup. Ideally, inverse analysis would be performed on

the same parameters for each FTPS thermal response model of the same layup. If final estimated parameters differ in value for each run, a method can be developed to integrate parameter estimates across different runs to find the "best" parameter estimates for all runs analyzed. Showing strong temperature prediction agreement for multiple runs would provide more confidence in the thermal response model physics and the estimated parameter values.

An effort is currently underway at NASA Langley Research Center to create a 2D FTPS thermal response model simulating depth and horizontal distance between the layup centerline and its outer diameter. The presented inverse multi-parameter estimation methodology can be extended further by analyzing multiple points between the centerline and the outer diameter of the arc-jet tested FTPS layup. After performing inverse analysis at each point between the centerline and outer-collar, one can determine reasonable scale factor values that improve temperature predictions and show agreement between locations. This would require recording thermocouple data at all off-axis locations within layups. Finally, during inverse analysis, one could add logic to penalize significant movement away from nominal scale factor values.

5.3 Suggestions for Future Development of Material Testing Methodology

One suggested improvement to the material property experimental uncertainty quantification methodology includes extending the method to quantify the probabilistic uncertainty of other normally distributed thermal-material properties. In this dissertation, a methodology was presented to experimentally estimate the standard deviation of the activation energy distribution. This methodology can be readily extended to obtain the uncertainty of other thermal-material properties, as long as the following requirements are met. First, the thermal-material property in question must be normally distributed. Second, one must have the resources to perform experimental repetitions to obtain statistical information about thermal-material property measurements. Lastly, one must be able to

155

approximate the thermal-material distribution with a student's t-distribution. The more repetitions that are performed, the closer the resulting t-distribution approximates a normal distribution.

TGA testing of a multi-constituent felt with multiple reactions is feasible by following appropriate ASTM standards mentioned in this work. If associated analyses are performed correctly to obtain estimates for activation energy, one could extend the presented material property experimental uncertainty quantification methodology to approximate desired activation energy distributions.

One limitation of the Standard TGA method is the maximum heating rate of 10 C/min specified by ASTM standards in order to obtain an experimental estimation of activation energy. While this is sufficient for obtaining one estimate of activation energy, a heating rate of 10 C/min is approximately an order of magnitude smaller than the heating rate experienced during atmospheric entry. At such high heating rates, the activation energy may be different. For this reason, it is worth the effort to experimentally determine the activation energy at flight-relevant heating rates.

5.4 Suggestions for Future Development of FTPS Design Methodology

The presented FTPS dual-insulator design methodology can be readily extended to consider a wider range of options. First, more than two insulators can be considered in the insulation stack for a nominal mission. This methodology only requires that the analyst has at least one flight-relevant arc-jet ground test with a pure insulation stack of each option. In fact, the more insulators that are considered, the more benefit one receives from using a DOE to reduce the set of layups that are actually evaluated with thermal response models. Second, one can consider a nominal mission for other atmospheric bodies such as Mars or Titan. Third, one can consider designing the FTPS multi-insulation stack for three different types of atmospheric entries, including ballistic, lifting and aerocapture trajectories. As a

final suggestion, the interested designer can apply this methodology to any multi-layered, multi-material heatshield beyond the FTPS application.

APPENDIX A

DETERMINATION OF CONSTANT CONVERSION REGION

When calculating activation energy with Standard TGA experimentation using ASTM Standard Test Method E1641-15, one must define a specific weight loss remaining percentage where the decomposition event occurs. It is desirable for this decomposition event to align with the region of constant conversion, which is where decomposition progresses at a constant rate. One can calculate activation energy at multiple conversion percentage values to find the region of constant conversion. Figure 107 and Figure 108 provide an example for define the weight loss remaining percentage where the decomposition event occurs for KFA5 carbon felt.
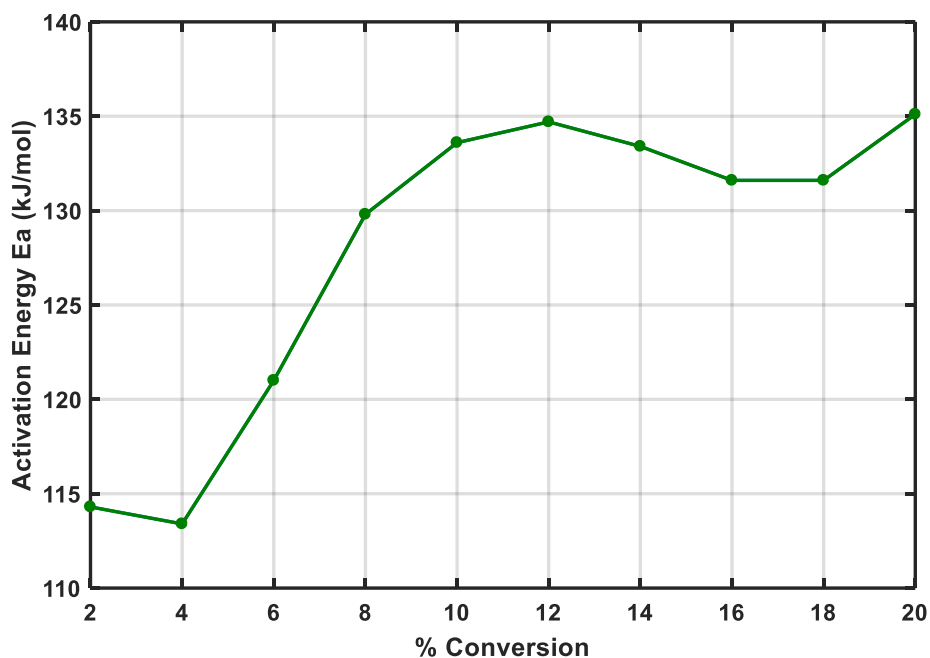
Figure 107: Determination of KFA5 Region of Constant Conversion
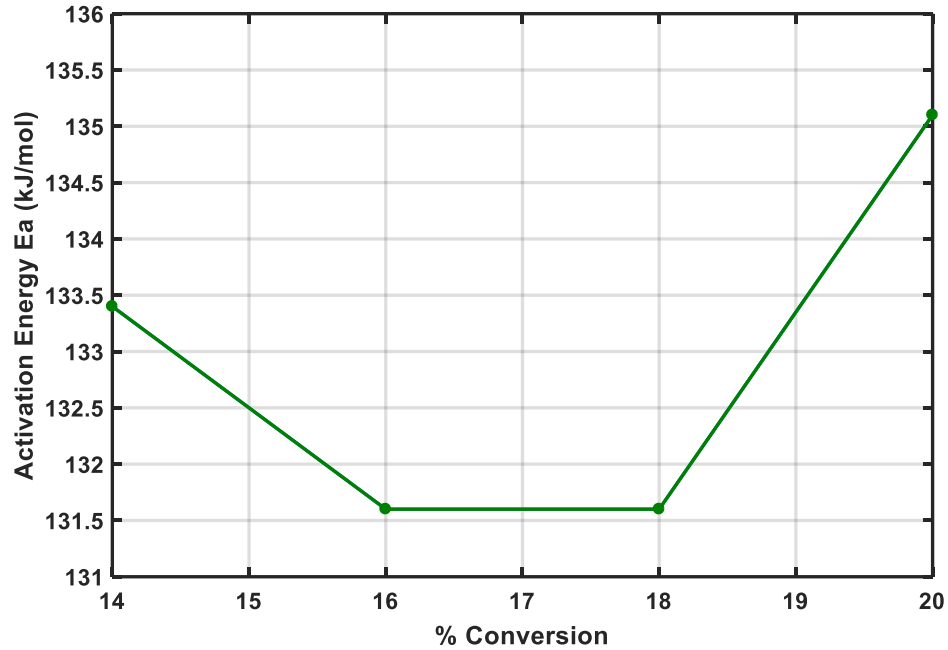
Figure 108: Determination of KFA5 Region of Constant Conversion – Zoomed In

Figure 107 shows a series of activation energy calculations between 2% conversion (98% weight loss remaining) and 20% conversion (80% weight loss remaining) in increments of 2%. Figure 108 zooms in on the region where the calculation of activation energy remains constant, between 16% conversion (84% weight loss remaining) and 18% conversion (82% weight loss remaining). Because this is a region of constant conversion, the decomposition event was defined to occur at 17% conversion, or 83% weight loss remaining. The resulting activation energy at 83% weight loss remaining is approximately 131.6 kJ/mol.

APPENDIX B

LIST OF PUBLICATIONS

A.1 Journal Articles

A.1.1 Published Journal Articles

1. **Rossman, G.**, LeVine, M., Lawlor, S., Sloss, T., Mishra, P., Tan, Z.P., and Braun R.D., "Conceptual Design of a Small Earth Reentry Vehicle for Biological Sample Return", *Journal of Spacecraft and Rockets*, Vol. 54, pp. 246-257, January, 2017.

A.1.2 Submitted Journal Articles

1. **Rossman, G.**, Braun, R.D., "Thermogravimetric Analysis of Carbon Felt Insulation for Thermal Response Modeling", *Journal of Spacecraft and Rockets*, Submitted in December 2017.

A.1.2 Planned Journal Articles

1. **Rossman, G.**, Dec, J.A., Braun, R.D., "Extended Inverse Multi-Paramter Estimation Methodology Flexible Thermal Protection Systems", *Journal of Spacecraft and Rockets*, (to be published).

2. **Rossman, G.**, Braun, R.D., "Dual-Insulator Design Methodology for Flexible Thermal Protection Systems", *Journal of Spacecraft and Rockets*, (to be published).

A.2 Conference Papers

A.2.1 Published Conference Papers

1. **Rossman, G.**, Dec, J.A., Braun, R.D., "Flexible Thermal Protection System Physics-Based Modeling for Temperature Profile Predictions", *AIAA Science and Technology Forum,* January 2014.

2. **Rossman, G.**, LeVine, M., Lawlor, S., Sloss, T., Mishra, P., Tan, Z.P., and Braun R.D., "BioDOME: Concept of an EDL System for Returning Small Biological Samples from LEO", *12th International Planetary Probe Workshop*, June 2015.

3. **Rossman, G.**, Braun, R.D., "Thermogravimetric Analysis of Flexible Thermal Protection Systems for Thermal Response Modeling", *AIAA Science and Technology Forum,* January 2016.

4. **Rossman, G.**, Braun, R.D., "Thermogravimetric Analysis of Carbon Felt Insulation for Flexible Thermal Protection System Thermal Response Modeling", *AIAA Science and Technology Forum,* January 2017.

5. Skolnik, N., Kamezawa, H., Li, L., **Rossman, G.**, Sforzo, B., and Braun, R.D., "Design of a Novel Hypersonic Inflatable Aerodynamic Decelerator for Mars Entry, Descent, and Landing", *AIAA Science and Technology Forum,* January 2017.

REFERENCES

[1] R. D. Braun and R. M. Manning, "Mars Exploration Entry, Descent, and Landing Challlenges", *Journal of Spacecraft and Rockets*, vol. 44, no. 2, pp. 310–323, Mar. 2007.

[2] S. J. Hughes, F. M. Cheatwood, R. A. Dillman, H. S. Wright, and J. A. DelCorso, "Hypersonic Inflatable Aerodynamic Decelerator (HIAD) Technology Development Overview," pp. 1–24, 21st AIAA Aerodynamic Decelerator Systems Technology Conference, May 2011, Dublin, Ireland, AIAA 2011-2524.

[3] Del Corso, W. E. Bruce, S. J. Hughes, J. A. Dec, M. D. Rezin, M. A. B. Meador, H. Guo, D. G. Fletcher, A. M. Calomino, and F. M. Cheatwood, "Flexible Thermal Protection System Development for Hypersonic Inflatable Aerodynamic Decelerators," pp. 1–11, 9th International Planetary Probe Workshop, June 2012, Toulouse, France.

[4] J. A. Del Corso, F. M. Cheatwood, W. E. Bruce III, and S. J. Hughes, "Advanced High-Temperature Flexible TPS for Inflatable Aerodynamic Decelerators," pp. 1–23, 21st AIAA Aerodynamic Decelerator Systems Technology Conference, May 2011, Dublin, Ireland, AIAA 2011-2510.

[5] J. R. Cruz and J. S. Lingard, "Aerodynamic Decelerators for Planetary Exploration: Past, Present, and Future," AIAA 2006-6792.

[6] D. K. Litton, D. M. Bose, F. M. Cheatwood, S. Hughes, H. S. Wright, M. C. Lindell, S. D. Derry, and A. Olds, "Inflatable Re-entry Vehicle Experiment (IRVE) - 4 Overview," pp. 1–14, 21st AIAA Aerodynamic Decelerator Systems Technology Conference, May 2011, Dublin, Ireland, AIAA 2011-2580.

[7] H. Wright, A. Cutright, J. Corliss, W. Bruce, D. Trombetta, A. R. Mazaheri, M. Coleman, A. Olds, and S. Hancock, "Heart Flight Test Overview," pp. 1–13, 9th International Planetary Probe Workshop, June 2012, Toulouse, France.

[8] K. Barnstorff, "NASA Technology May Help Protect Wildland Firefighters," NASA Langley Research Center online research article, June 16, 2015.

[9] K. Daryabeigi and S. Miller, "Heat Transfer in High Temperature Muiltilayer Insulation," pp. 1–9, 5th European Workshop on Thermal Protection Systems and Hot Structures, May 2006, Noordwijk, Netherlands.

[10] K. Daryabeigi, "Thermal Analysis and Design Optimization of Multilayer Insulation for Reentry Aerodynamic Heating," *Journal of Spacecraft and Rockets*, vol. 39, no. 4, pp. 509–514, Jul. 2002.

[11] K. Daryabeigi, "PhD Thesis: Design of High Temperature Multi-layer Insulation for Reusable Launch Vehicles," University of Virginia, 2000.

[12] R. Savage, W. Love, and F. Bloetscher, "High Temperature Performance of Flexible Thermal Protection Materials," presented at the 19th Thermophysics Conference, Reston, Virgina, 2012, pp. 1–10.

[13] S. J. Hughes, R. A. Dillman, B. R. Starr, R. A. Stephan, M. C. Lindell, C. J. Player, and F. M. Cheatwood, "Inflatable Re-entry Vehicle Experiment (IRVE) Design Overview," pp. 1–14, 18th AIAA Aerodynamic Decelerator Systems Technology Conference and Seminar, July 2005, AIAA 2005-1636.

[14] M. McGuire, J. Arnold, A. Covington, and I. Dupzyk, "Flexible Ablative Thermal Protection Sizing on Inflatable Aerodynamic Decelerator for Human Mars Entry Descent and Landing," presented at the 49th AIAA Aerospace Sciences Meeting including the New Horizons Forum and Aerospace Exposition, Reston, Virginia, 2012, pp. 1–9.

[15] M. McGuire, "Dual Heat Pulse, Dual Layer Thermal Protection System Sizing Analysis and Trade Studies for Human Mars Entry Descent and Landing," presented at the 49th AIAA Aerospace Sciences Meeting including the New Horizons Forum and Aerospace Exposition, Reston, Virginia, 2012, pp. 1–15.

[16] R. A. S. Beck, J. O. Arnold, S. White, W. Fan, M. Stackpoole, P. Agrawal, and S. Coughlin, "Overview of Initial Development of Flexible Ablators for Hypersonic Inflatable Aerodynamic Decelerators," pp. 1–16, 21st AIAA Aerodynamic Decelerator Systems Technology Conference, May 2011, Dublin, Ireland, AIAA 2011-2511.

[17] Sigratherm Online Brochure, "SIGRATHERM® KFA," Accessed Sep. 2014.

[18] Aspen Aerogels Material Safety Datasheet, "Pyrogel 2250 MSDS", Accessed Sep. 2014.

[19] S. A. Tobin and J. A. Dec, "A Probabilistic Sizing Demonstration of a Flexible Thermal Protection System for a Hypersonic Inflatable Aerodynamic Decelerator," presented at the 53rd AIAA Aerospace Sciences Meeting, Reston, Virginia, 2015, pp. 1–13, AIAA 2015-1895.

[20] A. Mazaheri, W. E. Bruce III, N. J. Mesick, and K. Sutton, "Methodology for Flight-Relevant Arc-Jet Testing of Flexible Thermal Protection Systems," *Journal of Spacecraft and Rockets*, vol. 51, no. 3, pp. 789–800, May 2014.

[21] R. M. Sullivan, E. H. Baker, J. Dec, and N. S. Jacobson, "Analysis Methods for Heat Transfer in Flexible Thermal Protection Systems for Hypersonic Inflatable Aerodynamic Decelerators," NASA TM-2014-218311, April 2014.

[22] R. E. Walpole, R. H. Myers, S. L. Myers, and K. Ye, *Probability & Statistics for Engineers and Scientists*, 8th ed. New Jersey: Pearson Prentice Hall, 2007.

[23] D. C. Montgomery and G. C. Runger, *Applied Statistics and Probability for Engineers*, 5th ed. Wiley, 2011.

[24] J. Lachaud, T. E. Magin, I. Cozmuta, and N. N. Mansour, "A Short Review of Ablative-Material Response Models and Simulation Tools", pp. 1–30, 7th Aerothermodynamics Symposium, May 2011, Belgium.

[25] H. Hurwicz, "Aerothermochemistry Studies in Ablation", 5th AGARD Combustion and Propulsion Colloquium, April 1962.

[26] C. J. Katsikas, G. K. Castle, and J. S. Higgins, "Ablation Handbook - Entry Materials Data and Design", presented at the AFML-TR-66-262, 1966.

[27] T. R. Munson and R. J. Spindler, "Transient Thermal Behavior of Decomposing Materials - Part 1 General Theory and Application to Convective Heating", *Armed Services Technical Information Agency AD 256909*, Mar. 1961.

[28] Acurex Corporation Aerotherm Division, "User's Manual, Aerotherm Charring Material Thermal Response and Ablation Program", Nov. 1987.

[29] Y. K. Chen and F. S. Milos, "Ablation and Thermal Response Program for Spacecraft Heatshield Analysis", *Journal of Spacecraft and Rockets*, vol. 36, no. 3, pp. 475–483, May 1999.

[30] F. S. Milos, Y. K. Chen, and T. Squire, "Updated Ablation and Thermal Response Program for Spacecraft Heatshield Analysis", presented at the 17th Thermal and Fluids Analysis Workshop, 2006.

[31] R. M. Amundsen, J. A. Dec, M. C. Lindell, "Thermal Analysis Methods for an Earth Entry Vehicle", pp. 1–18, 11th Thermal and Fluids Analysis Workshop, August 2000, Cleveland, Ohio.

[32] M. J. Wright, C. Y. Tang, K. T. Edquist, B. R. Hollis, P. Krasa, and C. A. Campbell, "A Review of Aerothermal Modeling for Mars Entry Missions", pp. 1–38, 48th AIAA Aerospace Sciences Meeting Including the New Horizons Forum and Aerospace Exposition, January 2010, Orlando, Florida, AIAA 2010-443.

[33] M. J. Wright, D. Bose, and Y. K. Chen, "Probabilistic Modeling of Aerothermal and Thermal Protection Material Response Uncertainties", *AIAA Journal*, vol. 45, no. 2, pp. 399–410, Feb. 2007.

[34] Wright, M. J., "CEV Thermal Protection System (TPS) Margin Management Plan," NASA Ames Research Center, C-TPSA-A-DOC-7005, Rev. v6d1, November, 2006.

[35] S. Hughes, J. Ware, J. Del Corso, and R. Lugo, "Deployable Aeroshell Flexible Thermal Protection System Testing", presented at the 20th AIAA Aerodynamic

Decelerator Systems Technology Conference and Seminar, Reston, Virginia, 2012, pp. 1–21.

[36] W. E. Bruce III, N. J. Mesick, P. G. Ferlemann, P. M. Siemers III, J. A. Del Corso, S. J. Hughes, S. A. Tobin, and M. P. Kardell, "Aerothermal Ground Testing of Flexible Thermal Protection Systems for Hypersonic Inflatable Aerodynamic Decelerators", pp. 1–11, 9th International Planetary Probe Workshop, June 2012, Toulouse, France.

[37] American Standard Test Method International, "Standard Test Method for Thermal Diffusivity by the Flash Method", *ASTM International*, 2013.

[38] "Step Heat Apparatus", TPRL Laboratory Website, Purdue University, January 2012.

[39] K. Daryabeigi, "Heat Transfer in High-Temperature Fibrous Insulation", *Journal of Thermophysics and Heat Transfer*, vol. 17, no. 1, Mar. 2003.

[40] K. Daryabeigi, "Thermal Analysis and Design of Multi-layer Insulation for Re-entry Aerodynamic Heating", 35th AIAA Thermophysics Conference, June 2001, Anaheim, CA, AIAA 2001-2834.

[41] K. Daryabeigi, "Analysis and testing of high temperature fibrous insulation for reusable launch vehicles", presented at the 37th Aerospace Sciences Meeting and Exhibit, Reston, Virginia, 2012.

[42] American Standard Test Method International, "Standard Test Method for Thermal Conductivity of Refractories", *ASTM International*, Jan. 2013.

[43] American Standard Test Method International, "Determining Specific Heat Capacity by Differential Scanning Calorimetry", *ASTM International*, 2011.

[44] ASTM, "Standard Test Method for Decomposition Kinetics by Thermogravimetry Using the Ozawa/Flynn/Wall Method", ASTM International, West Conshohocken, PA, 2013.

[45] M. N. Ozisik and H. R. B. Orlande, *Inverse Heat Transfer*. New York: Taylor & Francis, 2000.

[46] O. M. Alifanov, *Inverse Heat Transfer Problems*. Springer-Verlag, 1994.

[47] H. R. B. Orlande, F. Fudym, D. Maillet, and R. Cotta, *Thermal Measurements and Inverse Techniques*. Florida: CRC Press, 2011.

[48] K. A. Woodbury, *Inverse Engineering Handbook*. CRC Press, 2003.

[49] B. Laub, "High Fidelity Modeling Shortcourse Presentation", pp. 1–23, NASA Ames Research Center, Nov. 2004.

[50] J. Beck and K. Arnold, *Parameter Estimation in Engineering and Science*. New York: Wiley, 1977.

[51] K. Kurpisz and A. J. Nowak, *Inverse Thermal Problems*. Computational Mechanics Publications, 1995.

[52] R. Aster, B. Borchers, and C. Tauber, *Parameter Estimation and Inverse Problems*. Burlington: Elsevier, 2005.

[53] S. Dutta, R. D. Braun, R. P. Russell, S. A. Striepe, and I. G. Clark, "Comparison of Statistical Estimation Techniques for Mars Entry, Descent, and Landing Reconstruction", *Journal of Spacecraft and Rockets*, vol. 50, no. 6, pp. 1207–1221, Nov. 2013.

[54] M. Mahzari, R. D. Braun, T. R. White, and D. Bose, "Inverse Estimation of the Mars Science Laboratory Entry Aeroheating and Heatshield Response", *Journal of Spacecraft and Rockets*, vol. 52, no. 4, pp. 1203–1216, Jul. 2015.

[55] D. A. Spencer, R. C. Blanchard, R. D. Braun, P. H. Kallemeyn, and S. W. Thurman, "Mars Pathfinder Entry, Descent, and Landing Reconstruction", *Journal of Spacecraft and Rockets*, vol. 36, no. 3, pp. 357–366, May 1999.

[56] M. Mahzari, "PhD Thesis: Inverse Estimation Methodology for the Analysis of Aeroheating and Thermal Protection System Data", pp. 1–213, Oct. 2013, Georgia Institute of Technology.

[57] S. Dutta, "PhD Thesis: Statistical Methods for Reconstruction of Entry, Descent, and Landing Performance with Application to Vehicle Design", Georgia Institute of Technology, 2013.

[58] M. Mahzari and R. D. Braun, "Time-Dependent Mars Entry Aeroheating Estimation from Simulated In-Depth Heat Shield Temperature Measurements", *Journal of Thermophysics and Heat Transfer*, vol. 27, no. 3, pp. 435–446, Jul. 2013.

[59] M. Mahzari, T. R. White, R. Braun, and D. Bose, "Inverse Estimation of the Mars Science Laboratory Entry Aerothermal Environment and Thermal Protection System Response", presented at the 44th AIAA Thermophysics Conference, Reston, Virginia, 2013, pp. 1–19.

[60] J. M. DiNonno, F. M. Cheatwood, S. J. Hughes, M. M. Ragab, R. A. Dillman, R. J. Bodkin, C. H. Zumwalt, and R. K. Johnson, "HIAD on ULA (HULA) Orbital Reentry Flight Experiment Concept", 13th International Planetary Probe Workshop, June 2016, Laurel, MD.

[61] D. M. Bose, R. Winski, J. Shidner, C. Zumwalt, C. O. Johnston, D. R. Komar, F. M. Cheatwood, and S. J. Hughes, "The Hypersonic Inflatable Aerodynamic Decelerator

(HIAD) Mission Applications Study", 22nd Aerodynamic Decelerator Systems Technology Conference, March 2013, Daytona Beach, FL.

[62] J. G. Reed, M. M. Ragab, F. M. Cheatwood, S. J. Hughes, J. DiNonno, R. Bodkin, A. Lowry, G. T. Brierly, and J. W. Kelly, "Performance Efficient Launch Vehicle Recovery and Reuse", AIAA SPACE 2016, September 2016, Long Beach, CA.

[63] D.-C. A. M, J. L. Davis, W. C. Engelund, D. R. Komar, E. M. Queen, J. A. Samareh, D. W. Way, T. A. Zang, J. G. Murch, S. A. Krizan, A. D. Olds, R. W. Powell, J. D. Shidner, D. J. Kinney, M. K. McGuire, J. O. Arnold, M. A. Covington, R. R. Sostaric, C. H. Zumwalt, and E. G. Llama, "Entry, Descent and Landing Systems Analysis Study: Phase 2 Report on Exploration Feed-Forward Systems", NASA, TM-217055, Feb. 2011.

[64] A. Mazaheri, "High-Energy Atmospheric Reentry Test Aerothermodynamic Analysis", *AIAA Journal of Spacecraft and Rockets*, vol. 50, no. 2, Mar. 2013.

[65] C. Davies, "Planetary Mission Entry Vehicles", Quick Reference Guide Handbook, NASA Technical Report SP-2006-3401, January 2006, Moffett Field, CA.

[66] R. D. Braun and R. M. Manning, "Mars Exploration Entry, Descent, and Landing Challlenges", *Journal of Spacecraft and Rockets*, vol. 44, no. 2, pp. 310–323, Mar. 2007.

[67] H. K. Tran, C. E. Johnson, D. J. Rasky, F. C. L. Hui, M.-T. Hsu, T. Chen, Y. K. Chen, D. Paragas, and L. Kobayashi, "Phenolic Impregnated Carbon Ablators (PICA) as Thermal Protection Systems for Discovery Missions", NASA Ames Research Center, April 1997, Moffett Field, CA, NASA-TM-110440.

[68] E. L. Strauss, "Superlight Ablative Systems for Mars Lander Thermal Protection" *AIAA Journal of Spacecraft and Rockets*, vol. 4, no. 10, 1967, pp. 1304-1309.

[69] L. T. Chauvin, R. B. Erb, D. H. Greenshields, J. E. Pavlosky, and C. L. Statham, "Apollo thermal-protection system development", *Journal of Spacecraft and Rockets*, vol. 7, no. 6, pp. 727–734, Jun. 1970.

[70] W. H. Willcockson, "Mars Pathfinder Heatshield Design and Flight Experience", *Journal of Spacecraft and Rockets*, vol. 36, no. 3, pp. 374–379, May 1999.

[71] W. H. Willcockson, "Stardust Sample Return Capsule Design Experience", *Journal of Spacecraft and Rockets*, vol. 36, no. 3, pp. 470–474, May 1999.

[72] R. A. Mitcheltree, S. Kellas, J. T. Dorsey, P. N. Desai, and C. J. Martin, "A Passive Earth-Entry Capsule for Mars Sample Return", 7th AIAA/ASME Joint Thermophysics and Heat Transfer Conference, June 1998, Albuquerque, NM.

[73] M. Wright, I. Cozmuta, B. Laub, Y.-K. Chen, and W. H. Wilcoxson, "Defining Ablative Thermal Protection System Margins for Planetary Entry Vehicles", presented at the 42nd AIAA Thermophysics Conference, Reston, Virginia, 2012, pp. 1–27.

[74] J. A. Dec, "PhD Thesis: Three Dimensional Finite Element Ablative Thermal Response Analysis Applied to Heatshield Penetration Design", Georgia Institute of Technology, Apr. 2011.

[75] M. J. Wright, R. A. S. Beck, K. T. Edquist, D. Driver, S. A. Sepka, E. M. Slimko, and W. H. Willcockson, "Sizing and Margins Assessment of Mars Science Laboratory Aeroshell Thermal Protection System", *Journal of Spacecraft and Rockets*, vol. 51, no. 4, pp. 1125–1138, Jul. 2014.

[76] J. Dec and R. Mitcheltree, "Probabilistic design of a Mars Sample Return Earth Entry Vehicle Thermal Protection System", 40th AIAA Aerospace Sciences Meeting & Exhibit, Reston, Virginia, 2012.

[77] Y.-K. Chen, T. Squire, B. Laub, and M. Wright, "Monte Carlo Analysis for Spacecraft Thermal Protection System Design", presented at the 9th AIAA/ASME Joint Thermophysics and Heat Transfer Conference, Reston, Virginia, 2012.

[78] M. J. Wright, J. H. Grinstead, and D. Bose, "A Risk-Based Approach for Aerothermal/ TPS Analysis and Testing", pp. 1–25, NASA Ames Research Center, July 2007, Moffett Field, CA.

[79] M. Wright, I. Cozmuta, B. Laub, Y.-K. Chen, and W. H. Wilcoxson, "Defining Ablative Thermal Protection System Margins for Planetary Entry Vehicles", 42nd AIAA Thermophysics Conference, Reston, Virginia, 2012, pp. 1–27.

[80] A. J. Brune, S. Hosder, K. T. Edquist, and S. A. Tobin, "Thermal Protection System Response Uncertainty of a Hypersonic Inflatable Aerodynamic Decelerator", *AIAA Journal of Spacecraft and Rockets*, vol. 54, no. 1, Jan. 2017.

[81] A. J. Brune, S. Hosder, K. T. Edquist, and S. A. Tobin, "Uncertainty Analysis of Thermal Protection System Response of a Hypersonic Inflatable Aerodynamic Decelerator", presented at the 46th AIAA Thermophysics Conference, 2016.

[82] M. Mahzari, I. Cozmuta, I. Clark, and R. Braun, "An Inverse Parameter Estimation Methodology for the Analysis of Aeroheating and Thermal Protection System Experimental Data", presented at the 42nd AIAA Thermophysics Conference, Reston, Virginia, 2012, pp. 1–25.

[83] G. Vanderplaats, *Multidiscipline Design Optimization*. Colorado Springs, CO: Vanderplaats Research & Development, Inc., 2007.

[84] J. H. Flynn and L. A. Wall, "A Quick, Direct Method for the Determination of Activation Energy from Thermogravimetric Data", pp. 1–6, Dec. 2002.

[85] M. E. Brown, *Handbook of Thermal Analysis and Calorimetry*, vol. 1. Amsterdam, Netherlands: Elsevier, 1998.

[86] P. Gabbott, *Principles and Applications of Thermal Analysis*. Oxford, UK: Blackwell Publishing, 2008.

[87] J. P. Schaffer, A. Saxena, S. D. Antolovich, T. H. Sanders Jr, and S. B. Warner, *The Science and Design of Engineering Materials*, 2nd ed. McGraw-Hill, 1999.

[88] R. Blaine, "A Faster Approach to Obtaining Kinetic Parameters", pp. 1–3, Feb. 1998.

[89] R. L. Blaine and B. K. Hahn, "Obtaining Kinetic Parameters by Modulated Thermogravimetry", pp. 1–10, Jun. 1999.

[90] ASTM, "Standard Test Methods for Kinetic Parameters by Factor Jump/Modulated Thermogravimetry", ASTM International, West Conshohocken, PA.

[91] TA Instruments, "TA Instruments Q5000 IR Brochure", pp. 1–19, Accessed Jan. 2011.

[92] J. Cai, W. Wu, R. Liu, and G. W. Huber, "A Distributed Activation Energy Model for the Pyrolysis of Lignocellulosic Biomass", *Green Chemistry*, vol. 15, no. 5, p. 1331, 2013.

[93] J. Cai, W. Wu, and R. Liu, "An overview of distributed activation energy model and its application in the pyrolysis of lignocellulosic biomass", *Renewable and Sustainable Energy Reviews*, vol. 36, pp. 236–246, Aug. 2014.

[94] J. Cai and R. Liu, "New distributed activation energy model: Numerical solution and application to pyrolysis kinetics of some samples of biomass", *Bioresource Technology*, vol. 99, no. 8, pp. 2795–2799, May 2008.

[95] S. J. Hughes, F. M. Cheatwood, A. M. Calomino, and H. S. Wright, "Hypersonic Inflatable Aerodynamic Decelerator (HIAD) Technology Development Overview", 22nd AIAA Aerodynamic Decelerator Systems Technology Conference, March 2013, Daytona Beach, Florida.

[96] J. M. DiNonno, F. M. Cheatwood, S. J. Hughes, R. A. Dillman, R. J. Bodkin, C. H. Zumwalt, and R. K. Johnson, "HIAD on ULA (HULA) Orbital Reentry Flight Experiment Concept - Presentation", presented at the 13th International Planetary Probe Workshop, Laurel, Maryland, 2016.

[97] H. S. Wright and F. M. Cheatwood, "High Energy Atmospheric Reentry Test (HEART) Overview of Proposed Flight Test - Presentation", presented at the 9th International Planetary Probe Workshop, Toulouse, France, 2012.

[98] R. A. Lugo, J. D. Shidner, R. W. Powell, S. M. Marsh, J. A. Hoffman, D. K. Litton, and T. L. Schmitt, "Launch Vehicle Ascent Trajectory Simulation Using the Program to Optimize SImulated Trajectories II (POST2)", NASA Technical Report Server, 2017.

[99] C. Zumwalt, "HIAD Secondary Payload on Centaur - Presentation", internal work accessed August, 2017.

[100] J. A. Dec, "HIAD Flexible Thermal Protection System (FTPS) Margin Management Policy", Hampton, VA, NASA internal work in the form of a Technical Memorandum (TM), November 2013.